Insights into biopharmaceutical freezing processes
- Characterization and impact of freeze concentration

zur Erlangung des akademischen Grades eines

DOKTORS DER INGENIEURWISSENSCHAFTEN (DR.-ING.)

von der KIT-Fakultät für Chemieingenieurwesen und Verfahrenstechnik des

Karlsruher Instituts für Technologie (KIT)

genehmigte

DISSERTATION

von

Dennis Weber, M. Sc.

geboren in Malsch, Kreis Karlsruhe

Danksagung

Nur durch die Unterstützung zahlreicher Mitmenschen ist die nachfolgende Arbeit zu dem geworden, was sie ist.

Zunächst möchte ich mich bei Herrn Prof. Hubbuch bedanken, für die Betreuung meiner Arbeit, die Inspiration zu neuen Ansätzen und die Freiheit meine wissenschaftlichen Interessen zu verfolgen, wann immer möglich.

Herrn Prof. Eppink möchte ich für sein fachliches Interesse, das daraus resultierende Feedback und die Übernahme des Zweitgutachtens danken.

Die Arbeit wurde in Teilen von Bilfinger Industrietechnik Salzburg GmbH, Schwetzingen finanziert. Diese Projektarbeit hat mich vor allem zu Beginn in zielführende Bahnen geleitet.

Dem Institut MAB gilt mein besonderer Dank. Die positive und produktive Arbeitsatmosphäre motivierte mich in Hochphasen und fing mich auf, wenn es mal nicht so gut lief. Zahlreiche Abende, Kaffeepausen und Kuchen versüßten mir den Alltag.
Meine Bürokollegen Anna Westkamp, Marieke Klijn und Nils Hillebrandt hatten von Beginn an ein offenes Ohr für meine Ideen. Annabelle Dietrich, Jan Weggen und Robin Schiemer gaben mir gegen Ende zahlreiches Feedback und ermöglichten mir eine neue Sicht auf meine Erkenntnisse. Susanna Suhm und Nicola Böhner danke ich für ihre ansteckende positive Einstellung, die sie beide am gesamten Institut verbreiteten. Meinen Studenten Christian Sittig, Enja Schwarz, Jan Kehrbaum, Konstantin Petry, Monika Desombre und Thomas Fuchs verdanke ich nicht nur ihre wissenschaftlichen Beiträge, sondern auch viel Spaß während Pausen und Partys.

Angela Valentic möchte ich danken für ihren Enthusiasmus, ihre Feierlaune und dafür, alle meine wissenschaftlichen Probleme über sich ergehen zu lassen.

Meiner Familie Erika Weber, Frank Glaser und Jennifer Weber möchte ich für das Vertrauen und die Unterstützung während meiner gesamten Zeit am KIT danken. Ihr habt mich ermutigt und mir den Rücken freigehalten.

Karo, dir gilt ein ganz besonderer Dank. Für alles.

Abstract

The continuously expanding biopharmaceutical product pipeline ranges from monoclonal antibodies (mAb) to insulin and messenger ribonucleic acid (mRNA). Over the last decade, the pressure on rapid process development has been intensified and peaked during the outbreak of the COVID-19 pandemic due to the urgent need for novel therapeutics and vaccines. Especially the optimization of storage conditions and temperatures was relevant for novel vaccines. While storage of liquid formulations in a frozen state at -80 °C is considered a safe option with regards to integrity of the active pharmaceutical ingredient (API), the need for cryo-technology restricts the handleability and availability of the drug. At elevated freezing temperatures, however, freezing-induced stresses such as freeze concentration are more pronounced. The necessary optimization of storage temperatures and freezing processes poses a challenge, leading to a potential overestimation of the required storage temperature during rapid process development. Conducted formulation studies to investigate the stability of biopharmaceuticals are time and material consuming with durations of up to 24 months and freezing volumes of up to hundred liters during transportation. High-throughput screenings of formulations at microliter-scale are used to study protein stability and freeze-thaw behavior, for example cold denaturation of proteins. However, mass transport phenomena due to freeze concentration are neglected, which are more pronounced at larger scales. Milliliter-scale models are therefore proposed to study freeze concentration behavior, bridging the gap between high-throughput screening and production scale.

For comparison and validation of differently scaled models, process analytical technology (PAT) is essential. Monitoring quality attributes and process parameters such as temperature can improve process understanding as requested by regulatory authorities for process approval. PAT may generate experimental data on transient phenomena and enable process control, for example by determination of the freezing endpoint. Furthermore, the real-time data may be used to validate models, such as in-silico simulations, which are becoming a valuable tool for process prediction and optimization in the biopharmaceutical industry.

To facilitate freezing process design and optimization, it is the aim of this thesis to improve process understanding of biopharmaceutical freezing processes. Therefore, a scale-down model was designed and characterized by two novel PAT approaches. Process parameters affecting the freeze concentration were identified and monitored. The generated transient data on the freezing process were used to investigate the applicability of existing computational fluid dynamic (CFD) models to describe and predict freezing processes by an in-silico model. Lastly, a case study with a monoclonal

antibody (mAb) process intermediate was conducted to evaluate the impact of freeze concentration on mAb process development and manufacturing.

In the first study[1] (Chapter 3), the novel freeze-thaw device was described and characterized by an improved temperature setup. The small-scale freeze-thaw device was designed as a slice from a larger hollow cylinder, which is actively cooled from the in- and outside. To minimize freezing at the bottom of the container, an insulating layer as well as an additional counteracting cooling loop at the container bottom were installed. Furthermore, the insulating layer divided the container into six individual chambers with working volume of up to 100 mL.

Biopharmaceutical freezing processes are usually monitored by a small number or even a single temperature probe. Heat conduction, convection, and freezing point depression with ongoing freeze concentration pose measurement challenges, which are difficult to overcome by temperature probes at low spatial resolution. In this study, the spatial resolution was improved by a temperature probe array using Fiber-Bragg-Grating sensors. Monitoring of the freeze front progression was further improved by evaluation of the second time derivative of temperature to overcome the influence of freeze point depression on the detection of freezing. For freezing of concentrated buffer solutions, elevated freezing temperatures above -30 °C led to a settlement of the last point to freeze (LPTF) in the container from top to bottom. Furthermore, a longer freezing time increased the degree of freeze concentration measured in the frozen bulk. As a result, the freezing time was identified as a critical process parameter (CPP). Using purified water as a cheap and widely available model liquid, a correlation between freezing time and freezing temperature was put into theoretical context with the Plank equation, which is commonly applied in the food industry. Furthermore, the freezing time was not only dependent on the set freezing temperature but also on the heat dissipation capacity of the attached refrigeration unit. Therefore, in rapid freezing processes, such as those found in common freezing bags, reducing the set freezing temperature may not improve the homogeneity of the freeze concentration.

While the temperature in biopharmaceutical freezing processes is often monitored continuously, it does not directly reflect a quality attribute of the drug. The protein and additive concentrations, however, have been classified as critical quality attributes (CQA). Until now, they have only been measured by sampling from the frozen bulk after completion of the freezing process. A non-destructive analytical method to monitor freeze concentration is missing yet, leading to a knowledge gap in

---

[1] *Weber et al. (2021), Frontiers in Bioengineering and Biotechnology, 9, 617770*

Abstract

the origin of freeze concentration and mass transport phenomena. Without this process understanding, predicting freeze concentration after changes in formulation or freezing temperature remains challenging. Therefore, the process characterization was advanced by the application of Raman spectroscopy as a novel PAT for real-time monitoring of freeze concentration in a second study[2] (Chapter 4). The concentrations of each solute in multi-component model formulations were monitored simultaneously using partial least squares (PLS) regression modelling. The concentrations predicted simultaneously for each component were validated by samples taken close to the Raman probe.

Overall, the freezing time had the largest impact on the freeze concentration, with increasing freezing time leading to increased freeze concentration. This confirms the findings of the first study (Chapter 3). An increase in initial sucrose concentration led to increased freeze concentration, which is important to consider during formulation development. In addition, convection currents as small as 1 mm were detected at the bottom of the vessel, highlighting the need for high-resolution PAT. Furthermore, the separation of solutes during freezing was shown, indicating potential destabilization of the API. The presented approach provides a robust, non-destructive PAT that can be applied at various scales in both industry and academia.

Concluding Chapter 3 and 4, freezing time and freeze concentration were identified as CPP and CQA, respectively. As mentioned earlier, intensification of process development is of great importance and can be accelerated by in-silico models. Using the data on the freezing process, the applicability of an existing CFD model to describe and predict freezing processes was investigated (Chapter 5). Freezing times were simulated using water as a single component solidification system. The solution was evaluated by a mesh and time step size study with converging results indicating simulation reliability. The predicted freezing times at freezing temperatures between -60 and -20 °C agreed with experimental results with minor deviations, that were attributed to cooldown of system components such as the steel housing. To simulate freeze concentration, the simulation was extended by a species model. Sucrose was selected as a model component and its temperature- and concentration-dependent physical properties were implemented in the model. Initial results were able to provide qualitative insights into the freezing process and mass transport phenomena present, which substantiated the discussion in the other studies. However, mass imbalances due to discretization inaccuracies were found, making quantitative comparisons challenging. The predicted concentrations were dependent

---

[2] *Weber et al., accepted (31.08.2021) by Biotechnology and Bioengineering*

on discretization parameters whereby large time steps and small viscosities led to increasing mass imbalances. Increasing the time and mesh resolution was not feasible due to hardware restrictions. In the future, alternatives to the enthalpy-porosity method used to describe solidification, or improvement in the discretization methods, should be evaluated for quantitative prediction of freeze concentration.

At last, the relevance of freeze concentration for the biopharmaceutical industry was investigated in a case study using an industrial process intermediate from a mAb platform process[3] (Chapter 6). In between the typical production stages (Upstream, Downstream and Formulation), the process intermediates are handed over from one department to another. In contrast to the manufacturing process, where process intermediates are processed directly, the intermediates are often frozen during process development due to time and project limitations. To answer the question of comparability, the case study investigated the impact of freezing on the CQAs of a mAb purification process. Therefore, cell culture supernatant (CCS) was subjected to an additional freeze-thaw cycle at temperatures from -60 to -20 °C, subsequently filtered and captured by a protein A chromatography. After the capture step, the CQAs showed a significant decrease in the remaining host cell proteins (HCP) and mAb aggregates after slow freezing processes in comparison to a reference sample. This was attributed to aggregation of mAb and specific HCPs. These aggregates formed particles larger than 0.2 µm, that were removed by a common filtration step and thus lead to an overestimated quality of the protein A eluate. Furthermore, smaller HCPs in the CCS were freeze concentrated to a higher degree. As a result, the study revealed the dependency of freeze concentration on the diffusion coefficient.

In summary, the thesis improves the overall process understanding of biopharmaceutical freezing processes by highlighting the contribution of mass transport phenomena to freeze concentration during the freezing process. Two novel tools to validate the scalability of freezing processes and potential in-silico models are presented. While currently existing CFD models were found to sufficiently estimate the freezing time of a container, the simulation of freeze concentration has to be carefully evaluated with regards to discretization and solution independency from physical properties. Overall, the thesis facilitates the development and optimization of novel freezing containers, formulations and freezing processes with regards to freeze concentration and required freezing temperature.

---

[3] *Weber et al. (2021), Biotechnology and Bioengineering, 118, 3914– 3925*

Zusammenfassung

Die ständig wachsende biopharmazeutische Produktpipeline reicht von monoklonalen Antikörpern (mAb) bis hin zu Insulin und Boten-Ribonukleinsäure (mRNA). Im letzten Jahrzehnt hat sich der Druck auf eine schnelle Prozessentwicklung erhöht und erreichte während des Ausbruchs der COVID-19-Pandemie aufgrund des dringenden Bedarfs an neuartigen Therapeutika und Impfstoffen seinen Höhepunkt. Insbesondere die Optimierung der Lagerungsbedingungen und -temperaturen war dabei für neuartige Impfstoffe von Bedeutung. Während die Lagerung von Flüssigformulierungen in gefrorenem Zustand bei 80 °C als sichere Option im Hinblick auf die Unversehrtheit des pharmazeutischen Wirkstoffs (API) gilt, schränkt die Notwendigkeit von Kryotechnik die Handhabbarkeit und Verfügbarkeit des Arzneimittels ein. Bei höheren Gefriertemperaturen sind jedoch die gefrierbedingten Belastungen wie die Gefrierkonzentration stärker ausgeprägt. Die notwendige Optimierung von Lagertemperaturen und Gefrierprozessen stellt eine Herausforderung dar, die dazu führt, dass die erforderliche Lagertemperatur bei der schnellen Prozessentwicklung möglicherweise überschätzt wird. Durchgeführte Formulierungsstudien zur Untersuchung der Stabilität von Biopharmazeutika sind zeit- und materialaufwändig mit Laufzeiten von bis zu 24 Monaten und Gefriervolumina von bis zu hundert Litern während des Transports. Hochdurchsatz-Screenings von Formulierungen im Mikrolitermaßstab werden zur Untersuchung der Proteininstabilität und des Gefrier-Auftau-Verhaltens eingesetzt, z. B. zur Kältedenaturierung von Proteinen. Dabei werden jedoch Massentransportphänomene aufgrund der Gefrierkonzentration vernachlässigt, die in größeren Maßstäben stärker ausgeprägt sind. Daher werden Modelle im Milliliter-Maßstab vorgeschlagen, um das Gefrierkonzentrationsverhalten zu untersuchen und die Lücke zwischen Hochdurchsatz-Screening und Produktionsmaßstab zu schließen.

Für den Vergleich und die Validierung unterschiedlich skalierter Modelle ist die prozessanalytische Technologie (PAT) unerlässlich. Die Überwachung von Qualitätsmerkmalen und Prozessparametern wie der Temperatur kann das Prozessverständnis verbessern, wie es von den Regulierungsbehörden für die Prozessgenehmigung gefordert wird. PAT kann experimentelle Daten über instationäre Phänomene generieren und die Prozesssteuerung ermöglichen, beispielsweise durch die Bestimmung des Gefrierendpunkts. Darüber hinaus können die Echtzeitdaten zur Validierung von Modellen verwendet werden, wie beispielsweise in-silico Modelle, die zu einem wertvollen Instrument für die Prozessvorhersage und -optimierung in der biopharmazeutischen Industrie werden.

Um die Gestaltung und Optimierung von Gefrierprozessen zu erleichtern, ist es das Ziel dieser Arbeit, das Prozessverständnis biopharmazeutischer Gefrierprozesse zu verbessern. Daher wurde ein kleinskaliges Einfrier-Auftau-Modell entworfen und durch zwei neue PAT-Ansätze charakterisiert. Prozessparameter, die die Gefrierkonzentration beeinflussen, wurden identifiziert und überwacht. Die erzeugten instationären Daten über den Einfriervorgang wurden verwendet, um die Anwendbarkeit bestehender CFD-Modelle (engl. Computational Fluid Dynamics) zur Beschreibung und Vorhersage von Gefrierprozessen durch ein In-silico-Modell zu untersuchen. Schließlich wurde eine Fallstudie mit einem Zwischenprodukt eines mAb-Produktionsprozesses durchgeführt, um die Auswirkungen der Gefrierkonzentration auf die Entwicklung und Herstellung von mAb-Prozessen zu bewerten.

In der ersten Studie[4] (Kapitel 3) wurde das neuartige Einfrier-Auftau-Modell beschrieben und durch verbesserte Temperaturmessungen charakterisiert. Das Model im kleinen Maßstab wurde als Scheibe eines größeren Hohlzylinders konzipiert, der von innen und außen aktiv gekühlt wird. Um das Einfrieren am Boden des Behälters zu minimieren, wurden eine Isolierschicht sowie eine zusätzliche entgegenwirkende Kühlschleife am Behälterboden installiert. Außerdem unterteilte die Isolierschicht den Behälter in sechs einzelne Kammern mit 100 mL Arbeitsvolumen.

Biopharmazeutische Gefrierprozesse werden in der Regel mit einer geringen Anzahl oder sogar nur einem einzigen Temperaturfühler überwacht. Wärmeleitung, Konvektion und Gefrierpunktserniedrigung mit fortschreitender Gefrierkonzentration stellen eine Herausforderung für die Messung dar, die mit Temperaturfühlern mit geringer räumlicher Auflösung nur schwer zu bewältigen ist. In dieser Studie wurde die räumliche Auflösung durch ein Temperatursonden-Array mit Fiber-Bragg-Grating-Sensoren erhöht. Der Verlauf der Gefrierfront in biopharmazeutischen Gefrierprozessen wurde durch Auswertung der zweiten zeitlichen Ableitung der Temperatur überwacht, um den Einfluss der Gefrierpunktsdepression auf die Detektion des Gefrierenprozesses zu überwinden. Beim Einfrieren von konzentrierten Pufferlösungen führten erhöhte Gefriertemperaturen über -30 °C zu einer Verlagerung der Position letzten Gefrierpunkts (LPTF) zum Behälterboden. Außerdem erhöhte eine längere Gefrierzeit den Grad der Gefrierkonzentration, die im gefrorenen Container gemessen wurde. Infolgedessen wurde die Gefrierzeit als kritischer Prozessparameter (CPP) identifiziert. Unter Verwendung von Wasser als günstige und verfügbare

[4] *Weber et al. (2021), Frontiers in Bioengineering and Biotechnology, 9, 617770*

Zusammenfassung

Modellflüssigkeit wurde eine Korrelation zwischen Gefrierzeit und Gefriertemperatur mittels der Plank-Gleichung in einen theoretischen Zusammenhang gebracht. Darüber hinaus war die Gefrierzeit nicht nur von der eingestellten Gefriertemperatur, sondern auch von der Wärmeleistung des angeschlossenen Kühlaggregats abhängig. Bei schnellen Gefrierprozessen, wie sie in gängigen Gefrierbeuteln vorkommen, führt eine Verringerung der eingestellten Gefriertemperatur daher möglicherweise nicht zu einer Verbesserung der Homogenität der Gefrierkonzentration.

Während die Temperatur in biopharmazeutischen Gefrierprozessen häufig kontinuierlich überwacht wird, spiegelt sie kein direktes Qualitätsmerkmal des Arzneimittels wider. Die Konzentrationen von Proteinen und Zusatzstoffen sind hingegen als kritische Qualitätsmerkmale (CQA) eingestuft worden. Bisher wurden sie nur durch die Entnahme von Proben aus der gefrorenen Masse nach Abschluss des Gefrierprozesses gemessen. Eine zerstörungsfreie Analysemethode zur Überwachung der Gefrierkonzentration fehlt bisher, was zu einer Wissenslücke hinsichtlich der Entstehung der Gefrierkonzentration und der Massentransportphänomene führt. Ohne dieses Prozessverständnis bleibt die Vorhersage der Gefrierkonzentration nach Änderungen der Formulierung oder der Gefriertemperatur schwierig. Daher wurde die Prozesscharakterisierung Raman-Spektroskopie als neuartige PAT für die Echtzeitüberwachung der Gefrierkonzentration vorangetrieben, wie in einer zweiten Studie vorgestellt[5] (Kapitel 4). Die Konzentrationen mehrerer gelöster Stoffe wurden gleichzeitig mit Hilfe von PLS-Regressionsmodellen (Partial Least Squares) in Modellformulierungen überwacht. Die für jede Komponente vorhergesagten Konzentrationen wurden anhand von Proben validiert, die in der Nähe der Ramansonde entnommen wurden.

Insgesamt hatte die Gefrierzeit den größten Einfluss auf die Gefrierkonzentration, wobei eine zunehmende Gefrierzeit zu einer erhöhten Gefrierkonzentration führte. Dies bestätigt die Ergebnisse der ersten Studie (Kapitel 3). Eine Erhöhung der anfänglichen Saccharosekonzentration führte ebenfalls zu einer erhöhten Gefrierkonzentration, was bei der Formulierungsentwicklung zu berücksichtigen ist. Darüber hinaus wurden am Boden des Gefäßes Konvektionsströme mit einer Höhe von nur 1 mm festgestellt, was die Notwendigkeit von hochauflösenden PAT zeigt. Darüber hinaus wurde die Trennung von gelösten Stoffen während des Einfrierens nachgewiesen, was auf eine mögliche Destabilisierung des Wirkstoffs hinweist. Der vorgestellte Ansatz bietet eine robuste, zerstörungsfreie PAT, die in verschiedenen

---

[5] *Weber et al., accepted (31.08.2021) by Biotechnology and Bioengineering*

Maßstäben sowohl in der Industrie als auch im akademischen Bereich eingesetzt werden kann.

In Kapitel 3 und 4 wurden Gefrierzeit und Gefrierkonzentration als CPP bzw. CQA identifiziert. Wie bereits erwähnt, ist die Intensivierung der Prozessentwicklung von großer Bedeutung und kann durch In-silico-Modelle beschleunigt werden. Anhand der Daten über den Gefrierprozess wurde die Anwendbarkeit eines bestehenden CFD-Modells zur Beschreibung und Vorhersage von Gefrierprozessen untersucht (Kapitel 5). Die Gefrierzeiten wurden mit Wasser als Modellflüssigkeit simuliert. Konvergierenden Ergebnisse in Gitterstudien wiesen auf die Zuverlässigkeit der Simulation hin. Die vorhergesagten Gefrierzeiten bei Temperaturen zwischen -60 und -20 °C stimmten mit den experimentellen Ergebnissen bis auf geringe Abweichungen überein, welche auf die Abkühlung von Systemkomponenten wie dem Stahlgehäuse zurückgeführt wurden. Um die Gefrierkonzentration zu simulieren, wurde die Simulation um ein Mehrkomponentenmodell erweitert. Als Modellkomponente wurde Saccharose gewählt, deren temperatur- und konzentrationsabhängige physikalische Eigenschaften in das Modell implementiert wurden. Erste Ergebnisse konnten qualitative Einblicke in den Einfrierprozess und vorhandene Massentransportphänomene geben, die die Diskussion in den anderen Studien untermauerte. Jedoch wurden Massenungleichgewichte infolge von Diskretisierungsungenauigkeiten festgestellt, was quantitative Vergleiche erschwerte. Die vorhergesagten Konzentrationen waren von den Diskretisierungsparametern abhängig, wobei große Zeitschritte und geringe Viskositäten zu zunehmenden Massenungleichgewichten führten. Eine Erhöhung der Zeit- und Gitterauflösung war aufgrund von Hardwarebeschränkungen nicht möglich. Zukünftig sollten Alternativen zur Enthalpie-Porositäts-Methode, die zur Beschreibung der Erstarrung verwendet wurde, oder Verbesserung der Diskretisierung für die quantitative Vorhersage der Gefrierkonzentration evaluiert werden.

Abschließend wurde die Bedeutung der Gefrierkonzentration für die biopharmazeutische Industrie in einer Fallstudie anhand eines industriellen Prozesszwischenprodukts aus einem mAb-Plattformprozess untersucht[6] (Kapitel 6). Zwischen den typischen Produktionsstufen (Upstream, Downstream und Formulierung) werden die Prozesszwischenprodukte von einer Abteilung zur anderen weitergereicht. Im Gegensatz zum Herstellungsprozess, bei dem die Prozesszwischenprodukte direkt verarbeitet werden, werden die Zwischenprodukte

---

[6] *Weber et al. (2021), Biotechnology and Bioengineering, 118, 3914– 3925*

Zusammenfassung

während der Prozessentwicklung aus Zeit- und Projektgründen oft eingefroren. Um die Frage der Vergleichbarkeit zu beantworten, untersuchte die Fallstudie die Auswirkungen des Einfrierens auf die CQAs eines mAb-Reinigungsprozesses. Dazu wurde der Zellkulturüberstand (CCS) einem zusätzlichen Gefrier-Auftau-Zyklus bei Temperaturen von -60 bis -20 °C unterzogen, anschließend filtriert und durch eine Protein-A-Chromatographie aufgereinigt. Nach dem Abtrennungsschritt zeigte ein Vergleich der CQAs mit einer Referenzprobe eine signifikante Abnahme der verbleibenden Wirtszellproteine (HCP) und mAb-Aggregate nach langsamen Gefrierprozessen. Dies wurde auf die Aggregation von mAb und spezifischen HCPs zurückgeführt. Diese Aggregate bildeten Partikel mit einer Größe von mehr als 0,2 µm, die in einen Filtrationsschritt entfernt wurden und somit zu einer überschätzten Qualität des Protein-A-Eluats führten. Außerdem wurden kleinere HCPs im CCS in höherem Maße eingefroren. Es wurde eine Abhängigkeit der Gefrierkonzentration vom Diffusionskoeffizienten gefolgert.

Zusammenfassend lässt sich sagen, dass die Arbeit das Prozessverständnis für biopharmazeutische Gefrierprozesse verbessert, indem sie den Beitrag von Massentransportphänomenen zur Gefrierkonzentration während des Gefrierprozesses hervorhebt. Es wurden zwei neue Methoden zur Validierung der Skalierbarkeit und potenzieller In-silico-Modelle von Gefrierprozessen vorgestellt. Während die derzeit kommerziell verfügbaren CFD-Modelle die Gefrierzeit eines Behälters ausreichend abschätzen können, sollte die Vorhersage der Gefrierkonzentration im Hinblick auf die Diskretisierung und die Unabhängigkeit der Lösung von physikalischen Eigenschaften kritisch betrachtet werden. Insgesamt trägt die Arbeit zur Entwicklung und Optimierung von neuartigen Gefrierbehältern, Rezepturen und Gefrierprozessen im Hinblick auf die Gefrierkonzentration und die erforderliche Gefriertemperatur bei.

Contents

1 Introduction

For centuries, freezing has been an essential measure in food preservation to reduce microbial degradation and thus increase the shelf life of perishable goods. Ice deposits in cellars or refrigeration boxes were used for preservation until William Cullen introduced the fundamental concept of fluid evaporation used in modern refrigeration [1]. In recent days, cooling and freezing are essential processes engineered specifically for areas such as the food, the biotechnological and other industries. In the biopharmaceutical manufacturing, susceptible therapeutic proteins are produced, mostly derived from microorganisms. In comparison to chemically synthesized small molecule drugs, such as acetylsalicylic acid or steroids, biopharmaceutics are highly structured with protein sizes ranging from 1000 Da to viruses of a 100 nm diameter. With increasing complexity, biopharmaceutics are prone to chemical and physical degradation and thus need careful evaluation of storage conditions. Common biopharmaceutical products include blood clotting factors, hormones and monoclonal antibodies (mAbs), which dominated the biopharmaceutical market in 2018 and before [2]. In 2020, vaccines containing messenger ribonucleic acid (mRNA) have become a well-known example, which were developed and approved by fast track approval process to tackle the COVID-19 pandemic [3].

Among other things, intense precaution measures to assure drug safety lead to comparably high values of biopharmaceutical drugs with newly approved products priced at up to 2.5 million USD per treatment [4]. To maintain the value and maintain drug safety, product degradation during hold times has to be minimized from manufacturing to transportation, storage and patient administration [5]. Thus, biopharmaceutics are often stabilized in a freeze-dried formulation or frozen and stored at low temperatures [6]. The storage conditions are optimized for each drug during formulation development. For liquid formulation, the storage temperature of different mAb containing drugs varies from -80 °C to 2-8 °C [7]. As another example,

the initial storage conditions of three proposed mRNA vaccines varied in between -20 °C and -60 °C for periods exceeding seven days [8]. The previously mentioned fast track approval and short development times led to uncertainties in the storage conditions and thus the storage temperature was updated half a year later to 2 °C to 4 °C for one vaccine [9]. While storage temperatures between -80 and -70 °C are considered a safe storage temperature, such cryogenic temperatures restrict the availability and increase the cost of a drug. Taking this and the variety of storage conditions for similar products into account, the need for rapid development of product-specific freezing processes becomes evident. Currently, different freezing solutions including stainless steel vessels and single use bags are used for bulk storage [7], with available small-scale models for freeze bags [10] and actively cooled containers [11]. small-scale models enable process investigations at early stages of pharmaceutical process development and overcome sample shortages [12]. To ensure process comparability, small-scale freeze-thaw models are often validated by mimicking temperature curves from large to small-scale [13]. Furthermore, the distribution of solutes in frozen bulk at the end of the process has been studied [14]–[18]. However, concerns were raised regarding the comparability of small-scale models [19].

Small-scale models may support the approval of new medications and are suggested by regulatory authorities, such as the European Medicines Agency or the American Food and Drug Administration (FDA), who assure the patient's safety. Besides evaluation of drug safety and stability prior to approval, the manufacturer must provide a robust production process to deliver a constant quality even in the event of minor production deviations. The Quality-by-Design (QbD) concept is used to identify and reduce manufacturing errors [20] and thus improve the production robustness. The idea behind the concept is, that manufacturing processes should be designed with process knowledge which leads to quality built into the process. Within this approach, critical quality attributes (CQA) are defined that must be met at the end of each production batch. Common tools to monitor CQAs throughout the process are referred to as Process Analytical Technology (PAT), which often provide real-time process information. High-throughput experiments and multivariate data measurements are frequently used techniques to provide the data necessary to comprehend complex processes and to find suitable process conditions. PAT in combination with small-scale models can demonstrate the impact of possible process variations and process robustness. Furthermore, critical process parameters (CPP) that influence CQAs should be identified and their impact understood.

Recently, in-silico process modelling has become an import tool for the biopharmaceutical industry [21] to support process development. Mechanistic models find application in the optimization and prediction chromatographic separations. On the other end, stochastic models are often used for interpolation of experimental results with limited predictability. Mechanistic models, however, often require intense calibration, precise knowledge of the physico-chemical process properties and large computational power.

In the following chapter, the background of freezing processes as well as the used analytical technologies are briefly introduced. In the last section, an overview of computational fluid dynamics is presented as a mechanistic model to describe freezing processes.

1.1. Protein stability in freezing processes

Proteins are highly structured polypeptides. The backbone chain is built from amino acids, referred to as the primary structure. With increasing protein size, the protein sub-domains form secondary, tertiary and quaternary structures with inter- and intramolecular forces such as Van-der-Waals, Coulomb or hydrogen bonds. The complexity of proteins leads to sensitivity and degradation in non-suitable environments. The main chemical degradation pathways involve oxidation, deamidation and carbonylation. Physical degradation may occur due to mechanical shear stress and surface interactions.[22] As a result, therapeutic proteins may form variants such as high and low molecular weight species. This may result in reduced efficacy or induce immunogenic reactions [23]. Thus, prevention of protein degradation is of importance, and biopharmaceutical drug formulations are carefully selected for their long-term stability. Evaluated formulation parameters include pH, ionic strength and suitable additives. For example, a pH shift in a formulation may lead to increased chemical degradation the primary structure [24] and reduced solubility [25]. Additives such as sugars, surfactants or antioxidants can further improve the long term stability of biopharmaceutical formulations [24] by prevention and reduction of chemical stresses. On the other hand, protein aggregation or crystallization occur at elevated proteins concentrations [26] leading product degradation.

A key process parameter influencing the long-term stability is the storage temperature. In general, low temperatures reduce chemical reaction rates and slow down degradation. However, cold denaturation of proteins at low temperatures has been reported similar to heat denaturation, as described by the Gibbs free energy. The Gibbs energy difference between the native and denatured state of a protein is a parabolic function over temperature with a maximum typically located between 20 °C

and 40 °C. This is a result of temperature dependent interaction between water molecules and non-polar groups located within the protein at native state. Thus, at temperatures far from the protein's maximum stability, the denatured state is thermodynamically favored. [27]

In addition to cold denaturation, therapeutic proteins are exposed to a number of stresses during freeze-thaw processes [28]. One driver is the freeze or cryo concentration of the solutes. The crystallizing water molecules exclude solute causing solute gradients in the frozen bulk. On a microscopic level, this leads to a distribution of solutes between the ice crystals [29] and a partial dehydration of the remaining liquid phase. From macroscopic view, solutes are concentrated at the freezing front causing changes in the physical properties of the solution such as viscosity, density and solidification temperature. Furthermore, the protein concentration may increase beyond solubility affecting the stability of a formulation.

As a result of changing concentrations and temperatures, solutes present in a drug formulation may crystallize during freezing. This can cause pH shifts as high as 3-4 pH units reported for common buffer systems such as sodium phosphate [30]. Changes of the pH are dependent on the buffer type and may be reduced by the addition formulation agents such as glycine [31]. However, additives have also been reported to crystallize and induce protein denaturation dependent on their initial concentration [32].

In addition, liquid-liquid phase separation can occur with increasing concentrations during freezing of biopharmaceutical formulations. Liquid-liquid phase separation has been reported for a number of protein formulations [33], [34]. The individual phases are enriched of one component which may lead to a reduction of stabilizing additives or an increase in protein concentration. Therefore, liquid-liquid phase separation should be avoided.

The crystallization of water molecules introduces new surfaces. Ice surfaces possess different hydrophobic properties that may favor interaction with hydrophobic amino acids. As a result, protein surface interactions occur during freezing and has been reported to induce denaturation [35]. The degree of supercooling may offer control over ice crystal morphology such as crystal size and number [36], affecting surface denaturation in the frozen bulk [37]. However, in large scale freezing processes, supercooling occurs only in in areas close to the cooling walls.

In conclusion, temperature and freeze concentration are drivers for many of the described stability issues. In large scale freezing processes, the solute concentration of a sample changes with time and location within a freezing device. Thus, the focus of

the presented work lies on the description and understanding of the mechanisms that lead to heterogeneities in frozen bulks.

1.2. Freeze-thaw processes in the biopharmaceutical industry

Freezing and thawing are unit operations performed at various stages during process development and manufacturing of biopharmaceutical drugs. As a production example, mAbs are commonly manufactured by a platform process as depicted in Figure 1.1. In a first step, the host cell line expressing the protein of interest is cultivated during upstream processing. Second, the drug is concentrated and purified during downstream processing. Here, the removal of process and product related impurities such as host cell proteins (HCP) and aggregates is performed usually by a number of sequential chromatography steps. Lastly, drug product formulation and final fill take place.[38] After formulation, the drug product can be frozen or freeze dried for long term storage. The individual process steps are operated by individual departments, that hand over their product with minimal hold times in between. While up-, downstream and formulation are often located on the same manufacturing site, the final fill may be performed decentralized, which requires transportation of bulk material.
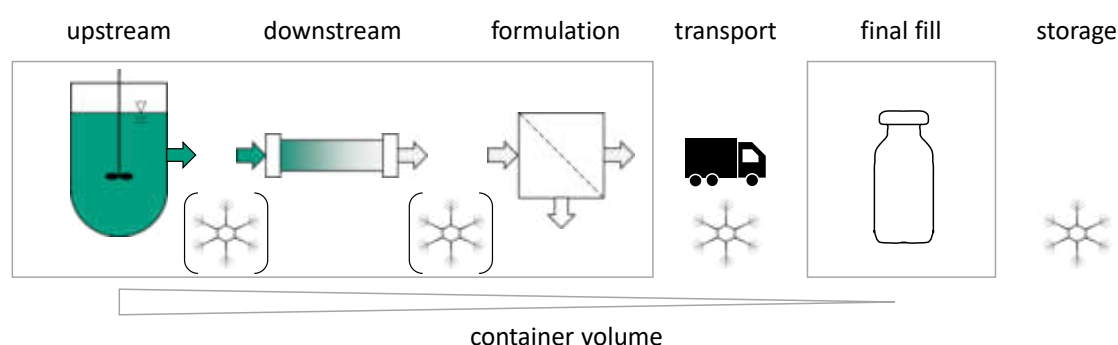
Figure 1.1: schematic of biopharmaceutical manufacturing operations with freeze-thaw steps. Potential freeze-thaw steps are marked by parenthesis. Locally separated manufacturing sites are indicated by grey rectangles.

During the manufacturing and process development, bottlenecks in the production line, process unit failures and transportation in between locations and departments may require a freezing step to assure product integrity. Throughout the production, process parameters such as bulk volume may change and have to be considered for freeze-thaw process optimization. To satisfy volume requirements, a variety of freeze-thaw containers is commercially available as summarized in Table 1.1. In general, industrial freezing processes can be categorized into active and passive processes. During passive, containers are placed into freezers or cold rooms. Actively cooled

samples, on the other side, are frozen using cooling fluids for heat removal. As a result, the heat transfer in active freezing processes is faster compared to passive processes, where stagnant air is used. So called 'blast freezers' improve the heat transfer rate in passive freezer by air circulation [39], but are still slower than active freezing. For smaller volumes, flash freezing by immersion in liquid nitrogen is commonly performed. However, this process is poorly scalable, expensive and challenging to handle at larger scales. Selecting the material of the container, single-use materials are often used to reduce costs of equipment and avoid cleaning [40]. Compared to stainless steel containers, single-use applications are limited to smaller volumes and, in some cases, to minimum freezing temperature. Upon freezing, polymer films tend to become brittle, causing handling problems and container breakages.

For both passive and active freezing processes, scale down models are commercially available. However, data available on the validation of scalability is often restricted to temperature profiles from a single probe and rarely concentration profiles in the frozen bulk.

Table 1.1 Overview of commercially available freeze-thaw containers. Examples for materials and specified freezing temperature according to manufacturer. PET: Polyethylene terephthalate; Min T_f: minimum freezing temperature

	Jacketed Vessel	**Single-use bags**	**Single-use bottles**
Volume	10 – 300 L	0.03 – 17 L	< 2 L
Material	Stainless steel	Not specified Polymer	PET
Cooling	Active	active or passive	passive
Min T_f	-80 °C	-80 °C	-40°C
Example	ZETA FreezeSystem (ZETA, Graz, Austria)	Celsius® FFTp (Sartorius, Göttingen, Germany)	Corning PET media bottles (Corning, Tewksbury, MA, USA)

1.2.1. Freezing of multicomponent solutions

Freeze-thaw processes can be divided into four main stages: cooling (I), freezing (II), isothermal hold (III) and thawing (IV), as schematically shown in Figure 1.2. During the cooling phase, the solution is cooled starting from the initial temperature. Eventually, the temperature drops below the freezing temperature (T_f) which is referred to as 'supercooling'. The following stage is initiated by the spontaneous
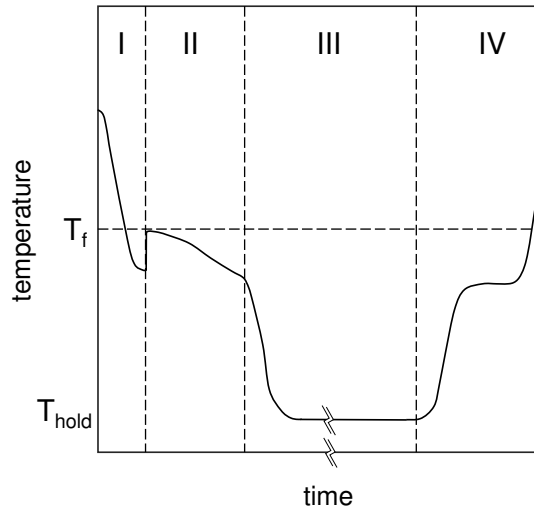
Figure 1.2: schematic temperature profile during a freeze-thaw process. Stages I to IV represent cooling, freezing, isothermal hold and thawing, respectively. T_f: freezing point temperature. T_{hold}: storage temperature.

crystallization of water molecules. The nucleation is a stochastic event caused by Brownian motion, among other factors, and is discussed in Chapter 1.2.2. Upon solidification, the heat of fusion is released, resulting in a sudden temperature increase of the sample temperature. Starting from the first nuclei, freezing continues and the concentration in the liquid phase increases. As a result, freezing point depression occurs [41] and the temperature in the remaining liquid phase decreases during freezing. At the end of the freezing phase, annealing can be used to increase the ice crystal size by Ostwald ripening. Therefore, the temperature is oscillated between the melting temperature and the storage temperature. Annealing often applied in freeze-drying processes to improve the drying kinetics [42]. After the entire bulk is frozen, stage three begins by a rapid temperature decrease due to the lack of released latent heat. The storage temperature (T_{hold}) is hold for the required and proven shelf life. In the last thawing phase, melting of the crystals is induced by increasing the temperature above the freezing point temperature.

Biopharmaceutical formulations are aqueous multicomponent solutions containing the drug and stabilizing additives such as buffer components or sugars. During the freezing phase, concentration changes and different phase states will occur in multicomponent solutions. For binary systems, such as sucrose solutions, state diagrams have been thoroughly investigated [43], [44], which describe phase transitions during a solidification process. A schematic phase diagram adapted from Roos et al. [43] is shown in Figure 1.3. During the cooling phase, the liquid solution will be cooled until the equilibrium freezing temperature is reached. Due to freeze concentration in the freezing phase, the concentration in the liquid phase will increase and the liquid temperature will decrease along the equilibrium line, which is also
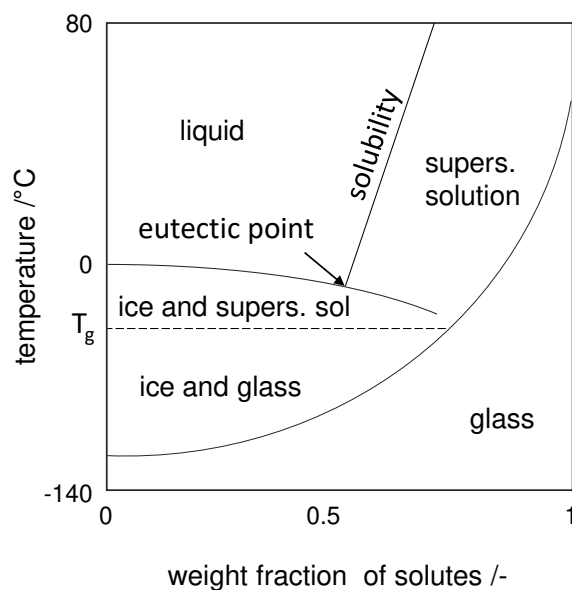
Figure 1.3: schematic phase diagram of a binary solution. Data adapted from [43]. Supers.: supersatured. Sol.: solution

referred to as 'liquidus line'. The solidified part, on the other hand, is composed of ice and supersaturated solution. Following the liquidus line, the eutectic point will be reached at the eutectic temperature T_{Eu}. At the eutectic point, liquid, frozen and crystallized solute are present. With further decrease in temperature, glass forming agents, such as sucrose, will form an amorphous state, known as 'glass state', if the temperature decreases below the glass transition temperature (T'_g). In the glass state, the maximum weight fraction is reached and water solidification stops [45]. The glassy state is important for the formulation stability [46] as the mobility of proteins is hindered by large viscosities [47] exceeding 10^{10} Pa s. Thus, the protein degradation rates are decreased greatly leading to suggested storage temperatures below the glass transition temperature [7]. The glass transition temperature can be determined by differential scanning calorimetry for binary systems, but is challenging to measure for complex solutions [45]. For example, glass transition temperatures between -40 °C and -60 °C have been reported for sugar solutions [48]. Other additive, such as phosphate buffers or trehalose might crystallize instead of forming a glass, if a critical concentration is exceeded [49].

Moreover, the physical properties of the solution change with increasing concentration in the liquid phase. As an examples, the viscosity of sucrose solutions as a function of concentration and temperature has been described by Génotelle [50], among others, and has been used for calculation of viscosities in the supercooled region down to -10 °C [51]. At the same time, the self-diffusion coefficients of solutes change with temperature and concentration as experimentally investigated for sugar solutions

[52]. Viscosity and diffusion coefficients of sucrose solutions have been investigated at sub 0 °C temperatures [51], [53], [54] and are shown in Figure 1.4. With increasing temperature, the viscosity decreases while the diffusivity increases. One reason for this is the influence of viscosity η and temperature T on the diffusion coefficient D, as described by the Stokes-Einstein equation 1-I for ideal spherical molecules [55].

$$D = \frac{k_B\, T}{6\, \pi\, \eta\, r} \qquad\qquad \text{1-I}$$

In the Stokes-Einstein equation, k_B represents the Boltzmann constant and r is the spheres radius.
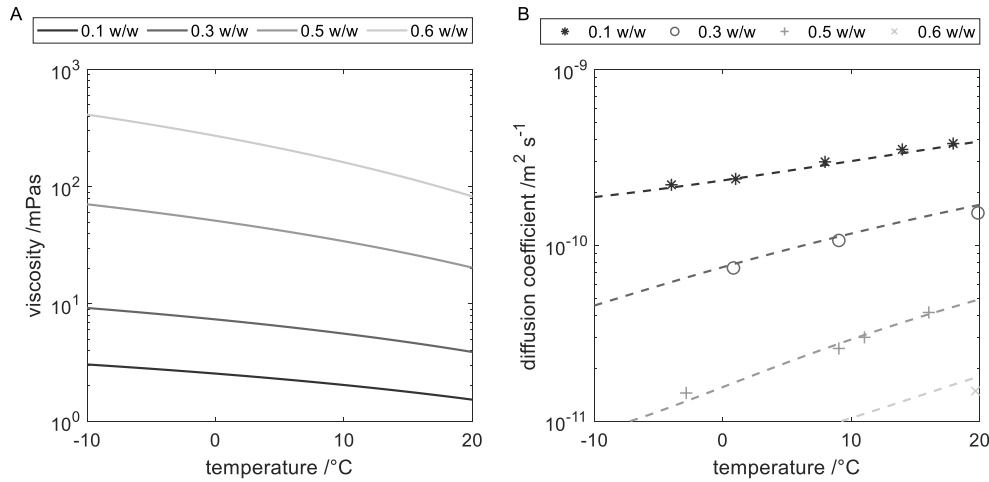
Figure 1.4: Physical properties of a sucrose solution over temperature. Weight fractions (w/w) increase with color gradient form dark to light. **A**: Theoretical viscosity of sucrose solutions calculated after Génotelle [50]. **B**: Diffusion coefficients of sucrose solution with data from [51], [53], [54]. Dashed lines represent second order polynomial regressions to guide the eye.

In addition, the density is dependent on the solute concentration and thermal expansion of water with the density anomaly. While physical properties and phase diagrams are available in literature for solutions such as sucrose and metal alloys, the properties of multicomponent biopharmaceutical formulations are more complex due to the variety of solutes and number of components. Even for similar proteins , different phase behavior has been reported [26]. Thus, either assumptions or in-silico predictions of protein phase behavior in the supercooled region are needed for investigation of such freeze-thaw processes.

1.2.2. Scale-dependent parameters in freezing processes

Due to sample limitations during the process development, small-scale models are a frequently used measure for process optimization and validation. The 'International

Council for Harmonisation of Technical Requirements for Pharmaceuticals for Human Use' (ICH) provides guidelines for the manufacturing of pharmaceutics and defines small-scale models as 'an appropriate representation of the proposed commercial-scale' [56]. Therefore, small-scale models must be validated against data to demonstrate the scalability and appropriateness of the model [56]. In freeze-thaw processes, a representative model should lead to a similar protein stress and CQAs after a freeze-thaw step is conducted. Process parameters, that affect protein stability include degree of supercooling, temperature profiles, freeze concentration and freezing duration. In the following, the parameters will be elucidated in the context of scale dependency.

Degree of supercooling

The degree of supercooling is defined as the difference between the freezing point temperature and the temperature of the solution, when nucleation first appears [57]. Nucleation is a stochastic event induced by Brownian motion, among others. Large degrees of supercooling, rough cooling surfaces and large volumes increase the likelihood of nucleation. Furthermore, particles, such as dust, might act as nucleation sites, which can reduce the degree of supercooling in non-sterile environments [57]. To achieve comparable supercooling, small-scale models should be made from the same material with equal surface roughness and induced nucleation might be necessary [58]. With increasing volumes, large temperature gradients will be found in the sample due to heat transfer limitations. If supercooling occurs in the entire sample, the bulk might freeze instantly, which is often found in high-throughput experiments at microliter scale. In larger freezing processes, however, supercooling will occur close to the cooling walls and freezing fronts will progress towards the center of the container.

Temperature profiles

The removal of heat from the sample is dependent on the ratio of cooling surface area to sample volume. The heat flux $\dot{q}$ can be calculated from Fourier's law,

$$\dot{q} = -\lambda \frac{\partial T}{\partial x} \qquad \text{1-II}$$

with $\partial T / \partial x$ being the temperature T gradient over the heat conducting distance x. The thermal conductivity λ is assumed to be constant for a given material. In case of freezing processes of pure water, however, the thermal conductivity changes considerably from approximately 0.6 W/(K m) for liquid water to 2.2 W/(K m) for ice. The heat flow rate $\dot{Q}$ can be calculated from $\dot{Q} = \dot{q}\, A$, where A is the cooling surface area. Under assumption of negligible influence of the solutes on the thermal

properties, the total heat to be removed ΔH_{tot} until temperature equilibrium in the bulk volume with mass M is reached, can be approximated using equation 1-III.

$$\Delta H_{tot} = M \left(c_{p,l} \, \Delta T_0 + c_{p,s} * \Delta T_{freeze} + \Delta H_{lat} \right) \qquad \text{1-III}$$

The heat capacity of water ($c_{p,l}$) and ice ($c_{p,s}$) are 4.2 kJ/(kg K) and 2.1 kJ/(kg K), respectively. The latent heat (ΔH_{lat}), that is released upon solidification, is approximately -334 kJ/kg. The temperature differences between the initial temperature and the freezing point temperature (ΔT_0) and between the freezing point temperature the storage temperature (ΔT_{freeze}) are overcome during stage I and II in the freezing process. The freezing time can be calculated from integration of the heat flow rate out of the system over time and the enthalpy difference from liquid to solid state ΔH_{tot}. The Planck equation describe the freezing time and is extended and applied in the of food industry [59].

Mushy Zone

While at smaller scales, spontaneous freezing of the entire volume might occur, freezing progresses slowly from the cooling surfaces at large scales. At the freezing front ice crystals grow into solution and the thermal properties change. From a macroscopic point of view, this transition zone is referred to as 'mushy zone', as this zone is neither solid nor liquid. Common crystal shapes described in aqueous systems are columnar, dendritic and amorphous [60] as illustrated in Figure 1.5. The crystal shape is affected by constitutional supercooling and present solutes [7]. In between the crystals, solutes are freeze concentrated as water crystallizes. Depending on the growth rate and crystal shape, freeze concentrated solutes are entrapped within the ice crystal matrix or pushed into the solution. Furthermore, mass transport away from the mushy zone leads to a reduction of freeze concentrated medium in between the growing ice crystals.
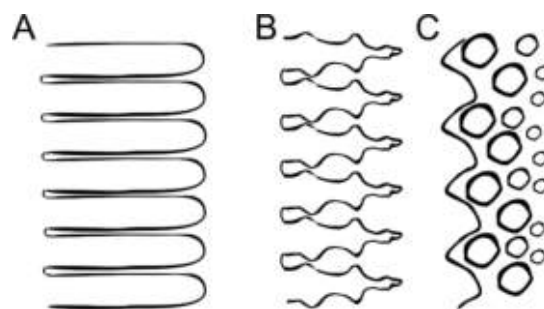
Figure 1.5: Crystal growth in the mushy zone. **A:** Columnar **B:** Dendritic **C:** Amorphous. Adapted from [60].

Introduction

Freeze concentration

From a macroscopic view, the freeze concentration in the mushy zone can be described by a partition coefficient k,

$$k = \frac{c_s}{c_l} \qquad\qquad\text{1-IV}$$

with c_s being the concentration in the solid phase and c_l the concentration in the liquid phase [61]. Partition coefficients have been investigated for solidification of metal alloys [62], [63] and therapeutic formulations [64]. The encapsulated solute concentration is a function of the solute concentration at the solidifying front. In metallurgy, the Scheil and Lever model are used to describe the freeze concentration in a solidification process [65]. While the Lever model takes diffusion in the solid into account, the Scheil model assumes zero diffusion in the solid phase. As freeze-concentration profiles are measured in the frozen bulk, the Scheil model is more likely to describe biopharmaceutical freezing. However, as freeze concentration continues, solute mass fluxes appear that reduce the freeze concentration in the mushy zone.

Solute Mass Transport

Solute mass fluxes can be categorized into diffusion and convection. According to Fick's first law [66], the solute mass flux J along the distance x can be calculated from

$$J = -D\frac{\partial c}{\partial x} \qquad\qquad\text{1-V}$$

where D is the diffusion coefficient and c the solute concentration. Thus, with increasing concentration, the mass flux increases. Under the assumption of no
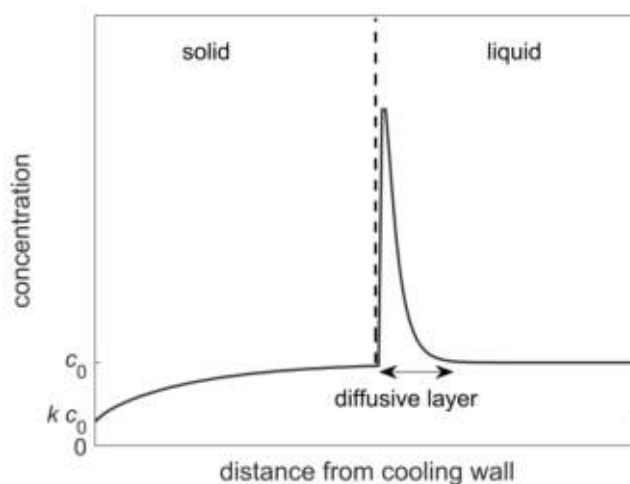
Figure 1.6: schematic representation of a steady state solidification at a specific time. No diffusion in the solid phase and no convection were assumed.

convection and no diffusion in the solid phase, steady state solidification will occur leading to concentration profiles as schematically depicted in Figure 1.6.

The solid concentration at the cooling wall is calculated from the initial concentration c_0 and the partition coefficient k. As freezing continues, solute will accumulate at the freezing front, leading to an increase in the solid concentration. At the same time, a diffusive layer will form, which transports the solute away from the freezing front according to Fick's second law [66] shown in equation 1-VI.

$$\frac{\partial c}{\partial t} = D \frac{\partial^2 c}{\partial x^2}$$

1-VI

Fick's second law describes the solute concentration c variation over time t. The concentration in the solid will increase until a steady state solidification forms, where the solute exclusion due to freeze concentration is equal to the diffusive flux into the remaining liquid. At the end of the solidification, diffusion is restricted due to the approaching boundary and the concentration in the solid will increase. Such steady-state solidifications find use in the solidification of alloys [67]. The steady-state solidification highlights the necessity for small-scale models to have a representative length between cooling surfaces.

Due to freeze concentration and thermal expansion, density gradients will occur in the solidifying volume. As a result of gravity, pressure gradients will form inducing buoyancy-driven convection also referred to as 'natural convection'. Convection phenomena have been investigated for numerous solidification problems such as metals [62], [68], [69] and also for pharmaceutical formulations [18].

Natural convection can be described by the dimensionless Grashof number [70]. The thermal Grashof number describes flow induced by thermal expansion of fluids whereas the solutal Grashof Gr_S number is used for mass transport induced flows and is calculated by equation 1-VII.

$$Gr_s = \frac{g\,\beta_s\,\Delta c\,H^3}{\eta^2}$$

1-VII

The gravity g, the solutal expansion coefficient β_s, the concentration difference in the fluid Δc, the fluid height H and the kinematic viscosity η are used to calculate Gr_s. For thermal Grashof numbers, the solutal expansion coefficient and concentration gradient are replaced by a temperature expansion coefficient and gradient, respectively. In freezing processes, the calculation of Grashof numbers is challenging, as solutal expansion is dependent on temperature and concentration. Additionally, viscosities change with concentration and temperature. Furthermore, the flow at the freezing front is restricted by crystals in the mushy zone [71].

Natural convection driven by solute concentration will occur in a circular motion in a closed cavity, dragging down freeze concentrated solution at the freezing front to the bottom center of the enclosure. In general, mass transport during a freezing process will lead to concentration gradients in the frozen bulk with increasing concentrations towards the center bottom of the freezing container.

1.3. Process analytical technology

Process analytical technology (PAT) by definition of the FDA is a "system for designing, analyzing and controlling manufacturing through timely measurements of critical quality […] attributes" [72]. This broad definition covers a variety of process development and manufacturing aspects, where PAT should be applied. First of all, the design of a manufacturing process should be guided by process understanding so CQAs can be controlled. This step is elucidated in the 'Quality-by-Design' approach introduced by regulatory authorities to increase process robustness [73]. According to the Quality-by-Design approach, manufacturing processes have to be designed and engineering with a profound process knowledge to assure a constant product quality. This process knowledge can be generated early on in the process development by a detailed analysis and characterization of manufacturing processes. It facilitates root-cause-analysis with the aim of identifying prevention strategies [74]. Furthermore, process understanding improves process control to keep the CQAs within a proven acceptable range. Such a proven acceptable range is defined in a process design space, where the impact of critical process parameters (CPP) on the CQAs is defined. In summary, PAT supports the aim of regulatory agencies to ensure patient safety by product quality.

By definition CQAs are quality attributes with a major impact on the drug quality. For biopharmaceutical products, this can be challenging as the product quality of the final drug product is measured by a number of quality attributes, which form the 'quality-target-product-profile'. Common CQAs for products such as mAb are the aggregation level and glycosylation profiles [75]. CQAs investigate in freeze-thaw processes are concentration [15], [76], pH [77], aggregation level [15] and protein activity [77]. Common CPPs for freeze-thaw steps are process dependent, especially the choice of freezer, and may include temperature, cooling liquid flow rates and agitation. For actively cooled freezing processes, CPPs have been tested at pilot scale and freezing temperature, freezing time and container fill level were suggested as most significant [11].

PAT applied in small-scale models might pose a scaling challenge. Scale-dependent process parameters, such as mixing, can lead to different gradients of the measured

variables in larger applications. For instance, substrate gradients in bioreactors have been reported as a function of impeller speed [78]. The observed gradients require sampling at multiple positions to monitor processes accurately, where the number of sampling positions has to increase with the degree of inhomogeneity. Thus, in large-scale freeze-thaw processes, a high spatial resolution of monitored variables is key due to the present convection.

Quality attributes can be measured by process analyzers categorized into off-line, at-line and in-line measurements [72], which deliver process data at increasing frequency in the mentioned order. PAT is often used in context with real-time monitoring. A prominent tool is the high performance liquid chromatography (HPLC) used at-line [79] for real-time process control [80]. HPLC methods are able to quantify product aggregates and charge variants present in the drug product. At-line analytical results, however, are always slightly delayed. Therefore, in-line analytical methods are desirable for improved process knowledge and control. Common in-line methods in the biopharmaceutical industry include pH and oxygen probes and spectroscopy [81]. In freeze-thaw processes, pH probes and in-line temperature sensors find application to control freeze progression and for validation of scaling models. However, data such as solute concentration data and protein activity is currently gathered by off-line analysis from ice samples either by slicing of the frozen bulk or the extraction of drill cores. While having a long-time delay, off-line analytics provide the ability of intense sample preparation and allow for time intensive analytic such as enzyme-linked immunosorbent assays. Furthermore, in-line tools are required to be non-invasive and non-destructive methods in contrast to off-line tools. In the biopharmaceutical industry, spectroscopy is a common example for a non-invasive PAT providing in-line process information.

1.3.1. Spectroscopy

Spectroscopic methods are a frequently used PAT used in biopharmaceutical processing [82]. For example, the absorption of light in the visible and ultra-violet (UV-Vis) spectrum is widely used for quantification of proteins in liquid solutions due to their absorption at 280 nm wavelength. However, not every solute present in a therapeutic formulation absorbs within the UV-Vis spectrum. Other methods, such as vibrational spectroscopy modes are able to provide more complex spectra to identify a large variety of individual components with covalent bonds. Common examples are infrared and Raman spectroscopy.

Raman spectroscopy

Raman spectroscopy as a non-destructive and possibly non-invasive analytical method is a versatile tool applied in biopharmaceutical manufacturing [83]. While being a vibrational spectroscopy tool similar to infrared spectroscopy, Raman spectroscopy measures the light interactions with molecular vibrations instead of the absorption. Upon radiation by a monochrome laser, the photons with a wavelength f_0 interact with the molecular vibrations in several ways as depicted in Figure 1.7.
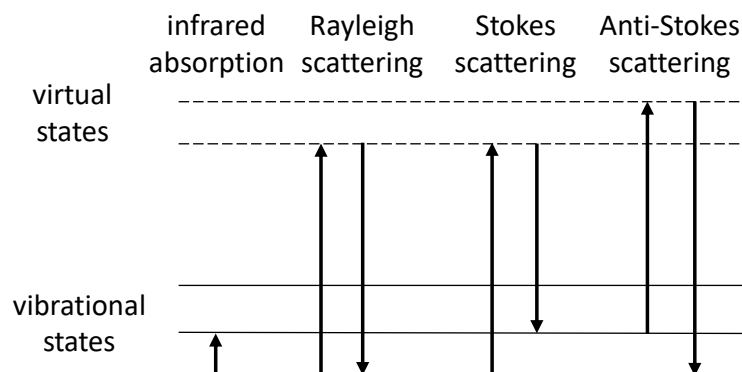
Figure 1.7: Schematic of the interaction of photons with molecular vibrations

First, absorption of the photons may occur leaving the molecule in an excited vibrational energy state. Second, the energy of the photon may lift the molecule from its initial energy state to a virtual state for a short time. In the event of Rayleigh scattering, the molecule falls back from this energetically unfavorable state to the initial state emitting a photon of the same wavelength λ_0. If Stokes Raman scattering occurs, the molecule falls into an excited vibrational energy state instead and emits a photon with shifted wavelength λ_1. In the case of anti-Stokes Raman scattering, the molecule is in an excited state prior to the photon interaction and is put into a lower vibrational state upon interaction with the photon. After anti-Stokes interaction, the photon is shifted to a shorter wavelength. Upon excitation by a monochrome light source, a detector, commonly a charge-coupled device (CCD), measures the scattered light. Typically, the Raman shift Δv is reported as calculated by $\Delta v = \left(\frac{1}{\lambda_0} - \frac{1}{\lambda_1} \right)$.

Unfortunately, Raman scattering signals are comparably low as Raman scattering only occurs in 1 of 10^{10} photon-molecule interactions [84]. As a result, Raman scattering as PAT has been difficult in the past with early measurements taking 40 h [85]. However, recent technology advancements were able to increase the sensitivity drastically, opening new fields of application. Traditionally, vibrational spectroscopy is used to identify and quantify molecules, functional groups and secondary structures of proteins [86], [87]. In the pharmaceutical environment, the applications of Raman spectroscopy vary from raw material characterization [88] to monitoring of

metabolites in upstream processes [89] and to quantifying mAb in downstream processes [90], [91]. In biopharmaceutical freeze-thaw processes, Raman spectroscopy was used to assess microheterogeneity in frozen protein formulations [29] and to monitor secondary structure of proteins during freeze-thaw processes [92].

Raman spectra provide information of scattered light for a range of shifted wavenumbers and thus multivariate data. To extract solute concentrations from the spectra, post-processing of the data is necessary as described in the following.

1.3.2. Multivariate data analysis

In comparison to univariate data, multivariate data consist of measurements with several variables as a result of a measured property. One benefit of multivariate data analysis is the possibility to measure the concentration of each component in a mixture of similar components such as proteins. Especially in spectroscopy, multivariate data are generated, with a measured intensity for each wavenumber. Besides good process analyzers, intensive data evaluation is often necessary to acquire the desired measured parameters. Thus, multi-variate data analysis for spectroscopic data evolved as a separate field of interest known as 'chemometrics'. Recent trends in chemometrics involve the application of artificial intelligence for spectra interpretation with a keen eye on non-linear correlations [91], [93]. Linear behavior, on the other hand, has been modeled using partial least squares regression (PLS), which is one of the main tools used in chemometrics [94].

Principal component analysis is the foundation for PLS. Briefly summarized, it can be applied to reduce set of variables to fewer latent variables known as principal components, which model the result without loss of information. Therefore, principal components are calculated based on the greatest variance in the data set and describe a projection of the original data set with new coordinates.

In a PLS, the correlation between a multivariate data set and number of output variables is modeled. The general idea behind PLS is a principal component analysis for the variables, incorporating information about the structure of the output variables. The resulting correlation is summarized in equation 1-VIII.

$$Y = X\,B^T + E \qquad\qquad \text{1-VIII}$$

The data set X contains n independent observations, e.g. measurements, with m variables, e.g. absorption at different wavelengths. During model calibration, a PLS is used to correlate X with a number of dependent output variables i per observation, leading to an output matrix Y with size n by i. The correlation between X and Y is stored in the regression matrix B by the latent variables. The residues stored in E

describe the prediction error. The regression is calculated by mathematical algorithms, which are explained in detail by Kessler [94]. If multiple output variables are correlated ($i>1$), the method is referred to as PLS2, whereas PLS1 corelates a single output variable.

With an increasing number of latent variables, the residues decrease, as more signal variation is explained. However, in experimental data such as spectral measurements, signal variation occurs from the variation of the output variable, e.g. the solute concentration, as well as signal noise by environmental and device specific conditions. As the noise may vary in between individual experiments, it should not add information to the regression model. A large number of latent variables leads to overfitting of the data, which takes signal noise into account.

To analyze if overfitting occurs, cross-validation methods of a model can be used during calibration. Therefore, the calibration data set is split into a calibration and validation set. The model is trained with the calibration set and afterwards the prediction error for the validation set is calculated. Plotting the prediction error against the latent variables, a minimum can be found, where the optimum number of latent variables for the regression model is found. A common prediction error is the root mean square error, also referred to as root mean square error of cross validation (*RMSECV*) in case of cross validation. It is calculated after equation 1-IX,

$$RMSECV = \sqrt{\frac{\sum_{i=1}^{n}(y_i - \hat{y}_i)^2}{n}} \qquad \text{1-IX}$$

where n is the total number of cross-validation observations, y_i is the output variable of one observation i and $\hat{y}_i$ is the predicted output variable.

1.4. Computational fluid dynamics

Freeze-thaw processes can be described as a heat transfer and fluid mechanical problem with changing physical properties and solute compositions as described earlier. To generate a better process understanding and possibly predict the behavior of varying process parameters, mechanistic models and digital twins are used. A mechanistic model to approach fluid mechanical problems is computational fluid dynamics (CFD). CFD can aid the optimization of process design and support process approval by the FDA [95]. CFD iteratively approximates the flow behavior by numerical analysis, solving the fundamental fluid equations. CFD finds application in various fields from climate simulations [96] to the optimization of heat transfer [97]. Additionally, it has also been used to study solidification processes [68], [98]–[100]. Furthermore, scale-up studies have been conducted by CFD.

The Navier-Stokes equation lays the mathematical foundation to describe pressure driven flow of viscous fluids. It resembles a continuity equation derived from the conservation of momentum. For liquids, a negligible compression can be assumed and the Navier-Stokes equation for incompressible flow can be denoted as follows:

$$\rho \left(\frac{\partial \vec{u}}{\partial t} + (\vec{u} \cdot \nabla)\vec{u} \right) = -\nabla p + \mu \Delta \vec{u} + \vec{f} \qquad \text{1-X}$$

The variable ρ represents the density, $\vec{u}$ the velocity, p the pressure, μ the dynamic viscosity and $\vec{f}$ any external force. A frequently occurring external force is the gravity, which is important for buoyancy driven flows that occur in solidification processes. To mechanistically describe fluid motion and heat transfer, the Navier-Stokes equation is supplemented by equations for the conservation of mass and energy, which can be extended by additional models such as solidification. The resulting set of non-linear partial differential equations has not yet been solved analytically. Thus, CFD approaches an iterative solution of a specified case by discretization of space and time. For space discretization, finite-element, finite-difference and finite-volume methods have been used by different software application.

To perform a CFD simulation, the problem and its boundary conditions need to be defined. First, the geometry is defined using computer aided design (CAD), from which a mesh is created, that slices the geometry into either finite volumes, elements or equally distant points depending on the type of method. The model accuracy and the computational effort increases with an increasing number of elements and therefore computational error has to be evaluated against grid size in a mesh study. In a next step, the physical boundaries for a problem need to be defined, such as fixed value boundaries called 'Dirichlet', e.g. the temperature at a cooling wall. Afterwards, the set of analytical equations is numerically approximated for each grid element at each time step by a suitable solver such as the semi-implicit method for pressure linked equations (SIMPLE). While large time steps significantly reduce the total computation time, they may lead to inaccuracies in the predictions. In summary, the solution accuracy has to compared against computational effort and thus simulation time with regards to time step and mesh resolution.

For calculation of CFD problems, a number of software solutions are available, which can be categorized by the method of spatial discretization or by availability. First of all, the equations can be hard coded, giving the user full flexibility. However, open source software packages are available, that have been improved over several years with regards to numerical stability and use of resources. A prominent open source package is OPENfoam. Commercially available software, such as ANSYS Fluent or COMSOL, provides a more user-friendly experience with supportand graphical user

interfaces. In addition, commercial software packages provide with a variety of implemented models such as solidification and species models, which are necessary to investigate freeze concentration behavior.

The topic of CFD is certainly complex with a variety of options to choose from. In the presented work, the focus was laid on the applicability of available software packages to model and predict freeze concentration.

2 Thesis Outline

2.1. Research Proposal

In 2020, numerous vaccines have been explored at peak process development intensification to control the COVID-19 pandemic. Categorized as biopharmaceuticals, the vaccines contain biologically derived active pharmaceutical ingredients (API), which are usually highly structured macromolecules. Biopharmaceuticals are prone to degradation, leading to a short shelf life at room temperature. Hence, freeze-dried or frozen formulations are favored for transport and long-term storage of biopharmaceuticals to assure drug integrity and patient safety. In general, low storage temperatures in the range of -80 to -70 °C are considered a safe option with regards to the product stability. However, cryogenic storage temperatures increase cost of transportation by manifold and restrict handleability and availability of the drug. In the past, API stability and formulation studies have been time and sample volume costly, leading to uncertainties in the necessary storage temperature. To address this, high-throughput screening approaches at microliter-scale have been proposed recently. However, at larger scales, freezing of liquid formulations induces mass transport phenomena, which are neglected in microliter-scale screenings. Freeze concentration at the freezing fronts caused by the exclusion of solutes from the crystallizing water causes diffusion and buoyancy driven convection. Small-scale models offer the possibility to investigate the mass transport, while reducing the product consumption and thus filling the gap between high-throughput and manufacturing scale.

Therefore, small-scale models are suggested by regulatory authorities to support the process validation and can be used to create process understanding as required by the 'Quality-by-Design' (QbD) initiative to ensure consistent drug quality and thus patient safety. This involves the identification of critical process parameters (CPP) and critical quality attributes (CQA). The implementation of process analytical technology (PAT)

to monitor process and quality parameters enables process control and contributes to a robust and reliable manufacturing process.

The focus of this work is to identify and monitor CPP and CQA in biopharmaceutical freezing processes and to facilitate future process design and optimization by an improved process understanding.

In a typical freezing container, the temperature is often monitored by a single or a few temperature probes. The determination of freezing by temperature relies on the knowledge of the freezing temperature. The freezing process is considered to be completed after the freezing time, when the sample temperature at the last point to freeze (LPTF) drops below the freezing temperature. As a result, freezing times are underestimated if single temperature measurements are not performed at the last point to freeze. Furthermore, they might be overestimated if freezing point depression is not considered, which increases due to ongoing freeze concentration. As freezing times can be used to compare different freezing processes such as actively cooled vessels or passively cooled bottles in freezers, an accurate determination is required. It was the aim of the first part of this thesis to overcome the mentioned challenges by improved temperature tools and investigate freezing time as a CPP. A temperature-based monitoring of the freezing progression further enables the investigation of model assumptions such as controlled boundary conditions.

Temperature-time profiles of freezing containers have been used to validate small-scale models. However, in biopharmaceutical solidification processes, temperature is mostly independent from the buoyancy-driven convection. Therefore, similar temperature profiles may not lead to comparable concentration gradients in the frozen bulk. Furthermore, freeze concentration in multi-component solutions may lead to separation of solutes and thus destabilization of the API. To date, biopharmaceutical freeze concentration in large scale freezing containers has been investigated from frozen samples. This method can be used to correlate concentration gradients in frozen bulks to process parameters but lacks of transient information on their origin and is a destructive analytic. A real-time monitoring of freeze concentration is yet missing. The second part of the presented work addressed this topic. Once established, the novel PAT was applied to investigate the impact of freezing process and formulation parameters on freeze concentration.

Besides small-scale models, in-silico models are attracting increasing attention from the biopharmaceutical industry for process optimization and prediction. Computational fluid dynamic (CFD) models were used to describe solidification in casting processes providing a potential framework to simulate biopharmaceutical

freeze concentration. Among the available software, commercial CFD packages claim to facilitate simulation by increased numerical stability and a variety of implemented models. After experimental investigation of transient temperature and concentration profiles, the predictability of the CPP freezing time and the CQA freeze concentration was investigated using commercially available CFD software in the third part of the thesis.

In the biopharmaceutical industry, freeze-thaw processes have been used for decades to increase the product shelf life. mAbs, which are among the top selling drugs worldwide, are produced using a platform process approach, where only minor changes are applied in between different products. During process development, process intermediates often have to be frozen due to timeline and project restrictions. In manufacturing, however, process intermediates are directly processed to avoid possible product degradation. A further study aimed at investigating the comparability of process development and manufacturing processes by measuring CQAs in process intermediate that were subjected to different freezing scenarios.

In summary, this work aims to address knowledge gaps identified in the understanding of biopharmaceutical freezing processes by identifying and monitoring CPPs and CQAs.

2.2. Comprehensive Overview

In this section, a list of the research papers is given followed by a brief summary. The author contributions signed by the respective authors are attached in the Appendix of the examination copy.

Chapter 3: Temperature based process characterization of large-scale pharmaceutical freeze-thaw operations

Dennis Weber, Jürgen Hubbuch

Frontiers in Bioengineering and Biotechnology (2021), volume 9, article 617770

In this study, a novel small-scale device has been used to demonstrate process characterization of freeze-thaw processes. The implementation of a temperature array with high spatial resolution in combination with advanced data analysis allowed for precise monitoring of the freezing progress and the solid phase. Purified water and concentrated buffer solutions served as model fluids. The degree of freeze concentrated buffer measured from ice core samples was correlated with the total freezing time, where lower temperatures resulted in faster freezing and increased frozen bulk homogeneity. Additionally, the freezing temperature in combination with freeze concentration had an impact on the last point to freeze. The observed freezing times were put into context with theoretical calculations and revealed process limitations by cooling units, that are relevant for large scale industrial applications.

Chapter 4: Raman spectroscopy as a process analytical technology to investigate biopharmaceutical freeze concentration processes

Dennis Weber, Jürgen Hubbuch

Accepted (31.08.2021) by Biotechnology and Bioengineering

In Chapter 4, the freeze concentration of solutes in the liquid phase was monitored on-line by raman spectroscopy. Multivariate data analysis was used to measure the concentrations of up to three individual formulation solutes from a single spectrum. The model was validated by samples taken next to the raman probe and analyzed off-line. Throughout the process, solute separation was shown and the freezing time, identified as a critical process parameter, was shown to influence freeze concentration. The results led to an improved process understanding by demonstrating the importance of convective and diffusive mass transport phenomena in biopharmaceutical freezing processes. Furthermore, the impact of the additive concentration in a drug formulation on the freeze concentration was demonstrated

using an industrially relevant product, where higher additive concentrations increased the overall freeze concentration.

Chapter 5: Applicability of available computational fluid dynamic models to predict biopharmaceutical freezing processes

Dennis Weber, Jürgen Hubbuch

Unpublished

The concentration and temperature profiles generated in the previous studies were used to investigate the applicability of available CFD models for the prediction of freezing processes. In the first part of the study, freezing times were predicted using pure water as a model fluid and the enthalpy-porosity method to describe solidification. After the independency of the solution was shown by mesh and time step studies, freezing times were predicted at freezing temperatures from -60 to -20 °C. The simulated freezing times agreed with experimental measurements. However, the predictions were marginally shorter than experimentally determined, which was attributed to experimental boundary conditions. In the second part, the model was extended by a second component to simulate freeze concentration of a sucrose solution. While general buoyancy-driven convection could be simulated, a time step study revealed discretization issues, which were observed by mass imbalances of the solute. As a conclusion, the enthalpy-porosity model in conjunction with the species model as implemented in the used software package might not be appropriate to predict freeze concentration.

Chapter 6: Impact of freeze-thaw processes on monoclonal antibody platform process development

Dennis Weber, Christian Sittig, Jürgen Hubbuch

Biotechnology and Bioengineering (2021), volume 118, issue 10

In this article, the comparability of process development and the manufacturing process for monoclonal antibodies was investigated, with the latter omitting intermediate freezing. Therefore, cell culture supernatant containing mAb was subjected to an additional freeze-thaw cycle at temperatures from -60 to -20 °C and subsequently filtered and captured by affinity chromatography. Critical quality attributes were monitored after each process step. An improved host cell protein and aggregate reduction after the purification step was attributed to freeze-thaw stress induced by elevated freezing temperatures. As a hypothesis, the aggregation of specific host cell proteins and antibody aggregates is suggested. Furthermore, freeze

concentration of individual host cell proteins and antibodies was correlated with protein size as a result of protein diffusion. Overall, this study highlights the importance of a freezing procedure evaluation in a frequently used product platform.

3

Temperature based process characterization of large-scale pharmaceutical freeze-thaw operations

Dennis Weber[1], Jürgen Hubbuch[1*]

[1] Institute of Engineering in Life Sciences, Section IV: Biomolecular Separation Engineering, Karlsruhe Institute of Technology (KIT), Karlsruhe, Germany

*Corresponding Author

Abstract

In biopharmaceutical production processes, freeze-thaw operations are used to ensure product integrity during long hold times, but they also introduce additional stresses such as freeze concentration gradients that might lead to a loss of protein activity. Process characterization of freeze-thaw operations at different scales should be conducted with attention to freezing time and boundary effects to ensure the product stability throughout the process and process development. Currently, process characterization often relies on one or very few temperature probes that detect freezing times based on raw temperature, which is largely influenced by freezing-point depression in case of concentrated solutions. A method to detect freezing based on the second derivative of temperature measurements from Fiber-Bragg-Grating sensors is presented to overcome this issue. The applicability of the method is demonstrated by process characterization of a novel small-scale freeze-thaw device with minimized boundary effects using freezing times of purified water and concentrated formulations. Freezing times varied from 35 to 81 min for temperatures between -60 and -20 °C and impacted freeze concentration profiles. Furthermore, freezing time estimations based on the Plank equation revealed model limitations due to start-up temperature gradients, that can be corrected by an empirically extended Plank model. As a hypothesis, we conclude that freezing temperature, from a freeze concentration view,

is less important in containers with small characteristic freezing distances such as freeze bags. Using a 2D-resolved temperature profile, a shift of the last point to freeze position from top to bottom of a container was observed when freezing above -30 °C.

3.1. Introduction

Therapeutic proteins are among the top selling pharmaceuticals. Due to their high value and production cost, activity loss of the active pharmaceutical ingredient (API) during shipment and storage has to be limited by selection of suitable formulation agents [46], [101] and storage conditions. Therefore, many biopharmaceuticals are stored in a frozen state [102], [103]. While freezing slows down and reduces degradation reactions of the API, freezing processes expose the protein to different stresses such as cold denaturation [27], freeze concentration [28], ice crystal formation [35] and potential excipient crystallization. Protein activity loss or aggregation were correlated with freeze concentration [11], [104]. At a microscopic scale, crystallization of water molecules leads to freeze concentration of the remaining solutes within the ice crystal structure causing freezing temperature dependent phase behavior of proteins [37], [105]. In large scale freezing operations, macroscopic freeze concentration leads to non-homogeneous solute distribution profiles. During freezing of larger bulk volumes, ice fronts progress from cooled container walls towards the center of the container. While freezing, solutes are concentrated in front of the phase boundaries and partition between solid and liquid phase [28], leading to macroscopic freeze concentration. Additionally, this freeze concentration effect leads to natural convection due to density gradients [64] and therefore settlement of solutes. As a result with the occurrence of freezing fronts, a typical freeze concentration profile with the peak concentration at the center bottom of a frozen bulk is unavoidable, if the container bottom is not cooled [15], [104], [106], [107] .

Freeze concentration was shown to be dependent on the freezing process rather than storage temperature [14]. Investigations of freeze-thaw characterizations with a focus on heat transfer and phase change are missing [108], but necessary to ensure process scalability and allow process optimization with regards to ideal freezing temperature. A key parameter often used for characterization of freezing processes is the ice front velocity, which impacts the maximum freeze concentration [14], [16], [19] and the total freezing time. The freezing time determination is commonly based on crude temperature measurement at the last point to freeze (LPTF), where the ice fronts come together at the end of a freezing process. This calculation relies on the assumption of ice below the freezing point temperature which is often arbitrarily set from -0.5 [16] to -5 °C [17] due to freezing point depression. Furthermore, the temperature probe has to be exactly at the LPTF position. A method for determination of the freezing time

independent from freeze point depression and the LPTF position has not been presented. In a recent publication, the Plank equation was suggested to model total freezing times of pharmaceutical processes [102], which allows for process time prediction and optimization. To date, a validation of the model in pharmaceutical freezing processes, however, is missing [102].

In the following work, a derivation-based temperature analysis for the detection of the total freezing time is presented. This method is used for process characterization of a novel small-scale freeze-thaw model with regards to freezing times at different temperatures. The applicability of the Plank equation on actively cooled pharmaceutical freezing processes is discussed to improve transferability of freezing processes to different scales and freezing setups. An extension of the Plank equation is introduced for correction of transient start-up conditions.

3.2. Materials and Methods

3.2.1. Sample Preparation

All used solutions were prepared with ultrapure water (PURELAB Ultra, ELGA LabWater, Veolia Water Technologies, Saint-Maurice, France) and sterile filtered using a 0.2 µm filter prior to application. As TRIS buffer is a widely used buffer in protein formulations [109], TRIS buffer was prepared from Tris-(hydroxymethyl)-aminomethane purchased from Merck (Darmstadt, Germany) and Tris-(hydroxymethyl)-aminomethan-hydrochlorid purchased from Applichem (Darmstadt, Germany) at a concentration of 500 mM. The pH was adjusted to pH 7.5 ± 0.1 using hydrochloric acid. TRIS buffer was selected at elevated concentrations due to its common use in formulations and for better comparability with highly concentrated pharmaceutical formulations that are usually freeze-thawed. Furthermore, freezing point depression is dependent on solute concentration, which emphasize the need for new method for total freezing time calculation. Similar concentration effects are expected for varying solutes such as proteins and stabilizing sugars [16].

3.2.2. Novel small-scale freeze-thaw device

A novel small-scale freeze-thaw device was designed and manufactured together with Bilfinger Industrietechnik Salzburg GmbH, Schwetzingen, Germany. It is designed as a scale down model of an industrial scale freezing unit representing a slice of a larger hollow tube. The hollow cylindrical shaped freezing unit, depicted in Figure 3.1, is cooled by an outer cooling jacket and an inner cooling tubing, while the bottom is heated separately to minimize scale-down boundary effects. The container volume is divided into six individual chambers by an inlay made from polytetrafluoroethylene (PTFE). This inlay allows to perform up to six individual experiment at a working volume of up to 90 mL per chamber. Furthermore, the PTFE also balances the heat fluxes at the bottom of the chamber due to the low heat conductivity resulting in a temperature profile as illustrated in cross-section in Figure 3.1. This PTFE bottom counteracts boundary effects present due to heat conductivity of the steel walls. The outer and inner cooling walls are made from 3 mm thick, 316L stainless steel and have a radius of 38 and 100 mm, respectively. The chamber depth is 40 mm. All tubing and steel parts are insulated using 20 mm Armaflex from Armacell (Münster, Germany).
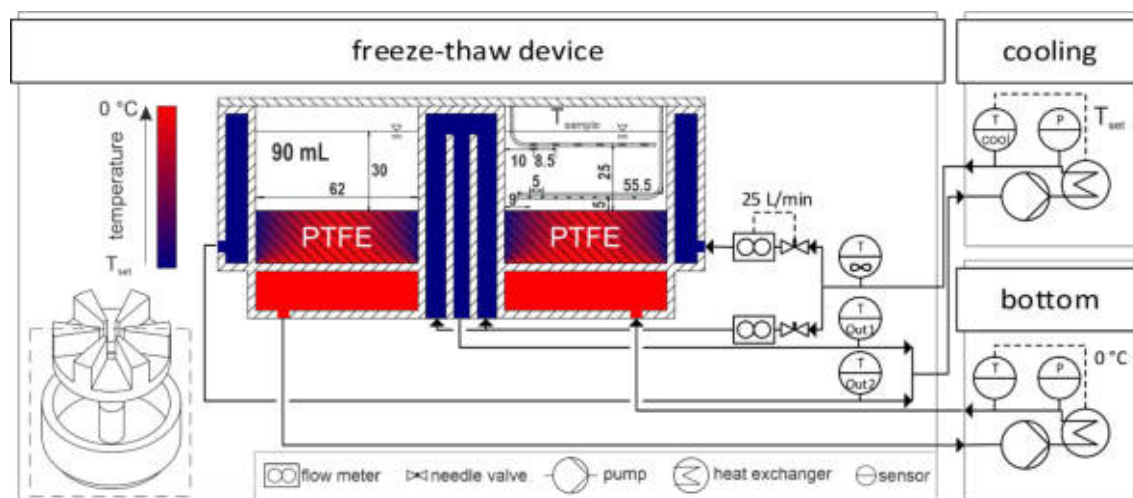
Figure 3.1: Experimental setup. A piping and instrumentation diagram of the cryogenic device with the two individual cooling units to control the freezing chambers is displayed. Freezing chambers are visualized as a cross-section of the small-scale freeze-thaw device is displayed as indicated in the lower left corner. Temperatures of cooling fluids and PTFE inlay are indicated by a gradient from T_{set} to 0 °C in blue to red, respectively. Inside the cross-section, sample temperature probes and dimensions in mm are shown. Pipes are represented by arrows. Hatched areas indicate solid stainless steel and PTFE.

A piping and instrumentation diagram of the freeze-thaw device is depicted in Figure 3.1. In order to achieve the desired temperatures, the inner and outer cooling circuits of the device were merged and connected to the cryogenic device Integral XT 1590 with the cooling fluid Kryo 90, both purchased from Lauda (Lauda-Königshofen, Germany). With installed flow meters from Krohne (Duisburg, Germany), needle valves and a set system pressure of 2 bar, a cooling fluid flux of 25 ± 5 L/min was achieved in the inner and outer circuit. The bottom of the container was heated by the cooling unit F25-MC used with the cooling fluid Thermal HY both purchased from Julabo (Seelbach, Germany). In a preliminary study, a constant bottom temperature of 0 °C was found to be ideal for minimal boundary effects indicated by parallel freezing fronts in the container, when freezing double deionized water (data not shown). All units where operated at maximum power without any set temperature gradients. PT100 thermoelements connected to a datalogger ALMEMO 8590 by Ahlborn (Holzkirchen, Germany) measured the cooling fluid temperatures on-line at the inlet of the freeze-thaw device before stream division and at the two outlet streams from the inner and outer circuit. The setup allowed for set temperatures from -60 to 30 °C. Measured data were collected and controlled using a custom app designed with MATLAB App Designer by Mathworks (Natick, MA, USA). The app automatically collected and set all temperature data on-line from the datalogger, the two cooling units and the sample temperature device described above. In the following sections, the cooling temperature $T_{cooling}$ refers to the temperature of the Kryo 90 cooling unit, while the bottom temperature was set to a constant temperature of 0 °C for all experiments. The fluid temperature T_∞ refers to the measured temperature at the inlet of the cryogenic device. The set temperature T_{set} is the temperature achieved in the cooling unit ($T_{cooling}$) after cooldown.

Prior to an experiment, the gaps between the PTFE inlay and the housing were sealed using food grade silicone Ottoseal S27 from Otto-chemie (Fridolfing, Germany). For each experiment, 90 mL of the sample was pipetted into a chamber. Neighboring chambers were filled with ultra-pure water to minimize radial boundary effects. A freezing process started with a hold phase at 5 °C for at least 2 h to assure equilibrium starting conditions. After equilibration, the set temperature was adjusted between -60 °C and -20 °C at maximum cooling ramp. After all sample temperature sensors measured temperatures below -1 °C, the bottom heating unit was turned off automatically to achieve minimal sample temperatures. If frozen samples were taken, a hold time of 2 h was added post freezing to assure that the freezing process was at equilibrium. After the freezing step, thawing was initiated by setting the temperature to 30 °C for at least 1 h. Timing of the different phases was automated using the app described above.

3.2.3. Temperature evaluation

The sample temperature was monitored using 14 temperature sensors as shown in Figure 3.1 with information on the probes' coordinates. The sensors were located on two pre-calibrated optical temperature fibers in a custom design from Loptek (Berlin, Germany) together with the interrogator SCN-46 S-line Scan 416 from Sylex (Bratislava, Slovakia). These fibers were encapsulated by a stainless-steel tubing of 1 mm diameter and contained up to nine Fiber-Bragg-Grating sensors. One fiber with 6 sensors was positioned 5 mm below the sample surface and a second fiber with 8 sensors was positioned 5 mm above the ground of the chamber to achieve a 2D-resolved temperature field of a chamber cross-section. Temperature data were obtained every 2 s using S-line Sentinel Software from Sylex (Bratislava, Slovakia). The used temperature monitoring set-up provides the benefits of increased temperature resolution while reducing heat conduction through the sensor cables when compared to commonly used thermoelements. We do not expect, that heat conduction along the sensors influences the freezing process, as the heat capacity of the hollow 1 mm thick tubes is negligible compared to the surrounding ice and water.
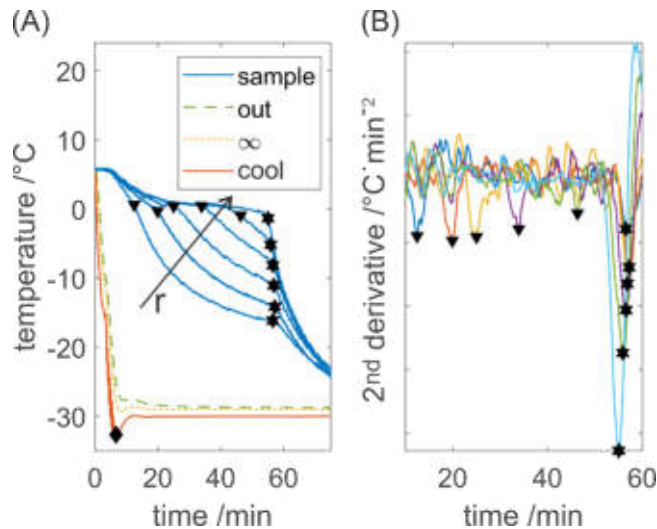
Figure 3.2: Process temperatures evaluation example. **A:** displays the measured device temperatures T_{out}, T_∞, and T_{out} and five out of 13 sample temperatures. The diamond shape indicates the cooldown time, triangle shows the freezing at an individual probe and hexagons show the LPTF. Freezing at individual probes and the LPTF time are calculated based on minima in the second derivative of the sample data, which is shown in **B**. r indicates the increasing distance of the temperature probe from the cooling surface. Individual sample temperature profiles are colorized in B for visibility.

Looking at a typical sample temperature profile as shown in Figure 3.2A, two distinct phase transition times can be detected. The first transition occurs upon freezing at the

observed temperature probe, where the temperature drops below the melting point, referred to as partial freezing time. At this point, thermodynamic properties change from water to ice, leading to a distinct variation of the temperature slope. The second event indicates freezing at the LPTF, which is referred to as total freezing time. When the entire bulk is frozen, no more latent heat will be released and thus, temperature at all probes will decrease simultaneously. For analysis of the two times measured with each temperature probe, the temperature profiles were smoothed and derived twice using a Savitzky-Golay-Filter, with a second order polynomial and a window of 151 data points. Minima in the second derivative indicate the discussed slope changes. The filter window should be carefully selected based on the data quality as discussed later, where smaller windows result in higher precision but also higher signal to noise ratio. The freezing time was calculated based on all 14 temperature measurements, with outliers based on three scaled median absolute deviations removed to improve calculation robustness. However, partial freezing times were determined based on temperature below -2 °C, due to the low signal to noise ratio of the used fiber optic sensors. When this method was applied to temperature readings from thermoelements, both partial and total freezing time could be analyzed based on second derivative.

The cooldown time until the cooling fluid reached the set temperature was calculated based on the minimum temperature of the set temperature.

3.2.4. Freezing time prediction

Plank's model to calculate the total freezing time $t_{freezing}$ [110], was suggested by Authelin et al. [102] as a in pharmaceutical freezing processes. It assumes a step decrease of the cooling fluid temperature $T_{cooling}$ from equilibrium to set temperature and the bulk to be at melting temperature T_m prior to freezing. The equation can be written as

$$t_{Plank} = \frac{\rho_l \, \Delta H_m \, X}{E \, k_a \, (T_m - T_{cooling})} \left(1 + \frac{Bi}{2} \right), \qquad\qquad \text{3-I}$$

where ρ_l is the density of the liquid sample, ΔH_m is the latent heat of fusion and X is the characteristic distance between the LPTF and the heat transfer surface [111]. The geometric factor E is 1 for infinite slabs, 2 for infinite cylinders and 3 for spheres. The Biot number $Bi = k_a X / \lambda_s$ relates the heat transfer resistance of the shell k_a to internal heat conductivity resistance of the sample with a given heat conductivity λ_s [112]. For pharmaceutical solutions, the physical properties of solid water as the solvent can be used under the assumption of diluted solutions [113][114]. Assuming a negligible temperature difference between the equilibrium and melting temperature and the

wall temperature equals T_∞ ($Bi \to \infty$), which may be done for actively cooled freezing systems, the freezing time may be calculated using equation 9-II,

$$t_{freezing} = \frac{\rho_l \, \Delta h_m \, X^2}{2 \, E \, \lambda_s \, (T_m - T_{cooling})} = \frac{\beta}{-T_{cooling}} \qquad \text{3-II}$$

where β in °C·min is a function of ρ_l, Δh_m, X^2, λ_s, and E, summarizing all constant values for a given active freezing system.

3.2.5. Frozen bulk analytic

A hollow drill from Buerkle (Bad Bellingen, Germany) with an inner diameter of 8 mm has been used to take samples from the frozen bulk. A 3D-printed mount with 9 drill holes in two different rows at an angle of 10.5 ° was placed on top of a chamber, providing reproducible drill positions across the whole chamber length. Under the assumption of negligible radial boundary effects, sampling from two different rows with overlapping sample volumes increased the sample resolution of a cross section as depicted in Figure 3.1 in solid and dashed lines. Samples were taken from the drill holes at 3 levels of 8 mm height with the last hole 2 mm above the chamber bottom. The sample above the first sample level has been discarded at all times to avoid uptake of ice fragments from the previous drilling and measuring of the freeze concentrated liquid from the center of the chamber that was pushed out where the expanding ice fronts met. The samples were transferred into 2 mL reaction tubes from Eppendorf (Hamburg, Germany) and thawed at room temperature. The buffer concentration of the samples was measured by analysis of the conductivity using a conductivity meter CDM 230 from Radiometer Analytical SAS (Lyon, France).

3.3. Results

3.3.1. Freezing time analysis

In order to characterize and describe a freezing process, the total freezing time is a key process parameter. Total freezing times could be calculated from the second derivative as shown in Figure 3.2. While minima at the total freezing time are prominent, minima at the partial freezing time are not. With elevated freezing temperatures above -25 °C, the first minima were not detected correctly at all temperature probes due to low signal to noise ratios of the temperature sensors. Therefore, the partial freezing times were determined when the temperature fell below -2 °C. With the freezing times at the individual probes, ice front progression in the chamber could be monitored as presented in Figure 3.3. Total freezing times calculated from the second derivative of all temperature profiles resulted in standard deviations below 2 % for pure water samples and below 4 % for highly concentrated buffer samples. Looking at observed process temperatures shown in Figure 3.2A, the

cooling temperature exceeded the set temperature by up to 3 K due to temperature regulation, whereas the fluid temperature did not, due to heat capacity of the steel housing.
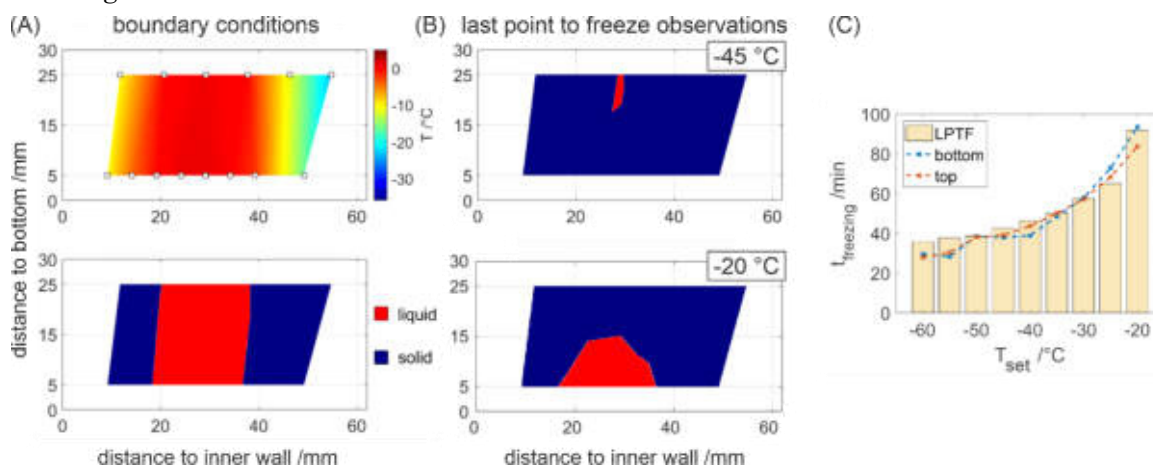
Figure 3.3: 2D resolved temperature analysis of the chamber cross-section. **A** displays interpolated temperature data, where temperature probes are indicated by rectangles. In the lower figure, temperatures below -1 °C and above are highlighted by blue and red, respectively. **B** shows highlighted temperatures prior to the LPTF for -45 °C and -15 °C. **C** compares the individual freezing times at the bottom and top temperature sensor at different set temperatures. LPTF times determined by the temperature slope are plotted as bar plots for reference.

3.3.2. Process characterization

Purified water was frozen at different temperatures to characterize the novel freeze-thaw device with respect to heat transfer properties because of the availability for large scale process characterization. In our studies, the total freezing time of water samples shortened by 2.3-fold from 78.7 to 33.8 min when decreasing the set temperature from -20 to -60 °C as shown in Figure 3.4.

Freezing times shortened faster at higher cooling temperatures compared to an almost stagnant freezing time reduction at lower cooling temperatures. Based on equation 9-II, an estimation model has been fitted using data from -25 to -20 °C, which resulted in a ß-value of 1619 °C·min with $R^2 = 0.972$. Solving equation 9-II with the data at -20 °C results in ß = 1620 °C·min. A RMSE of 1.83 min for the model and all set temperatures was calculated, where the measured freezing times at temperatures below -25 °C always exceeded the estimated freezing time. A ratio of cooldown time
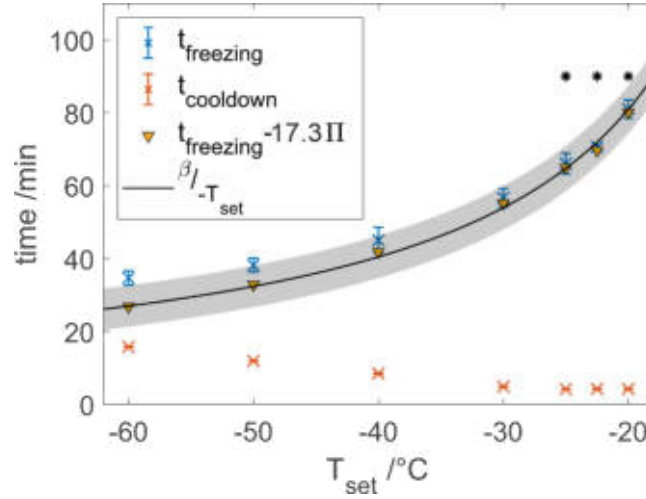
Figure 3.4: Freezing and cooldown times at different set temperatures. Data marked points with a star were used to calibrate a model after 9-II with ß = 1619, where the grey area shows the 95 % confidence bounds.

and total freezing time Π was calculated after equation 9-III. Subtraction of empirically determined 17.3-fold Π from the total freezing times reduced the RMSE to 0.96 min, where especially the estimation of freezing times at lower temperatures was improved as indicated in Figure 3.4.

$$\Pi = \frac{t_{cooldown}}{t_{freezing}} \qquad\qquad 3\text{-III}$$

Analyzing the temperature of the heat transfer fluid inside the cooling unit, cooldown times of 4.2 to 4.9 min for set temperatures of -30 °C and above were measured. Cooldown times greatly increased for lower set temperatures. The temperature differences between cooling fluid and the cryo-device outlet were up to 3 K after freezing process start and reduced to around 0.5 K at equilibrium state. Using a mean heat capacity of 1.5 kJ/kg/K and a density of 900 kg/m³ of the heat transfer fluid provided by the supplier and a flow rate of 25 L/min, a power loss of 330 to 100 W can be estimated at equilibrium state.

3.3.3. Sample temperatures

With the help of temperature fibers, a continuous two-dimensional resolved temperature field could be observed as shown in Figure 3.3. Assuming frozen sample for temperatures below -2 °C, the ice front progression was observed during a freezing process. When freezing 500 mM Tris buffer solution, perpendicular freezing fronts have been observed as shown in Figure 3.3A. The LPTF was observed at a distance of 26.5 ± 2.5 mm from the inner cooling wall at all experiments. In contrast, the vertical position of the LPTF varied with temperature as shown in Figure 3.3B. In experiments

with set temperatures below -25 °C, the freezing fronts met at the bottom of the container first and a small gap froze from the bottom to the top of the container, resulting in a LPTF position at the top of the chamber. This occurs as liquid is pushed to the bulk surface by the expansion of water molecules, which agrees with an observed iceberg on top of the sample bulk at the location of the LPTF. Freezing at elevated set temperatures of -25 °C and above resulted in a LPTF position at the bottom of the container, where the remaining liquid froze in the form of a shrinking bell. Figure 3.3C shows total freezing times at the top and the bottom of the container based on temperature compared to the total freezing times calculated from temperature slopes. The slope based freezing times were similar to those observed for purified water shown in Figure 3.2. Differences in freezing times at the top and bottom of the freezing container were marginal for set temperatures below -25 °C when compared to differences of up to 9.7 min at higher set temperatures.

3.3.4. Frozen bulk analysis

A 500 mM Tris buffer solution at pH 7.5 has been frozen at -20, -40 and -60 °C to evaluate the influence of the freezing temperature on cryo-concentration and the results are shown in Figure 3.5. The maximum freeze concentrated area was located at the LPTF position 25 mm away from the inner cooling wall at all freezing experiments. When increasing the temperature from -60 to -40 to -20 °C, the maximum freeze concentration increase (c_{max}/c_0) rose from 1.39 ± 0.01 to 1.52 ± 0.03 to 2.53 ± 0.04, respectively. The bulk inhomogeneity, more specifically the ratio of the maximum to the minimal concentration (c_{max}/c_{min}), summarizes freeze concentration results and high values represent high freeze concentration. The bulk inhomogeneity improved significantly when lower the freezing temperature from 8.1-fold to 3.6-fold to 3.0-fold at freezing temperatures of -20 °C, -40 °C and -60 °C, respectively. In general, it was observed that a concentration gradient from top to bottom was present. The authors want to mention, that the sampling method only provided averaged concentrations of the sample volume, whereas the true local peak freeze concentration is expected to be higher.

3.4. Discussion

3.4.1. Freezing time analysis

We demonstrated a method to extract freezing times at individual positions of temperature probes and the total freezing time from the second derivative of various temperature profile. A common problem in the detection of freezing at individual probes is freezing-point depression which leads to assumptions such as solid state below -5 °C [17]. Furthermore, detection of the total freezing time based on raw temperature profile relies on the knowledge of the LPTF position. We overcome both of these issues with the approach to use the second derivative of the temperature. However, the method relies on precise and high frequency data with high differences in freezing and equilibrium temperature. With higher freezing temperatures, signal to noise ratios decreased due to lower absolute temperature gradients. Thus, standard deviations of freezing times increase with higher freezing temperatures. As a result, only LPTF freezing times were calculated by slope analysis. Individual freezing times
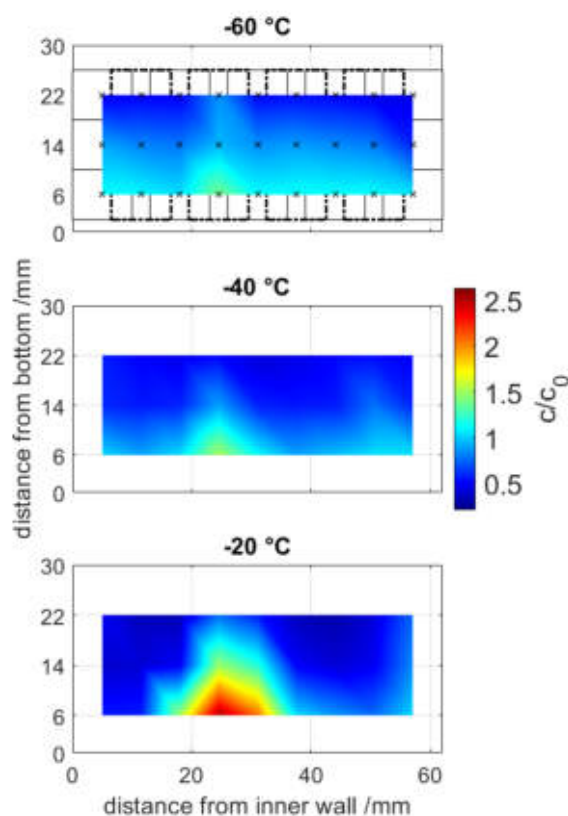
Figure 3.5: Offline sample analysis from frozen drill cores at temperatures from -60 to -20 °C. Samples volumes are visualized in the first graph in solid and dashed rectangles, where the center of a measurement is marked by x. Normalized concentration are visualized by a color gradient from blue to red and are interpolated between the averages from triplicates.

used to calculate freezing times at the top and bottom of the container were assumed for temperatures below -2 °C. Comparing the two methods as shown in Figure 3.3C reveals deviations of the two methods. While derivative-based analysis shows similar trends seen for purified water, temperature-based analysis often leads to larger deviations from expected freezing times. Nonetheless, temperature-based analysis was able to indicate settling of the LPTF to the ground of the chamber as discussed in the following sections. This can be important when designing freezing processes with a single thermoelement, as this should be directed at the LPTF. Unfortunately, the fiber optic temperature sensors provided a generally lower signal to noise ratio when compared with common thermo elements. This, however, shows the applicability and robustness of the derivative based method.

3.4.2. Extensions of the Plank equation

As shown above, a decrease of the freezing temperature shortens total freezing times. The non-linear trend can be explained partially by thermodynamic properties of freezing processes as we showed by our model based on Plank's model. The calculated model based on three initial freezing tests with water was able to estimate total freezing times at lower temperatures.

With lower freezing temperatures, however, larger deviations of our experimental results from the Plank model were observed. These deviations show the process related limitations of the Plank equation. Unlike our model, the measured values are expected to approach a minimal freezing time of approximately 31 min for lower freezing temperatures, based on exponential extrapolation of all measured data. The rising cooldown times for decreasing temperatures could explain the limited behavior of the real freezing time since the Plank equation is only applicable to step-like cooling temperatures. Therefore, a dimensionless number Π was introduced to take the transient starting conditions of a freezing device into account. For an ideal system, with a step like cooling temperature decrease, Π approaches 0, whereas in real systems, Π is expected to increase with decreasing freezing temperatures due to physical heat transfer restrictions in cooling units. If it exceeds 1, lowering the set cooling temperature will not result in a further decrease of cooldown times as the initial transient period exceeds the freezing time. Hence, cryo-concentration of solutes will not decrease either. Π values with our setup are summarized in Table 3.1.

Table 3.1: dimensional Π values of the freezing device

set temperature	Π /-
-60.0 °C	0.466 ± 0.0041
-50.0 °C	0.318 ± 0.0016
-40.0 °C	0.192 ± 0.0044
-30.0 °C	0.088 ± 0.0006
-25.0 °C	0.064 ± 0.0002
-22.5 °C	0.060 ± 0.0010
-20.0 °C	0.054 ± 0.0008

Π rises with increasing cooldown times at lower set temperatures as more enthalpy needs to be removed from the cooling fluid and as cooling units become less efficient at lower temperatures. Empirical correction of freezing times by the calculated Π values significantly improved the model. We therefore conclude that the Plank equation may be used to predict freezing times even at low temperatures when transient start-up conditions are considered. Furthermore, Π should be especially important when scaling experiments are performed or different freeze-thaw processes are compared. In general, Π is thought to be the highest for small freezing distance containers such as freeze bags, due to short total freezing times. On the other end, passively cooled systems, such as freeze-thaw bottles, will have lowest Π due to their step-like cooling temperature decreasing and long freezing times. The authors therefore conclude, that from a cryo-concentration point of view, freezing temperature is highly important for system with longer freezing times e.g. passively cooled systems and cooled vessels, which was also shown by Nidhi et al. [71]. Contrarily, lowering the set temperature in fast freezing processes might only marginally improve bulk homogeneity and protein integrity as reported for freeze-thaw processes in single-use bags [13], [76], [115], with shorter freezing times where transient starting conditions can play a significant role. As an application example, the Plank model may be used for justification of a proven acceptable range in front of regulatory authorities, where lower freezing temperatures result in a wider acceptable range and thus a more robust process.

3.4.3. Sample temperature

The parallel, perpendicular freezing fronts during the freezing observed in our setup provide valuable information on the scalability of our process. It highlights the

minimized boundary effects present in our setup, which is essential for small-scale models. In small-scale processes with uncontrolled boundary effects such as passive freezing in bottles, freezing from the bottom occurs, which may impact the freezing front shape and the final concentration profile as seen by Kolhe et al. [15], where the bottom concentration was usually lower than the layer above. In studies using actively cooled systems, boundary effects are not yet described.

Another phenomenon observed was, that the distance of the LPTF was closer to the inner cooling wall, which is a result of the smaller heat transfer area at the inner wall. A simplified energy balance between the volume from the inner cooling wall to the LPTF and the outer cooling wall and the LPTF (see supplementary material) leads to a theoretical LPTF distance to the inner wall of 24 mm, which agrees with our findings.

Apparent descending of the LPTF to the bottom of a chamber when freezing at elevated temperatures can be explained by settlement of the freeze concentrated liquid throughout the process [7], [15]. Concentrated solution pushed to the top at the LPTF agrees with results of Hauptmann et al. [14]. Freeze concentration leads to viscosity and density gradients in the solution inducing natural convection [64]. Furthermore, freezing-point depression occurs with increased concentration. Thus, the LPTF position will sink to the bottom, when freeze concentration is superior at elevated freezing temperatures. This effect is likely to be more pronounced in large scale applications, due to an increased convection [102] and larger sedimentation distances. A temperature probe is placed commonly at the LPTF for process monitoring [17], [76], which might result in false results when different formulations are frozen. We therefore suggest the derivative based method discussed above for process characterization based on freezing time because of the method's flexibility with regards to position of temperature probes in the container.

3.4.4. Frozen Bulk analysis

In general, our findings with concentration maxima of up to 2.5-fold are in agreement with literature with actively cooled freezing devices [16], [19], [104], who reported 1.3 to 2.5-fold freeze concentrations. The concentration gradient observed can be explained by the freeze-concentration due to solute exclusion [102], [106] and the previously mentioned settlement of denser freeze concentrate [15]. The smaller reduction in bulk homogeneity when decreasing the temperature by 20 °C at lower freezing temperatures can be attributed to smaller reduction in freezing time at lower temperatures due to physical limitations as seen by Plank's model. This supports our findings, that freeze concentration and therefore freezing processes can be characterized by freezing time, which is in agreement with Hauptmann et al. [14].

3.5. Conclusion

The presented results give industrially relevant guidance for freeze-thaw process design and monitoring. A novel freeze-thaw device using two individual cooling circuits is demonstrated. While the model has an increased engineering complexity, it is capable of reducing boundary effects such as freezing from the bottom. Thus, process parameters, such as temperature dependent settlement of the LPTF, can be evaluated at a small-scale, which is important for process monitoring. Furthermore, a high-resolution temperature monitoring approach with process interference was combined with a derivative-based method to calculate total freezing times. The determined freezing time had a high impact on the resulting freeze concentration profile of the frozen bulk. These freezing times can be estimated for a given actively cooled system using the Plank equation by model calibration with few freezing time experiments. However, for real processes at low freezing temperatures, the Plank model has to be extended by the non-dimensional number Π to consider start-up conditions present during cooldown of the heat transfer fluid and the system. Π might explain, why freezing temperature plays a more important role in short distance freezing processes. Thus, the reduction of freezing temperatures might have a bigger impact on frozen bulk homogeneity for freezing processes with larger characteristic distances as seen in stainless steel vessel. Processes with shorter freezing distances such as freeze bags might not be as improved by low freezing temperatures. These findings thus have a high impact on future process analytical technology strategies for freeze-thaw operations in the pharmaceutical industry.

3.6. Acknowledgements

3.7. Supplementary material

3.7.1. LPTF calculation

An energy balance is used to calculate the theoretical LPTF distance to the inner wall $d_{\text{LPTF, in}}$. Therefore, the sample volume is divided at the LPTF into an inner V_{in} and outer V_{out} volume with an equal freezing time t_{freezing}.

$$t_{freezing,in} = t_{freezing,out}$$

3-IV

The heat flow $\dot{Q}$ into the sample can be calculated from the heat transfer coefficient k, the heat conducting surface A_{Wall} and the temperature difference between the sample and the cooling fluid ΔT_∞ as described by equation 3-V.

$$\dot{Q} = k\, A_{wall}\, \Delta T_\infty$$

3-V

The total enthalpy H that is removed within $t_{freezing}$ is calculated by equation 3-VI,

$$\dot{Q}\, t_{freezing} = H = V\left(c_{p,ice}\, \Delta T_{sample,mean} + \rho_l\, \Delta h_m\right)$$

3-VI

where V is a sub volume, $\Delta T_{sample,mean}$ is the mean temperature difference between the mean sample temperature at equilibration and at $t_{freezing}$, ρ_l is the liquid sample density, Δh_m is the specific latent heat. Equation 3-VII can be calculated by solving 3-IV with 3-V and 3-VI and calculating the specific areas and volumes with the inner r_{in} and outer r_{out} radii of the freezing device.

$$\frac{V_{in,LPTF}}{A_{in}} = \frac{V_{out,LPTF}}{A_{out}}$$

5-V & 5-VI
in 5 IV

$$r_{LPTF} = \sqrt{r_{in}\, r_{out}} \;\; with \;\; d_{LPTF} = r_{LPTF} - r_{in}$$

3-VII

ΔT_{sample} was assumed to be linear.

4

Raman spectroscopy as a process analytical technology to investigate biopharmaceutical freeze concentration processes

Dennis Weber[1], Jürgen Hubbuch[1]*

[1] Institute of Engineering in Life Sciences, Section IV: Biomolecular Separation Engineering, Karlsruhe Institute of Technology (KIT), Karlsruhe, Germany

*Corresponding Author

Abstract

Freezing processes are a well-established unit operation in the biopharmaceutical industry to increase the shelf-life of protein-based drugs. While freezing reduces degradation reaction rates, it may also exert stresses such as freeze concentration. Macroscopic freeze concentration in large scale freezing processes has been described thoroughly by examination of frozen bulk material, but the transient process leading to such freeze concentration profiles has not been monitored yet for biopharmaceutical solutions. In this study, Raman spectroscopy as a process analytical technology is demonstrated for model formulations containing monoclonal antibodies (mAb) or bovine serum albumin (BSA) in varying concentrations of sucrose and buffer salts. Therefore, a Raman probe was immersed into a bulk volume at different heights, monitoring the freeze concentration in the liquid phase during freezing processes. Partial least square (PLS) regression models were used to distinguish between the protein and excipients. The freeze concentration profiles showed temperature and formulation dependencies with freeze concentrations up to 2.4-fold. Convection currents at the bottom of the freezing container were observed with a maximum height of 1 mm. Furthermore, freeze concentration was correlated with the sucrose

concentration in a formulation. Analysis of the freeze concentration slope indicated diffusion from the bottom to the top of the container. As a conclusion, Raman spectroscopy is a valuable tool for process validation of freeze concentration simulations and to overcome scale dependent challenges.

Keywords: freeze concentration, Raman spectroscopy, formulation, monoclonal antibody

4.1. Introduction

Pharmaceutical proteins are among the top-selling drugs with monoclonal antibodies (mAb) as the most successful product [38]. The ever-growing demand for mAbs leads to the desire and need for new and larger scale manufacturing processes [116] from which new challenges arise. As the last step, the final fill, in the production of biopharmaceutical drugs is often located off the production site, large bulk volumes of formulated drug need transportation. To improve the shelf-life and reduce shear stress during transport, bulk substances may be frozen before transportation [7]. While freezing slows down drug degradation reactions, it may also induce protein activity loss due to protein-ice surface interactions, cold denaturation and freeze concentration gradients [27], [28]. Therefore, drug formulations often contain excipients such as carbohydrates for protein stabilization in a glassy matrix [117] to reduce freeze denaturation of proteins. During a freezing process, freeze concentration occurs, excluding solute molecules from the crystallizing water. On a microscale, solutes are entrapped within ice crystals and the amount of water is constantly reduced with decreasing temperatures until either a glass is formed or solutes start to crystallize. On a macroscopic scale in large scale freezing, a freezing begins at the cooling walls and progresses to the center of the container. A transition or mushy zone forms, where ice crystals grow into solution. At this mushy freezing front, solutes are partially excluded and entrapped within the ice matrix. The solute concentration in the solid phase c_{solid} is reduced compared to the concentration c in the liquid phase at the freezing front as described by the partition coefficient k in equation 4-I [61].

$$k = \frac{c_{solid}}{c} \qquad\qquad \text{4-I}$$

As a result, solute concentration and temperature gradients are found in the remaining liquid phase leading to density gradients during the freezing process. Hence, buoyancy-driven natural convection occurs in large scale freezing processes. When observing the liquid concentration c at a fixed point, the relative freeze concentration c/c_0, where c_0 is the initial bulk concentration, will increase over time. With increasing freezing volumes, freeze concentration profiles may change as convection becomes more dominant [102], which poses scalability challenges. Natural

convection is well described for traditional solidification processes such as alloy solidification [68], [69], [100]. However, the complex solidification of multi-component solutions frozen in pharmaceutical applications currently lacks of process understanding necessary to overcome scalability issues. In the past, studies have been performed on novel freeze-thaw devices [106], [118]–[120] with the aim of improved scalability and processes were mostly characterized by solute concentration in the frozen bulk [15], [71], [104], [121]. However, in large scale freezing processes, freeze concentration profiles are a result of the interplay of diffusive and convective mass fluxes. The analysis of the frozen bulk concentration lacks of information to describe transient mass fluxes in freezing processes. First, the measured concentrations are averaged across the sample volume providing a limited spatial resolution. Second, frozen samples represent the final state with limited information on the transient freezing process. Recently, computational fluid dynamic modelling has been proposed as a tool for freeze concentration prediction [119], [122]. While the prediction of temperature has been validated by real-time process data, the freeze concentration profiles were only validated by the solute concentration in the frozen bulk at the end of the process. On-line data of freeze concentration enables validation of simulated findings with regards to concentrations and thus improves model reliability of simulated scale-up models. The transient process of freeze concentration was investigated previously on a microscopic scale by Raman spectroscopy [123] and by Mach-Zender optical interferometry [64]. Furthermore, Raman spectroscopy was also suggested as a tool for on-line process monitoring of pharmaceutics [88]. An on-line monitoring of the transient, macroscopic freeze concentration is yet missing. Hence, in the following study, Raman spectroscopy was used for on-line monitoring of macroscopic freeze concentration for the first time. Raman spectroscopy with partial least squares (PLS) regression is used for monitoring of individual formulation solutes. The transient, solute dependent freeze concentration effects were analyzed in a large-scale freezing process. The study provides an in-depth process understanding of diffusive and convective mass fluxes present in freezing processes.

4.2. Materials and Methods

4.2.1. Sample Preparation

All used solutions were prepared with ultrapure water (PURELAB Ultra, ELGA LabWater, Veolia Water Technologies, Saint-Maurice, France) and filtered using 0.2 µm filter prior to application. Tris buffer was prepared from Tris-(hydroxymethyl)-aminomethane purchased from Merck (Darmstadt, Germany) and Tris-(hydroxymethyl)-aminomethan-hydrochlorid purchased from Applichem (Darmstadt, Germany) at concentrations ranging from 50 to 1500 mM. The pH was adjusted to

pH 7.5 ± 0.1 using hydrochloric acid. Sucrose was used as an exemplary cryoprotectant with low tendency for crystallization [117]. Therefore, sucrose with 99 % purity was purchased from former Alfa Aesar now Thermo Fisher (Kandel, Germany) and dissolved at concentrations ranging from 250 to 2000 mM. All solutions were prepared from stock solutions. As a model protein, lyophilized BSA with a purity exceeding 98 % was purchased from Merck (Darmstadt, Germany). It was dissolved in the desired buffer solution at high concentrations using a SpeedMixer DAC 150 from Hauschild (Hamm, Germany) and diluted to the desired concentration. As a typical pharmaceutical protein, a mAb was kindly provided by Byondis (Nijmegen, The Netherlands). The frozen cell culture supernatant was thawed and the mAb captured using protein A chromatography. The protein A eluate was dialyzed against the buffer of interest using 10 kDa Snakeskin Dialysis Tubing from Thermo Fisher Scientific (Massachusetts, USA) for 1 h at room temperature and then over night at 5 °C after buffer exchange. The protein concentration was adjusted using Vivaspin 2 with a 30 kDa cut-off PES membranes from Sartorius (Göttingen, Germany) and dilution with buffer.

4.2.2. Experimental freezing setup

Bulk freezing was performed in an actively cooled freezing device depicted in Figure 4.1. The device is cooled by two individual cooling units, one to apply the set freezing temperature and a second one to cool the bottom of the device to minimize boundary effects such as freezing from the bottom. The device is split into six individual chambers to reduce the sample volume by an inlay made from polytetrafluoroethylene (PTFE). Additionally, the inlay insulates the bottom of a freezing chamber which reduces boundary effects further. An in-depth device and process characterization has been described previously [120]. For each experiment, the freezing chamber was filled with 90 mL of process solution. If the samples were re-used, the bulk was homogenized by aspirating and dispensing using a 5 mL pipette. Prior to a freezing process, the temperature was equilibrated for at least 2 h at 5 °C, followed by the initiation of the freezing process at temperatures between -60 °C and -20 °C at maximum cooling rate. After the freezing step, thawing was initiated by a temperature increase to 30 °C for mAb and to 40 °C for BSA over at least 45 min. The individual steps were timed using predefined methods, which were executed by an in-house software written with Matlab 2020b (The Mathworks, Natick, MA, United States). The Raman probe and the sample capillary were positioned at a distance of r = 32 mm from the inner cooling wall using 3D-printed mounts, to assure reproducibility and precise positioning. The

depth of the Raman probe was varied from 1 to 15 mm above the bottom of the freezing chamber. Exact dimensions are noted in Figure 4.1.
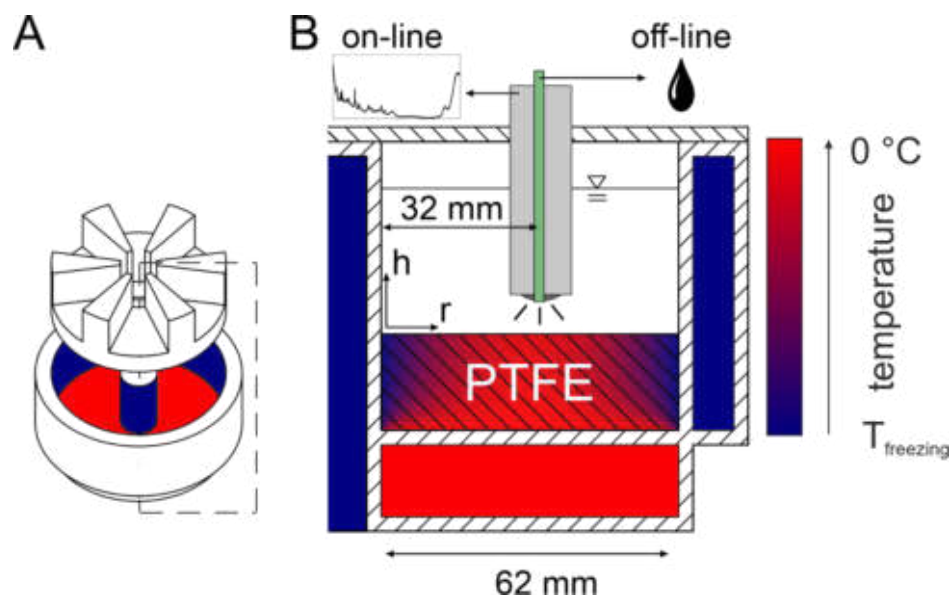
Figure 4.1: A An exploded view of the freeze-thaw scale-down model with the insulating inlay. The bottom temperature is controlled separately to reduce boundary effects. The freezing chamber is separated by an inlay into six chambers. A cross section through one chamber as highlighted by the dashed box is shown in **B**. The Raman probe and capillary for sampling are depicted in grey and green, respectively. Images were adapted from Weber et al. [120].

4.2.3. Raman spectroscopy

A HyperFlux PRO PLUS 785 from Tornado Spectral Systems (Toronto, ON, USA) with a bandpass from 200 - 3300 cm^{-1} from 785 nm wavelength laser at a power of 495 mW together with Fiber BallProbe® from Marqmetrix (Seattle, WA, USA) was used to obtain Raman resonance spectra. The focal length of the optics was 200 µm. The spectral resolution was 1 cm^{-1} and integration times from 700 to 1400 ms were chosen depending on the exposure time suggested by the autoexposure option of the software SpectralSoft by Tornado Spectral Systems (Toronto, ON, USA). Spectra were recorded every 5 s. The laser probe was positioned at a constant distance from the inner cooling wall, whereas the height above the chamber bottom was varied from 1 to 15 mm as described above.

4.2.4. Partial Least Squares model calibration for on-line concentration

PLS models were calibrated from batch experiments spectra exclusively. A set of 55 solutions with varying concentrations of Tris (0 – 1000 mM), sucrose (0 – 710 mM), mAb (0 – 25 g/L) and BSA (0 – 56 g/L) were prepared from stock solutions. Calibration

spectra were recorded as described above but at room temperature. For each solution, the probe height and exposure time were varied to account for possible changes in spectra background and the spectra were recorded at least 5 times. The recorded spectra were processed using MATLAB R2020b by Mathworks (Natick, MA, USA). At least 125 of the total 775 spectra were selected for cross-validation based on equal solute concentration distribution across the measured concentrations. For preprocessing, the spectra were normalized by the exposure time, smoothed and optionally derived using a Savitzky-Golay filter with a second-order polynomial fit [124]. Wavenumbers below 700 and above 3050 cm^{-1} were excluded. A background subtraction using a water or buffer spectrum was evaluated for basic subtraction and extended multiplicative signal correction (emsc), but did not improve model accuracy and robustness. For each solute, the calibrated PLS models were used to calculate concentrations from the spectra as described by Großhans et al. [125]. Briefly, a Matlab built-in genetic algorithm was used to optimize the PLS model based on calculated predictive residual sum of squares (PRESS) with varying options such as number of latent variables (3 - 10), Savitzky-Golay smoothing filter window width (5 - 35) and optional spectrum differentiation. Division of the PRESS by the total number of samples was used for calculation of the root mean square error cross validation (RMSECV). Q^2 and R^2 were calculated as suggested by Wold et al. [126]. For modelling of the mAb concentration, spectra from BSA were excluded and vice versa. Furthermore, high concentrations of BSA lead to major changes in the Raman resonance. Thus, modelling of the Tris concentration was performed separately for samples without and with BSA, where the later only used information from 2700 - 3050 cm^{-1}.

4.2.5. Off-line sample analysis

In order to validate the PLS predicted concentrations, offline samples of 300 µL were taken at the same radius and height as the Raman probe using a peek capillary with an inner diameter of 0.17 mm and 1 mL syringes. The protein concentration of the samples was measured by UV-absorption at 280 nm using a Nanodrop 2000c by Thermo Fisher Scientific (Massachusetts, USA). Extinction coefficients of 0.67 g/(L cm) for BSA and 1.5 g/(L cm) for mAb have been used. In order to determine sucrose and Tris concentrations, the conductivity and density of samples were measured using a conductivity meter CDM 230 from Radiometer Analytical SAS (Lyon, France) and micro liquid density sensor from Integrated Sensing Systems, Inc (Ypsilanti, US). As both solutes affect both density and conductivity, a two-dimensional regression calibration was performed with 32 samples ranging from 0 to 300 mM Tris and 0 to 1200 mM sucrose. The calibration results were approximated

by second order polynomial regression resulting in an R^2 of 0.999 for the conductivity and 0.999 for the density. Detailed calibration information is listed in the supplementary material.

4.3. Results and Discussion

4.3.1. Liquid freeze concentration monitoring with Raman spectroscopy

The freezing process of pharmaceutical formulations was evaluated using Raman resonance spectroscopy. Spectral changes over the course of a freezing process may occur due to for example temperature deviation presented and discussed in the following. The Raman spectrum of a purified water sample measured in the freezing chamber at room temperature contained peaks at 1637 and 3235 cm^{-1} attributed to water and peaks at 732, 1215, 1300, and 1380 that occur due to the PTFE [127] bottom of the freezing chamber. The transition from water to ice can be observed in the spectra at 3140 cm^{-1}, where a distinct ice peak arises, while the water peak at 3235 cm^{-1} declines as the solution freezes as shown in Figure 4.2B. The ice peak was described and compared already in the early 1930s by Ockman [128] and the transition during solidification was recently used to describe phase transition from water to ice [129]. Additionally, baseline shifts were present throughout all measurements, which are comparable to Raman spectra of biological samples [130] in the fingerprint region from 700 to 1900 cm^{-1} and due to the broad water resonance peak from 2600 to 3330 cm^{-1}. The addition of solutes leads to numerous peaks in the fingerprint region and from 2600 to 3050 cm^{-1}, as well as baseline shift changes in the fingerprint region. The spectra observed at 5 mm above the bottom for a model formulation with 50 mM Tris and 200 mM sucrose frozen at -20 °C is depicted in Figure 4.2.

As shown in Figure 4.2A, the spectra remain stable until around 30 min when freezing at -20 °C. After 30 min, most of the peaks in the fingerprint region began to increase due to freeze concentration. Water peaks, however, remained constant until solidification began. When the freezing front reached the Raman probe, ice crystals are formed leading to a significant decrease of the mean Raman resonance as shown in Figure 4.2C. The decrease of the mean spectrum can be attributed to changes in optical density due to crystallization. Thus, the rapid decrease in the mean spectra was used to detect the beginning of the phase change. Đuričković et al. [129] suggested to use a ratio S_D of water and ice peak areas to describe the phase transition. Similarly, S_D was calculated after Equation 4-II by summing up of the raw Raman intensities I for the water peak area from 3270 - 3290 cm^{-1} and the ice area from 3140 - 3160 cm^{-1}.

$$S_D = \frac{\sum_{3270}^{3290} I}{\sum_{3140}^{3160} I} \qquad\qquad \text{4-II}$$

When comparing the mean Raman resonance and S_D, as shown in Figure 4.2C, both signals decreased upon arrival of the freezing front at the Raman probe after 44 min. The mean Raman signal decreased rapidly and stabilized after 60 min total, whereas S_D decreased later and continuously decreases over the observed time. This indicates, that the majority of solidification has taken place after 16 min and optical properties reached an equilibrium. Meanwhile, the water crystals are continuously formed and the ice structure changes as seen in S_D, while the solution is approaching phase equilibrium given for the current temperature. Ideally, the method would be able to
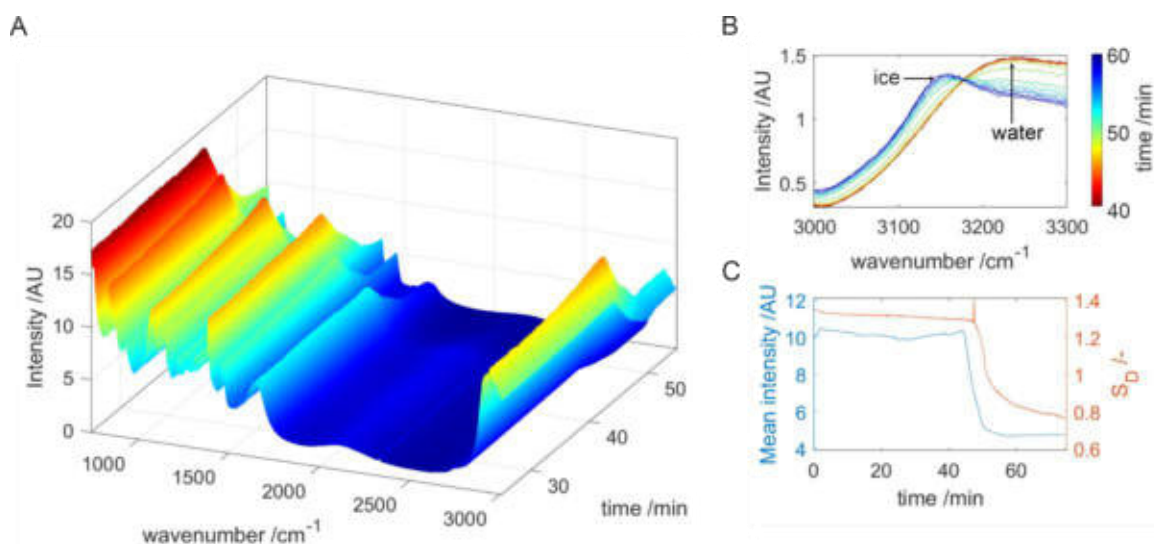
Figure 4.2: A Example Raman spectra over time when freezing a 50 mM Tris, 200 mM sucrose solution at -20°C. Probe height was 5 mm. **B** Raman spectra shift from water to ice used for calculation of S_D. **C** Comparison of the mean spectrum and the water to ice peak areas S_D over time.

predict the solute concentration in the frozen state. However, PLS modelling of freeze concentrated solution would require frozen solutes with known concentration for model calibration. Due to micro scale freeze concentration within the crystalline ice structure, this was not possible with the used set-up. Twomey et al. overcame this issue by implementation of confocal Raman spectroscopy [29]. In this study, the application of PLS models derived from liquid samples on frozen state, however, resulted in large differences for Tris and sucrose as shown below in chapter 4.3.3 Validation of Raman concentration monitoring and predicted concentrations post freezing were not reproducible. The Raman probe and laser introduce heat in the system, influencing the ice structure and glass composition. Thus, the predictions of concentration are only valid in the liquid state and the freeze concentration data post freezing is not shown in the following for visualization purposes.

4.3.2. PLS modeling of Raman spectra for concentration quantification

PLS models were used to quantify and distinguish up to three individual formulation agents. PLS regression coefficient of each solute are shown in Figure 4.3 and the PLS modeling characteristics are summarized in Table 4.1.
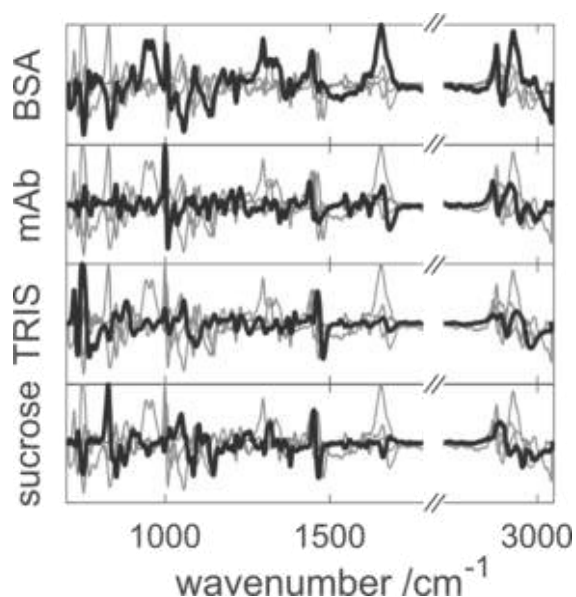
Figure 4.3: Normalized PLS regression coefficients for the prediction of solute concentration. The regression coefficients of the solute are highlighted as a bold line, while the remaining coefficients are supplemented in gray. BSA spectra are non-derived. mAb, Tris and sucrose coefficients are applied to the first derivative of a spectrum.

Table 4.1: Summary of the Raman spectrum preprocessing parameters, the PLS model parameters and the quality of prediction for each solute. Two Tris models were used for prediction in presence and without BSA.

	mAb	sucrose	Tris	BSA	Tris (with BSA)
Latent variables	8	7	5	9	3
Savitzky-Golay window	11	29	19	15	5
derivative	1	1	1	0	1
Wavenumbers /cm^{-1}	700 – 3050	700 – 3050	700 – 3050	700 – 3050	2700 – 3050
R^2	0.998	0.997	0.999	0.999	0.939
Q^2	0.999	0.999	1.000	1.000	0.999
RMSECV	0.07 g/L	1.08 mM	0.72 mM	0.08 g/L	2.56 mM
Calibration range	1.7 – 25 g/L	80 – 708 mM	31 – 1000 mM	14 – 56 g/L	31 – 1000 mM

For all solutes except BSA, the first derivative of the spectra led to the best modelling results. While one PLS model for sucrose quantification could be used for all samples, a separate model for Tris quantification was used for samples containing BSA, where only the wavenumbers from 2700 to 3050 cm^{-1} were used. In general, three to nine latent variables have been used with a Savitzky-Golay filter window between five and nineteen wavenumbers. Other studies used five to seven latent variables [131], [132] for the prediction of protein concentrations with Raman spectroscopy. The calculated coefficients of determination R^2 ranged from 0.997 to 0.999 with similar Q^2-values. The models provided good linear correlation across all the calibration concentrations. Despite the promising quality attributes of the models, the model data was generated solely from batch measurements at room temperature. Temperature changes and convection in the freezing process might cause background variations and noise reducing model accuracy. Therefore, validation of the predictions in freezing processes was performed to evaluate deviations from batch measurements as discussed later. Spectral preprocessing to minimize the influence of process conditions on the model was evaluated by extended multiplicative signal correction and subtraction of a water spectrum as a background. However, this intense preprocessing did not improve the model by means of R^2 and predicted high noise levels when applied on freeze process data. Furthermore, spectrum normalization, while giving the opportunity of

overcoming challenges in optical property shift, also led to worse R^2-values and high signal to noise ratios in the predicted concentrations in the process.

4.3.3. Validation of Raman concentration monitoring

In order to validate PLS predicted freeze concentration, the predicted concentrations were compared against concentrations in liquid samples, that were aspirated at a 5 min interval using a capillary. The Raman probe and capillary were positioned 5 mm above the chamber bottom at an equal distance from the inner freezing wall, as indicated in Figure 4.1B. Two studies with and without protein were performed. First, a 200 mM sucrose, 100 mM Tris solution at pH 7.5 was frozen at -20 °C and concentrations measured and predicted are shown in Figure 4.4.
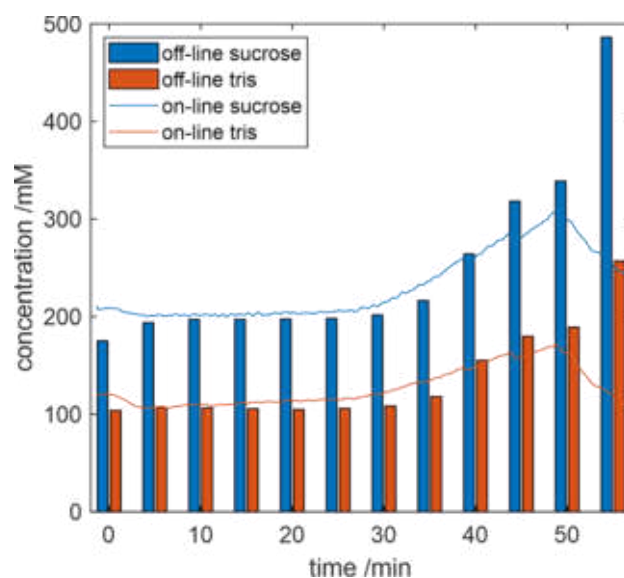
Figure 4.4: Freeze concentration predictions on-line with Raman and off-line by sampling at a 5 min interval. The Raman probe was positioned 5 mm above ground. Tris and sucrose determination by conductivity and density.

Between 5 and 30 min, the solute concentration remained stable with off-line concentrations of 106 ± 1.2 mM Tris and 197 ± 2.5 mM sucrose and on-line predicted concentrations of 112 ± 3.6 mM Tris and 203 ± 3.0 mM sucrose. The agreeing measurements and the low signal variation highlight the PLS model accuracy and the robustness with regards to noise. After 30 min, the solute concentration of Tris and sucrose increased in both on- and off-line measurements. While off-line measurements showed maximum concentrations of 189 mM Tris and 338 mM sucrose after 50 min, the Raman spectra indicated concentrations of 171 mM Tris and 315 mM sucrose. The differences may be attributed to continuous extraction of concentrated sample at the capillary thus adding a source of turbulence and mixing. As a result of the mixing, higher concentrated solution might be aspirated from the lower layers, as shown later.
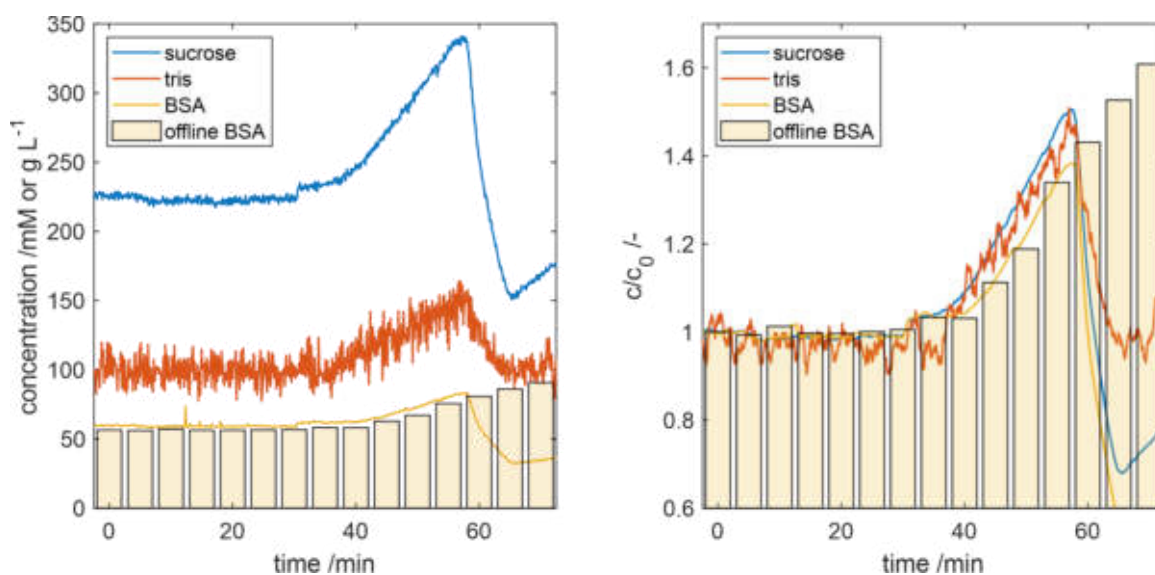
Figure 4.5: Freeze concentration predicted on-line with Raman and measured off-line by sampling at a 5 min interval. The Raman probe was positioned 5 mm above ground. BSA concentration determined by UV-Vis absorption at 280 nm. **A:** absolute concentrations. **B:** Concentrations normalized by initial values.

After 50 min, the freezing front reached both the Raman probe and the capillary leading to an apparent decrease in on-line predicted concentration. The off-line measurements, on the other hand, indicated a steep increase in concentration. While the arrival of the freezing front was clearly detected by Raman spectroscopy, liquid sampling was still possible. The off-line measurements did no longer measure the bulk concentration but instead the freeze concentrated liquid extracted through the capillary. Furthermore, the end of the capillary was located approximately 7 mm away from the Raman probe focal point. Due to the thermal impact of the Raman probe, freeze concentration might have been impacted by the probe itself.

When examining the freeze concentration of a highly concentrated BSA solution with 56 g/L BSA, 100 mM Tris and 225 mM sucrose at pH 7.5, similar results were found, as shown in Figure 4.5. From 0 to 30 min, 59.3 ± 1.1 g/L BSA, 99.4 ± 8.6 mM Tris and 222.9 ± 2.3 mM sucrose were predicted and 56 ± 0.4 g/L BSA were measured off-line. In general, the predicted concentrations show an off-set to the initial concentration of 3 g/L. Adding BSA to the formulation significantly decreased the PLS model robustness of Tris, as standard deviations of up to 9 % were observed over the first 25 min compared to 3 % without BSA. Looking at the relative freeze concentration (c/c_0) shown in Figure 4.5B, the BSA concentration increased by 38 % detected by Raman and by 37 % measured off-line after 57 min (off-line increase interpolated linearly). The root mean square error of prediction (RMSEP) between measured and predicted BSA concentrations was 3.8 g/L absolute and 1.5 % for relative concentrations. In

comparison, Parachalil et al. reported an RMSECV of 1.58 g/L for albumin quantification by Raman spectroscopy from 5 to 50 g/L [131] and Filik et al. reported RMSEPs of 8 to 11 % of the mean concentration [132], which is in range with our model. Other models report lower RMSEPs around 1 mM for glucose [133], but have a smaller upper calibration limit of 24 mM. The presented model focusses on the determination of the relative freeze concentration rather than exact quantification of solutes.

4.3.4. Freeze concentration at different temperatures

A highly concentrated BSA solution of 50 g/L BSA, 50 mM Tris, 225 mM sucrose at pH 7.5 was frozen at different temperatures and monitored with the Raman probe 5 mm above the ground. The influence of the freezing temperature on the freeze concentration profile was investigated. Within the first 5 min of all freezing experiments shown in Figure 4.6 and Figure 4.7, concentrations of 51 ± 0.6 g/L BSA, 32 ± 2.2 mM Tris, and 235 ± 3.2 mM sucrose were predicted. As starting concentrations c_0 remain the same across the experiments, only relative concentrations (c/c_0) of BSA and sucrose are described and discussed in the following.
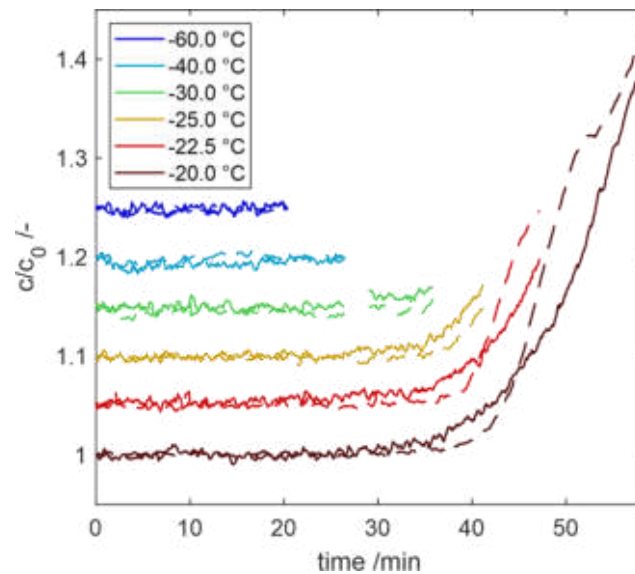
Figure 4.6: Sucrose (-) and BSA (- -) relative freeze concentration at different freezing temperatures. The Raman probe was positioned 5 mm above ground. Concentrations are shifted by 0.05 for visualization purposes. Outliers at -30°C were excluded.

As expected, the freezing time was reduced with decreasing freezing temperatures. Additionally, freeze concentration was not observed when freezing at -40 °C or below. For higher freezing temperatures, the freeze concentration at the time of freezing

increases with temperature. The correlation of freezing time t to the negative inverse of cooling temperature $T_{cooling}$ (t ~ -1/$T_{cooling}$) as well as similar freeze concentration behavior in frozen bulk media was shown previously [120].
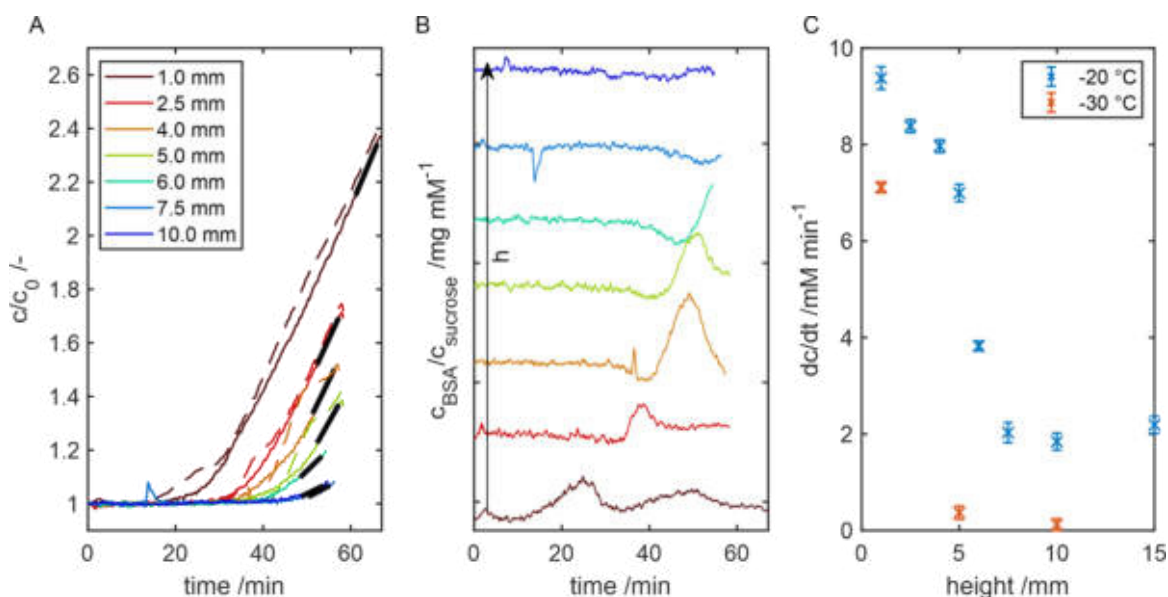
Figure 4.7: Freeze concentration of a BSA formulation at different heights. **A** freeze concentration at -20 °C of BSA (- -) and sucrose (-). **B** freeze concentration at -20 °C of BSA relative to sucrose over time for different heights . The color scheme in A and B is the same. Lines are shifted by increments of 0.03 for visualization purposes. **C** final freeze concentration slope of sucrose prior to freezing as indicated by solid black lines in A.

Looking at the freeze concentration of BSA, the concentration began to increase later than the sucrose concentration after 35 to 40 min and quickly exceeded the sucrose concentration exponentially. The maximum relative concentration difference between BSA and sucrose ($c_{BSA}/c_{BSA,0} - c_{sucrose}/c_{sucrose,0}$) occurring at -20 °C was 11.8 % after 51 min and narrowed down over time to 3.1 % after 58 min.

Interestingly, the freeze concentration showed a similar progression over time throughout all examined freezing temperatures. For example, the relative sucrose concentration exceeds the BSA freeze concentration for all experiments between 20 to 30 min. More specifically, the relative sucrose concentration increased by 1.4 ± 0.25 % after 35 min across freezing temperatures from -20 to -30 °C, and after 40 min by 4.6 ± 0.87 % across freezing temperatures from -20 to -25 °C. This indicates, that freeze concentration and thus the partition coefficient in larger pharmaceutical tanks might be primarily dependent on freezing time. Natural convection can explain this phenomenon as illustrated in Figure 4.8.
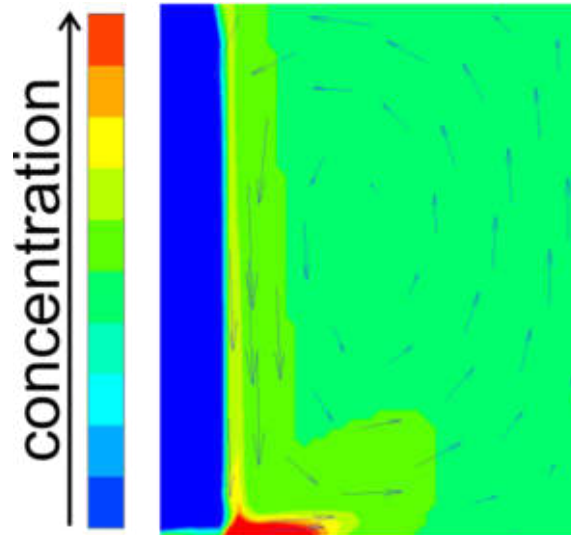
Figure 4.8: Schematic of a freeze concentration profile. The freezing front moves from the left, cooling wall towards the center. Liquid currents are displayed by arrows, where the velocity is represented by arrow length. Diffusion occurs orthogonal to iso-concentration lines. Convective mass transport drags solute enriched liquid along the bottom of the chamber from where it diffuses to the top.

The freezing time correlates with the freeze front velocity, which increased with lower freezing temperatures in this study. However, the freeze concentration was similar over time at different freezing temperatures and thus independent from the freeze front velocity. If the natural convection was negligible, the concentration profile at the freezing front would be dominated by diffusion forming a diffusive concentration layer. This diffusive layer would lead to similar freeze concentration at the end of each freezing process across varying temperatures, when the layer reaches the Raman probe. In this study however, the opposite was found. Convection dominated the freezing processes dragging the concentrated solutes from the freezing front along the bottom to the center and thus reducing the formation of a diffusive layer. Low convection current flow rates are expected at the freezing front and the container bottom. Hence, the current at the bottom needs time to reach the Raman probe. For shorter freezing times at low freezing temperatures faster freeze front velocities will occur. The convective current at the bottom might be slower and thus freeze concentrated solution is entrapped. Hence, similar freeze concentration profiles independent from the freezing temperature indicate convective flow. In addition, similar freeze concentration profiles indicate a constant partition coefficient independent of the freezing temperature. Butler et al. evaluated the freeze concentration in smaller thin films without convection and found a constant partition

coefficient. It was used to describe freeze concentration by a quasi-steady state approximation valid for low molecular weight solutes and at slow freezing speeds. [64]

4.3.5. Freeze concentration at different heights

As indicated in Figure 4.8, natural convection drags freeze concentrated solution to the bottom of a container and freeze concentration time profiles will change along a vertical axis. Therefore, the model solution, containing 50 g/L BSA, 50 mM Tris, and 225 mM Sucrose at pH 7.5, was frozen at -20 °C and monitored at different heights from 1 to 15 mm above the ground. The relative freeze concentration behavior of BSA and sucrose at the different levels in depicted in Figure 4.7A.

The relative freeze concentration was detected first at the bottom of the container and continuously progressed throughout the different layers. More specifically, the sucrose freeze concentration exceeded 101 % after 19, 30, 33, 35, 37, and after 45 min at heights of 1, 2.5, 4, 5, 6, and 7.5 mm, respectively. Freeze concentration of BSA was detected before sucrose at the bottom of the container, but was delayed at elevated heights. The relative freeze concentration of BSA exceeded 101 % after 13, 31, 35, 38, 43, and 52 min at heights of 1, 2.5, 4, 5, 6, and 7.5 mm, respectively.

As freezing continued, freeze concentration of sucrose increased exponentially at the beginning and turned into a linear, steady concentration increase. The maximum relative freeze concentration 1 mm above ground was 2.42-fold for BSA and 2.38-fold for sucrose. It decreased rapidly over height to a 1.42-fold BSA and 1.38-fold sucrose freeze concentration at 5 mm. Other studies evaluated the freeze concentration in a frozen cylindrical vessel by slicing the frozen bulk in 7 mm thick layers and found a two- to threefold increase of BSA and trehalose [16]. Roessl et al. found freeze concentrations of up to 2.5-fold for lactic dehydrogenase and phosphate for frozen sampling over 14 mm sample height [106]. While the results from this study are within the range of the previously described freeze concentrations, they indicate that the freeze concentration measured by frozen sampling may underestimate the maximum freeze concentration by up to onefold as it evaluates the average freeze concentration over a sample height.

The ratio of BSA to sucrose concentration is shown in Figure 4.7B. When comparing freeze concentration of BSA to the freeze concentration of sucrose, it appears, that an initial peak of BSA was transported from the bottom to the top of the freezing chamber. Right before freezing, the ratio of BSA to sucrose concentration $((c_{BSA,end}/c_{BSA,0})/(c_{sucrose,end}/c_{sucrose,0}))$ was similar across all heights with 1.01 ± 0.02 - fold. As these results are the first description of on-line monitored freeze concentration, the following hypothesis is derived. The maximum natural convection occurs at the

beginning of freezing processes [119], as highest density gradients are formed due to the initial large temperature differences in the bulk medium. Higher concentrations of BSA compared to sucrose might be dragged to the bottom of the container. Two potential reasons are a smaller partition coefficient leading to higher exclusion from the freezing front and / or slower diffusion of the larger molecule [134]. The current velocity at the freezing front declines over the distance from freezing front as shown in Figure 4.8. With increasing diffusion coefficients, molecules diffuse further into the convective current due to the orthogonality of the concentration gradient and the convection current. Thus, the freeze concentration at the bottom is a complex interplay between diffusive and convective mass transport at the freezing front. With comparably slow diffusion, BSA might initially not be able to escape the convection flux in contrast to the smaller sucrose molecules. Over time, BSA is dragged to the container bottom by convection. From there it diffuses vertically to the top of the container as the concentration at the bottom continuously increases by convection. This may lead to an initial BSA-rich concentration peak first detected at the bottom.

Under the assumption of negligible contribution of convective mass transport along the observed vertical axis, the data can be used to evaluate the impact of the diffusive flux according to Fick's second law, which describes diffusion over time driven by spatial concentration differences [66]. However, due to the necessity of second order derivation in space, a low number of selected spatial measurements are not sufficient to provide a reliable data set. An external long-distance focal point Raman probe could be used for spatial resolved data set to overcome this issue. In this study, however, mass fluxes can only be interpreted on a qualitative scale. Thus, the slopes of the sucrose freeze concentration over time right before freezing have been fitted, as indicated in Figure 4.7A and are shown in Figure 4.7C for temperatures of -20 °C and -30 °C. From the bottom of the freezing chamber, where the concentration is continuously increased by convection, the concentration slope declines until approximately 7.5 mm above ground, where stagnant slopes where present. The continuously decreasing slopes over the height indicate the degree of diffusion and support the hypothesis of diffusion from the bottom to the top of the container. Additionally, the decreasing slopes over height as well as steadily increasing concentrations imply low turbulences in the freezing process and thus laminar flow. On the other hand, the stagnant slopes in higher layers indicate a diffusion layer in front of the mushy freezing zone that has formed over time. The diffusive layer at the freezing front reaches the Raman probe at similar time across the entire height, explaining the similar degree of freeze concentration found at elevated heights. Exemplarily measured freeze concentration at -30 °C at three heights showed reduced

freeze concentration slope without hardly any detected diffusion layer as shown by the slopes in Figure 4.7C.

Lastly, with increasing distance between probe and chamber ground, the freezing time increased. This can be attributed to the impact of the stainless-steel probe due to heat conduction of the room temperature through the insulation into the freezing chamber. For further studies, this might be avoided by the use of an external Raman probe with a long focal distance.

4.3.6. Formulation dependent freeze concentration

Lastly, the influence of solute concentration on the freeze concentration behavior was investigated for common industrial formulation components. An industrial formulation was mimicked by a mAb formulated in Tris and varying concentrations of stabilizing sucrose. The solutions were frozen at -20 °C and the freeze concentration was monitored at a height of 5 mm. The freeze concentration profiles are depicted in Figure 4.9.
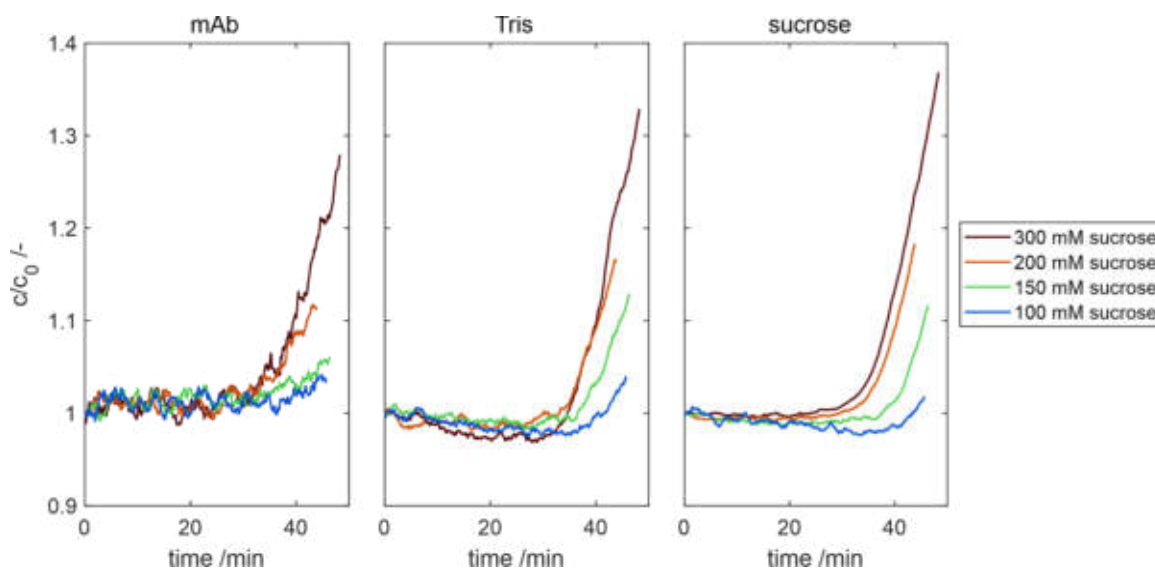
Figure 4.9: Freeze concentration predictions for mAb, Tris and sucrose in formulations with varying amounts of sucrose from 100 to 300 mM. The Raman probe was positioned 5 mm above ground.

The formulations contained 4 g/L mAb, 50 mM Tris and 100 to 300 mM sucrose at pH 7.5. The initial predicted concentrations were 3.9 ± 0.14 g/L mAb, 49.6 ± 2.3 mM Tris and 105, 159, 211, 289 mM Sucrose for the individual formulations. This indicates the model accuracy and in the following, only the relative freeze concentration (c/c_0) will be described. In general, the maximum freeze concentration of mAb increased with sucrose concentration. Maximum freeze concentrations of 1.28-fold mAb, 1.33-fold Tris, and 1.37-fold sucrose were observed right before freezing. Similar to the BSA

case study, low molecular solutes were concentrated to a similar degree. The mAb, however, was least freeze concentrated for all formulations. As mAb with approximately 150 kDa is larger than BSA with 66 kDa, it has a lower diffusion coefficient [134]. Diffusion towards the center reduces the concentration at the freezing front. As shown in Equation 4-I, the amount of solute encapsulated at the freezing front is dependent on the solute concentration at the freezing front. Thus, larger proteins may experience overall less freeze concentration as they are entrapped by the freezing front to a higher degree, which agrees with freeze concentration of different proteins in cell culture supernatant [135]. Kolhe et al. also reported significant differences in sugar and mAb freeze concentration for solutions frozen in bottles [15]. However, the diffusion of the proteins in the two cases is also dependent on the viscosity, which is different for the BSA and mAb formulation.

In addition to that, the final slope of freeze concentration before freezing increased with sucrose concentration for both mAb and sucrose as shown in Figure 4.10. The outlier of mAb freeze concentration at 100 mM sucrose can be attributed to the comparably high noise of the prediction.

Next to higher overall freeze concentration, high sucrose concentrations also led to an
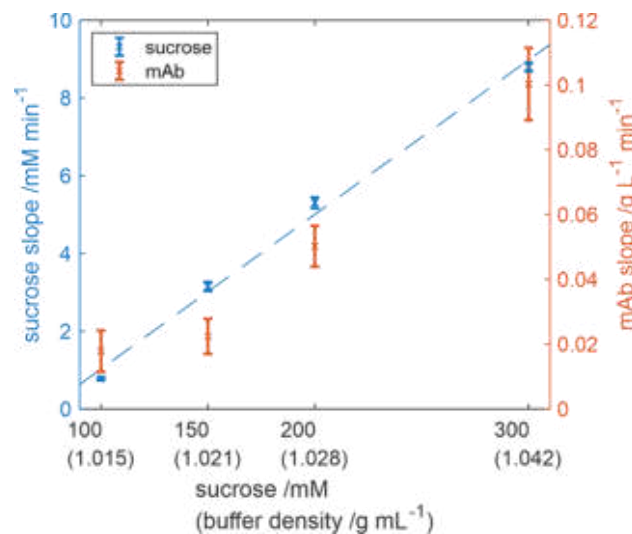
Figure 4.10: Final freeze concentration slope of sucrose and mAb prior to freezing as a function of sucrose concentration. The dashed line is a linear regression of the sucrose slopes. The density of the formulating buffers is proportional to the sucrose concentration and denoted in parentheses.

earlier detection of freeze concentration. Under the assumption of a similar partition coefficient for the given concentrations, more molecules are excluded from the ice matrix upon freezing with increasing concentrations resulting in higher absolute concentration gradients in the liquid phase. Because the measured buffer density is

proportional to the sucrose concentration, higher density gradients in the bulk solution will occur leading to increased convection. In contrast to the BSA freeze concentration, freeze concentration of mAb and sucrose occurred at approximately the same time despite different diffusion coefficients, suggesting that the initial freeze concentration is dominated by convection for formulations with low concentrations of mAb. Furthermore, the viscosity also increases with the sucrose concentration, which reduces diffusive and convective mass transport. For further investigation of convective mass transport in freezing processes, the Grashof number should be evaluated at increasing additive concentrations, requiring the determination of freeze concentration at the freezing front. A coupling of diffusive models and computational fluid dynamics might add to the process understanding of mass transport effects.

4.4. Conclusion

In this study, Raman resonance spectroscopy was thoroughly investigated as a novel approach for process monitoring of pharmaceutical freezing processes. While previous characterization of freeze concentration was limited on the frozen bulk, Raman spectroscopy gives a deeper process understanding on the origin freeze concentration profiles in frozen bulk volumes. Current low-resolution frozen sampling might underestimate freeze concentration by many-fold, as convective flows were in dimensions of 1 mm or thinner. This highlights the importance of spatial high-resolved data acquired by Raman spectroscopy. The qualitative evaluations of diffusional and convectional mass fluxes are a powerful tool for the optimization of freezing processes with regards to process parameters such as temperature and formulation composition. Further information could be retrieved by the using external Raman probe with a long-distance focal length scanning for freeze concentration. This work contributes to quality-by-design freezing processes and formulation development. Product loss due to transient freeze concentration effects can be identified and reduced. The method provides the first real-time data of freezing processes for the validation of scale-down models as well as simulations. Process characterization by Raman monitoring provides proven acceptable and normal ranges for regulatory authorities.

4.5. Acknowledgements

reading of the manuscript and Jan Kehrbaum for his assistance in the laboratory. The authors declare no conflict of interest.

4.6. Supplementary material
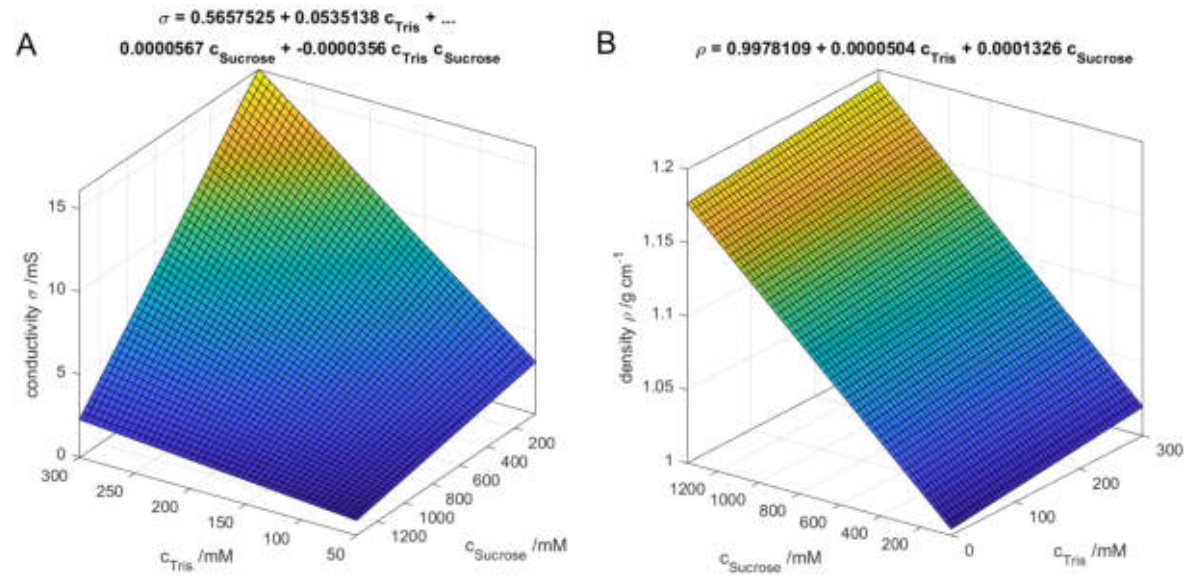
Figure 4.11: Regression models used to estimate sucrose and tris concentration from density and conductivity. **A:** Conductivity model with $R^2 = 0.9985$. **B:** Density model with $R^2 = 0.9998$. Model equations are given in the respective titles.

5

Applicability of available computational fluid dynamic models to predict biopharmaceutical freezing processes

Dennis Weber, Jürgen Hubbuch

Abstract

Freezing is an essential unit operation in the biopharmaceutical industry to increase the shelf of liquid formulations. During the freezing step, solutes are concentrated due to the exclusion from crystallizing water molecules. The freezing time has been identified as a critical process parameter (CPP), which impacts the critical quality attribute (CQA) freeze concentration. In this study, the use of computational fluid dynamics (CFD) was investigated with the aim to predict CQAs and CPPs in freezing processes. The commercially available software package ANSYS Fluent was investigated, which uses the enthalpy-porosity model for description of the solidification process. The freezing time was predicted in a transient simulation using water as a model fluid in a small-scale freezing container. Freezing times predicted at temperatures between -60 and -20 °C were similar to experimental results and confirmed the findings presented in Chapter 3. Extension of the simulation by the predefined species model was performed to investigate the predictability of freeze concentration. Initial simulations were able to qualitatively describe the process of freeze concentration and increased the process understanding by illustrating present mass transport phenomena. However, the results were found to be largely dependent on space and time discretization and physical properties such as viscosity. The average solute concentration in the container was used to identify issues in closing of the solute mass balance. This error method could be applied in further simulations to validate the numerical stability. It was concluded, that the enthalpy-porosity method might

not be suitable to predict freeze concentration in biopharmaceutical freezing operations. Other approaches, such as the phase-field description, might overcome this issue, but have limited availability.

5.1. Introduction

Freeze-thaw processes are frequently used process steps to increase the shelf life of biopharmaceutical products such as monoclonal antibodies. While chemical and physical degradation of proteins is reduced in the frozen solid state due to slower reaction rates, freezing processes may exert additional stresses such as cold denaturation [27], surface denaturation [35] and freeze concentration [123]. Freeze concentration occurs due to the exclusion of solved molecules from the crystallizing water and has been correlated with freezing time. As a result of freeze concentration, solutes are concentrated within the ice crystal matrix. On a larger scale, freeze concentration at the freezing front leads to solute concentration gradients in the solid and liquid phase. In addition, the heat conduction leads to transient temperature gradients in the liquid phase. These temperature and concentration gradients result in density gradients causing buoyancy-driven convection in solidification processes also referred to as 'natural convection' [69], [136]. Furthermore, temperature and solute concentration affect physical properties of the solution such as viscosity and diffusivity. Properties such as heat capacity and conduction are almost constant in one phase, but change dramatically upon phase transition. From a macroscopic point of view, the phase transition occurs slowly in a mushy zone between liquid and solid phase, where ice crystals grow into solution. Freeze concentration occurs in this zone and the resulting convection flows through the zone. To accommodate for the flow resistance by the growing ice crystals, the zone can be described as a porous material. In addition to convective mass transport, diffusion of the concentrated solute away from the freeze concentrated walls occurs. These mass transport phenomena lead to a challenging problem when it comes to optimization of freezing process.

To reduce the freeze concentration in the frozen bulk, low freezing temperatures or narrow freezing containers can be used. However, handleability issues of low temperatures during storage and transportation, as well as volume limitations, make it necessary to optimize the freezing process. Mechanistic modelling provides a promising tool for process optimization, with increasing interest in the biopharmaceutical industry [21]. Biopharmaceutical freezing processes have been simulated recently by computational fluid dynamics (CFD) to describe freezing temperatures [106] and freeze concentration [119], [122]. However, recent CFD simulations were restricted to the description of a single case while concerns were raised with regards to numerical stability. Therefore, the reliability of predictions has

to be investigated. Furthermore, the availability of the models is restricted due to the modifications and implemented add-ons. Therefore, it is the aim of this work to test the applicability of a commercially available CFD software to model and predict biopharmaceutical freeze-thaw processes. The critical process parameter (CPP) freezing time and critical quality attribute (CQA) freeze concentration identified in Chapters 3 and 4, respectively, should be modeled. A commercial software package that provides the basic framework should be investigated on the premise of enabling simulation without the complexity of in-depth modifications. Furthermore, the independence of the simulation solution from physical properties is investigated, which is necessary for the prediction of freeze-thaw processes.

5.2. CFD environment

Numerous software solutions are available for the mechanistic modelling of fluid mechanical problems. In the presented work, the software package ANSYS Fluent 2020 R2 (Ansys Inc, PA, USA) was used. The software package has been used for solidification processes in metal casting and thus provides the necessary models to simulate freezing processes. In addition, the implemented enthalpy-porosity model used for the simulation of solidification has been shown previously to describe freeze concentration [119]. To model the CPP freezing time and the CQA freeze concentration, a simplified single component model was simulated in the first part of the study. In the second part, freeze concentration was evaluated by extension of the model with the species model.

5.2.1. Geometry setup and physical properties

A small-scale freezing container designed as a slice of a hollow tube was modelled. It was cooled from the in- and outside and modelled as a 3D-case using DesignModeler (Ansys Inc, PA, USA) to accommodate for radial volume expansion as shown in Figure 5.1. The width of 62 mm and height of 30 mm are equal to the small-scale model presented in 3.2.2. The model was meshed into cuboid cells with a varying length Δx from 0.1 to 1.5 mm. Under the assumption of negligible tangential boundary conditions, the walls in tangential direction were implemented as symmetric boundaries. The top and bottom of the container were implemented as adiabatic, zero heat flux walls. Cooling at the container wall was implemented by time dependent temperature profiles T_{cool} observed at the entrance of the small-scale model to accommodate for cooldown times described in 3.3.1. Temperature profiles for -20, -25, -30, -40, and -60 °C were implemented.
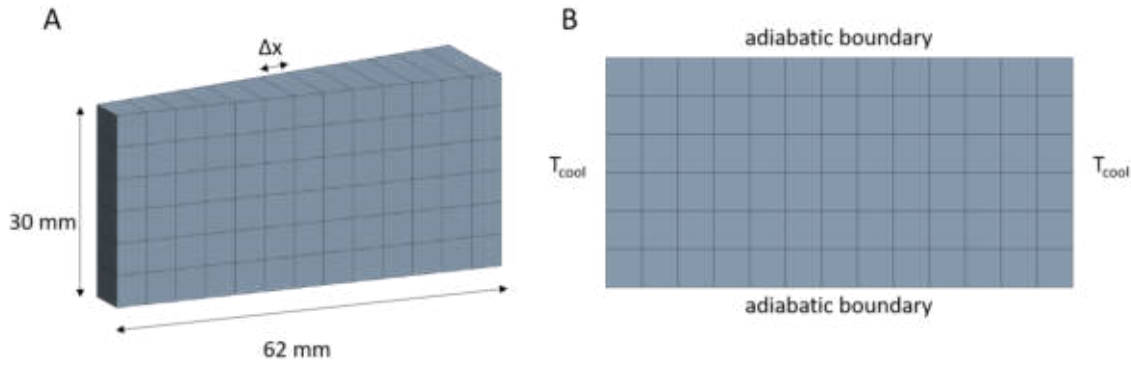
Figure 5.1: Case overview. **A:** dimensions and exemplary representation of the cell width *Δx*. **B:** boundary conditions used for the model. The shown cell width exceeds the modelled maximum width to enhance visualization.

In the first part of the study, the freezing of pure water was investigated for comparison with freezing time estimates described in chapter 3. The physical properties of water used are summarized in Table 5.2 in the Supplementary material. Temperature dependent properties were approximated using linear interpolations with up to 3 sampling points. A freezing temperature of 0 °C was used as solidus and liquidus temperature. Outside the defined temperature range, the nearest given property value was used.

In the second part, the simulation of freeze concentration was performed using a sample solution with 0.15 %w/w sucrose modelled as a two-component mixture with the species model provided by ANSYS Fluent. The physical properties are summarized in Table 5.1. Properties dependent on temperature and solute concentration were implemented as user defined functions (UDF). The differences in thermal conductivity and latent heat from sucrose solutions to water were assumed to be negligible. In addition to the mixture properties, the components of the mixture were defined as summarized in

Table 5.3 in the Supplementary material.

Table 5.1: Properties of the sucrose mixture implemented to model freeze concentration. T represents the temperature in K, w_s the sucrose mass fraction, w_w the water mass fraction and β the liquid fraction. Literature (Lit.) resources are given in the last column.

Property	Value functions		Lit.
Density ρ /kg m^{-3}	$\rho = 1/(w_s\,\rho_s + w_w\,\rho_w)$		
Viscosity μ /kg m^{-1} s^{-1}	$\mu = 0.001\,(0.5791 - 0.05032\,(T - 273.15) + 20.23\,w_s + 0.002893\,(T-273.15)^2 - 0.6117\,w_s\,(T-273.15))$		[51]
Heat capacity c_p /J kg^{-1} K^{-1}	$c_p = 1116 + 3.34\,T,$	if ($\beta < 0.05$)	[137]
	$c_p = (1-\beta)\,(1116+3.34\,T) + \beta\,(4140-2460\,c +\dots\\ 0.665\,(T-273.15)\,(1+w_s)^3),$	if ($\beta < 0.95$)	
	$c_p = 4140-2460\,w_s + 0.665\,(T-273.15)\,(1+w_s)^3,$	if ($\beta \geq 0.95$)	[138]
Diffusivity D /m^2 s^{-1}	$D = 3.3\,(1 - 1.26\,w_s)\,10^{-\left(6+\frac{1137}{w_s}\right)}$		[139]

5.2.2. Models and governing equations

The presented work focusses on the applicability of the implemented models to investigate predictability by available, mechanistic simulations. Thus, only the models and main equations used in ANSYS Fluent are described in the following.

Fluid dynamic models

Under the assumption of low Reynolds numbers, a laminar flow model was selected for incompressible media. A semi-implicit method for pressure linked equations (SIMPLE) was used for pressure-velocity coupling. Implemented discretization schemes in ANSYS Fluent were evaluated in preliminary experiments. The selected spatial schemes are summarized in Table 5.4 in the supplementary material. For the transient formulation, a second order implicit formulation was used.

Solidification model

To describe the solidification, the enthalpy-porosity method can be used [140]. The freezing front is formulated as a mushy, porous zone. As a cell solidifies, the porosity changes along with the liquid fraction from 1 to 0 according to the enthalpy balance. The energy equation is calculated with Equation 5-I after Voller et al. [140]. In the equation, t represents the simulated time, ρ the fluid density, $\vec{v}$ the fluid velocity, k is the heat conductivity, T the temperature and S a source term.

$$\frac{\partial}{\partial t}(\rho\,H) + \nabla \cdot (\rho\vec{v}H) = \nabla \cdot (k\nabla T) + S \qquad \text{5-I}$$

The enthalpy H is calculated from equation 5-II,

$$H = h_{ref} + \int_{T_{ref}}^{T} c_p dT + \Delta H \qquad \text{5-II}$$

where h_{ref} is the material enthalpy at a reference temperature T_{ref} and c_p is the heat capacity. The latent heat content ΔH is calculated from $\Delta H = \beta L$, with the latent heat L of the material. The liquid fraction β is dependent on the solidus T_{solid} and liquidus T_{liquid} temperature in the case of multicomponent solutions. It is calculated after Equation 5-III.

$$
\begin{aligned}
\beta &= 0 & &\text{if } T < T_{solid} \\
\beta &= 1 & &\text{if } T > T_{liquid} \\
\beta &= \frac{T - T_{solid}}{T_{liquid} - T_{solid}} & &\text{if } T_{solid} < T < T_{liquid}
\end{aligned}
\qquad \text{5-III}
$$

For pure substances, such as freezing of water, an enthalpy based approach is used for determination of the liquid fraction [140], as the solidus and liquidus temperatures are equal. For mixtures, the solidus and liquidus temperatures are calculated from the liquidus line found between the melting point of the pure solute and the eutectic point in a phase diagram (see Figure 1.3).

The mushy zone is modeled as a porous structure in the enthalpy-porosity method. An approach after the Kozeny-Carman equation is used to describe fluid flow in the porous media, where porosity is defined by the liquid fraction β.

$$S = \frac{(1 - \beta)^2}{\beta^3 + \epsilon} A_{mush} \, \vec{v} \qquad \text{5-IV}$$

In equation 5-IV, ϵ is a small number to avoid division by zero and A_{mush} is a damping constant. The higher the damping constant the slower the flow in the mushy zone with default values between 10^5 and 10^7.

In general, the segregation of a solute in the solid and liquid phase is described by the partition coefficient k. It is calculated from the ratio of the concentration encapsulated in the solid phase c_{solid} by the concentration in the liquid phase c_{liquid}. The mass fraction of solute was calculated after Scheil under the assumption of zero diffusion in the solid phase after equation 5-V.

$$
\begin{aligned}
\frac{\partial}{\partial t}&\left(\rho Y_{i,liq}\right) + \nabla \cdot \left(\rho \beta \vec{v}_{liq} Y_{i,liq}\right) \\
&= \nabla \cdot \left(\rho \beta D_{i,m,liq} Y_{i,liq}\right) - k_i Y_{i,liq} \frac{\partial}{\partial t}\left(\rho(1 - \beta)\right) + \frac{\partial}{\partial t}\left(\rho(1 - \beta) Y_{i,liq}\right)
\end{aligned}
\qquad \text{5-V}
$$

In the equation $Y_{i,liq}$ is the solute mass fraction in the liquid phase and $D_{i,m,liq}$ is the solute diffusion coefficient where the subscript i denotes the solute.

5.2.3. Data post-processing

To monitor the solidification progress, an average of the solid fraction was calculated over the radial cross-section as depicted in Figure 5.1B. Furthermore, the conservation of solute mass did not close during the simulation of freeze concentration. To investigate the solver accuracy, an area average mass fraction of the solute over the radial cross-section was calculated. Ideally, the average mass fraction remains constant by conservation of mass. Deviations from the constant value indicate inaccuracy caused by the solver.

5.3. Results and Discussion

In the first part of the study, freezing of water was simulated with the aim of investigating freezing time predictions. In the second part, the established model was extended by the species model available in ANSYS Fluent to evaluate the simulation of freeze concentration.

5.3.1. Freezing time predictiong

The independency of the model from the mesh size was tested by varying the cell length from 0.5 to 1.0 to 2.0 mm resulting in 7440, 1860, and 465 cells, respectively.A constant time step size of 0.05 s was used, which was identified as sufficient in preliminary experiments. A cooling temperature profile of -20 °C was used in the study. The solidification progress monitored as described above is depicted in Figure 5.2 for the respective mesh resolutions.
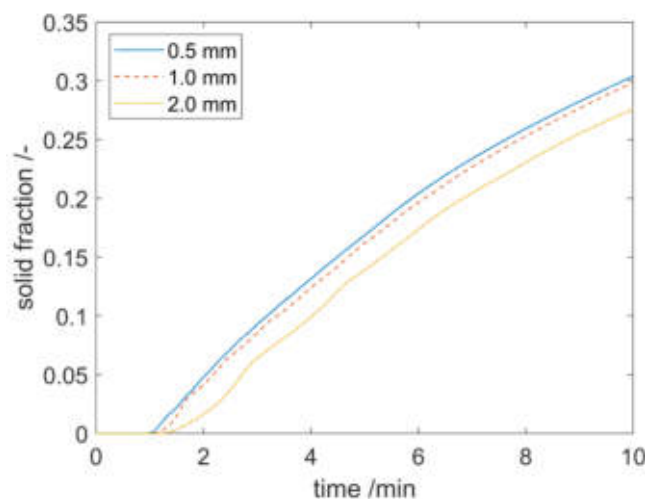
Figure 5.2: Freezing progress over time simulated at -20 °C. Pure water was used and mesh cell lengths were varied.

The freezing time was defined as the duration until no liquid fraction was found in the container. With an increasing number of cells, the freezing time decreased from 77.0

to 73.6 to 73.4 min for cell lengths of 2.0, 1.0, and 0.5 mm, respectively. As a result, a cell length of 1.0 mm was found to be sufficient for predicting the solidification of pure water.

Natural convection was observed in the liquid region as a result of thermal buoyancy. The damping constant A_{mush} influences the convection in the mushy zone and thus potentially the heat transfer. Therefore, the damping constant was varied from 10^5 to 10^{10}. As a result, the maximum velocity in gravitational direction increased from 41.1 to 42.0 to 42.2 to 42.4 mm/min for damping constants of 10^5, 10^6, 10^7, and 10^{10}, respectively. However, the simulated freezing times varied between 73.9 ± 0.74 min without a trend. Thus, the influence of the damping constant on the freezing time was considered negligible, representing the impact of convection on the heat transfer. Oosthuizen et al. also reported negligible influence of convection on the heat transfer rate, but stressed the influence of the width to height ratio of the freezing container, where convection is more pronounced in wider cavities [136].

Furthermore, freezing times at different temperatures where predicted and compared against the results from Chapter 3. The results are depicted in Figure 5.3. In general, simulated freezing occurred 5.0 ± 1.5 min faster than the experimentally observed. The faster freezing times can be attributed to the heat loss in the system, which is not accounted for in the simulation. For the simulation, wall temperatures were set to the cooling fluid's temperature at the entrance of the freezing device. However, the wall temperature in the freezing device is expected to lack behind the cooling fluid temperature as the temperature difference between the in- and outlet of the freezing device decreases from 3 to 0.5 K over time. Furthermore, the initial temperature of
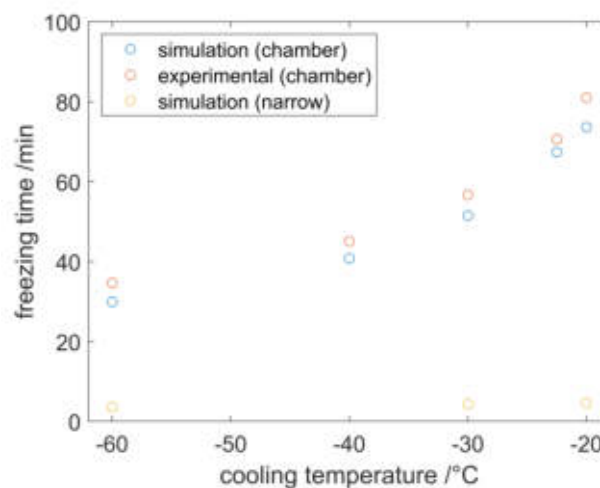
Figure 5.3: Validation of freezing time prediction. Experimental data are from Figure 3.4. Yellow points represent predicted freezing times in a narrow freezing chamber with 10 mm width.

the water in the simulation was set to 5 °C, which was the equilibrium temperature of the cooling fluid, whereas measured temperatures ranged from 5.4 to 6.0 °C initially.

In Chapter 3, it was suggested, that the influence of the set freezing temperature on the freezing time will decrease in case of narrow freezing containers due to heat transfer limitations. Therefore, the freezing times were simulated for a container with a width of 10 mm. As shown in Figure 5.3, the freezing time of 4.2 ± 0.5 min did not change considerably in between cooling temperatures of -20 to -60 °C. This agrees with the hypothesis and shows, that cooling temperatures might not affect freeze concentration in freezing containers with close cooling walls such as freezing bags. As a conclusion, CFD in combination with information on available cooling capabilities can be used to optimize cooling temperatures and maximum container widths with regards to freeze concentration. However, in the authors' opinion, the freezing times in simple container geometries can be approximated by the Plank equation with less computational effort as shown in Chapter 3.

5.3.2. Thermal convection in aqueous solutions

The density anomaly of water, with a peak density of 1000 kg/m^3 at 4 °C, leads to convection vortices in the chamber, that invert over the course of a freezing process as shown in Figure 5.4 by velocity vectors for freezing of pure water. Initially, the density increases when the temperature approaches 4 °C from the starting temperature, leading to a flow in gravitational direction at the cooling wall, referred to as 'hot vortex'. As the temperature decreases further, the density starts to decrease leading to a buoyant force and an inversion of the vortex at the freezing front, known as 'cold vortex'. Until the maximum temperature is below 4 °C, two vortices in opposite direction are be present in the liquid phase. This phenomenon has been investigated experimentally [141] and described as cold and hot vortices below and above the temperature of maximum density, respectively.

Considering this phenomenon for biopharmaceutical freezing processes, the hot vortex may enhance the gravitational convection induced by freeze concentration, whereas the cold vortex might reduce freeze concentration. The density anomaly of water has been thoroughly described in literature, whereas the impact of solutes on the density anomaly lacks of documentation in the temperature range of interest. Wada et al. reported a shift of the temperature at density maximum by -2.51 K at 28 mol% sucrose
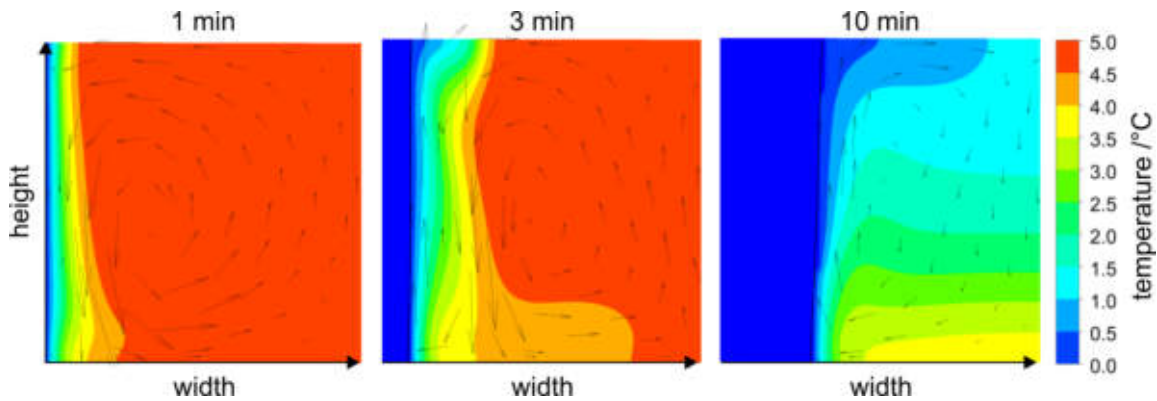
Figure 5.4: Simulated temperatures and fluid velocities of water frozen with cooling temperatures of -20 °C. Half of a cross section is displayed for visualization and symmetry reasons after 1, 3, and 10 simulated minutes. The velocity is indicated by arrows where the arrow length represents the magnitude. The temperature is depicted as a contour plot from 0 to 5 °C to visualize the temperature gradients in the fluid region. A solid black line indicates the freezing front, with 50 % liquid fraction.

[142], but did not describe the shift of the density slope. A lower temperature at density maximum may increase the duration of the hot vortex. Due to freezing point depression, the temperature range of the cold vortex increases approximately by 0.09 K/(w/w) for sucrose in the range from 0 to 0.3 w/w sucrose [143]. In previous works on the simulation of biopharmaceutical freezing processes, the density anomaly was considered negligible [119] or the shift of the density maximum was not accounted for [122]. The thermosolutal convection has been discussed for casting processes previously and the need for precise phase equilibrium data has been pointed out [65]. While the sucrose-water system is well described in literature [44], [51], [52], [54], [144], phase diagrams of pharmaceutical proteins are different even within similar protein classes [26]. Thus, phase diagrams and physical properties of the investigated system need to be measured in the area of interest, including the variation of additives and the supercooled region below 0 °C. In conclusion, the results show presence of hot and cold vortices in aqueous solutions. Especially in slow freezing processes of large volumes from room temperature, hot and cold vortices are to be expected. In biopharmaceutical freezing processes, the impact of the thermal buoyancy might be superseded by the solutal density increase. Further investigations are necessary to estimate the importance of thermosolutal convection.

5.3.3. Freeze concentration simulation

After modelling the freezing process of water, the simulation was extended by the species model to include freeze concentration processes. Preliminary simulations showed, that freeze concentration and natural convection were simulated successfully.

The results were used to illustrate and explain mass transport phenomena on a qualitative basis as shown in Figure 4.8 and below in Figure 6.7.

For quantitative prediction and reliability, the solution independency from physical properties was investigated in a next step. As the physical properties of the solution change with temperature and concentration, the impact of viscosity on the model accuracy was investigated by calculating the average solute concentration in the simulated volume. For a desired closing mass balance, the average solute concentration would remain constant. Freezing at -20 °C with a mesh size of 1 mm and a time step size of 0.05 s was simulated at fixed viscosities from 1 to 10 mPas, as the viscosity of sucrose solution varies between 1 and 2 mPas from 0 to 20 %w/w. With decreasing viscosity, increasing solute mass imbalances were observed as shown in Figure 5.5. Over 50 simulated minutes, the mass balance deviated by 0.3 % and 2.9 % at viscosities of 10 mPas and 1 mPas, respectively. Overall, the simulation of 73 min was calculated after 23 h. The mass balance inaccuracies caused by viscosity dependent freeze concentration led to maximum freeze concentrations over time of 1.22-, 1.20-, and 1.30-fold the initial concentration for viscosities of 1, 5 and 10 mPas, respectively. Despite the difference in viscosity and thus mass transport, no trend was observed in the maximum freeze concentration indicating solution inaccuracies. Mass balance errors are attributed to calculation errors in the mushy zone. Furthermore, the calculated mass balance is averaged over the whole volume. Thus, the error at the freezing front might be underestimated.

As smaller viscosities increase the mass transport, smaller time steps are necessary to improve the simulation accuracy, especially for the mushy zone region. Therefore, the time step size was decreased from 0.1 to 0.005 s for freezing simulations at -20 °C
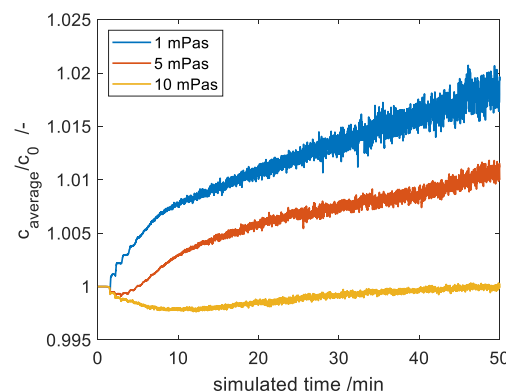
Figure 5.5: Model accuracy at different viscosities when simulating freezing at -20 °C with a mesh size of 1 mm and a time step size of 0.5 s. The average solute concentration normalized by the initial concentration is plotted against the simulated time.

at a mesh size of 1 mm and a viscosity of 5 mPas. The resulting average concentrations are depicted in Figure 5.6. Overall, decreasing time steps reduced the mass imbalances. Large time steps led to an initial mass loss between 1 and 7 min, followed by an increasing solute concentration. Decreasing the time step size below 0.01 s led to similar results. However, processing time to simulate 5 min increased from 0.9 to 1.3 to 8.5 and 15.6 h for time steps of 0.1, 0.05, 0.01, and 0.005 s, respectively.
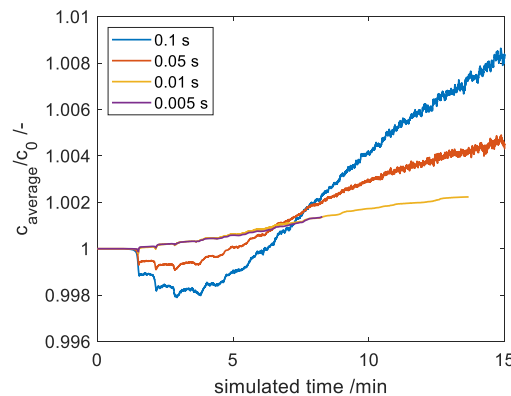
Figure 5.6: Numerical stability at decreasing time steps. Viscosity of 5 mPas, freezing temperature of -20 °C and a mish size of 1 mm was used. **A:** Average solute concentration relative to the starting concentration.

The mass imbalances are reflected in the solute concentration gradients in the frozen bulk increases as shown in Figure 5.7. The freeze concentration homogeneity was defined as the ratio of maximum by minimum concentration (c_{max}/c_{min}) in the frozen bulk. It decreased from 1.559 to 1.552 to 1.534 with decreasing time step sizes of 0.2, 0.1 and 0.05 s, respectively. In general, the concentration in diluted areas decreased with larger time steps and increased in the concentrated areas. Thus, freeze concentration profiles are impacted by the set time step rather than the prediction of physical mass transport phenomena.

As shown in Figure 5.6, the mass imbalances decreased step-like in the beginning. This can be attributed to the completion of solidification of a column of cells close to the cooling wall, indicating a dependence of the prediction on the mesh resolution. With higher mesh resolution, the accuracy was observed to increase (data not shown). With decreasing mesh cell sizes and at lower, realistic viscosities, smaller time steps will be necessary as suggested by the Courant–Friedrichs–Lewy condition [145] which is used to describe convergence in differential equations. Therefore, the time step study was performed at an artificially increased viscosity to improve the solver accuracy. The estimated processing time to simulate a freezing process with a viscosity of 5 mPas, a time step size of 0.01 s and a freezing temperature of -20 °C is 5.3 days, which increases by manifold at necessary smaller time steps. The processing time was restricted by memory band width rather than computational power due to the small

number of cells. Thus, increasing the number of central processing units by using high-performance cluster solutions did not speed up the simulation. A complete mesh study as shown for the prediction of freezing times in water was considered disproportionate due to the necessary simulation time.
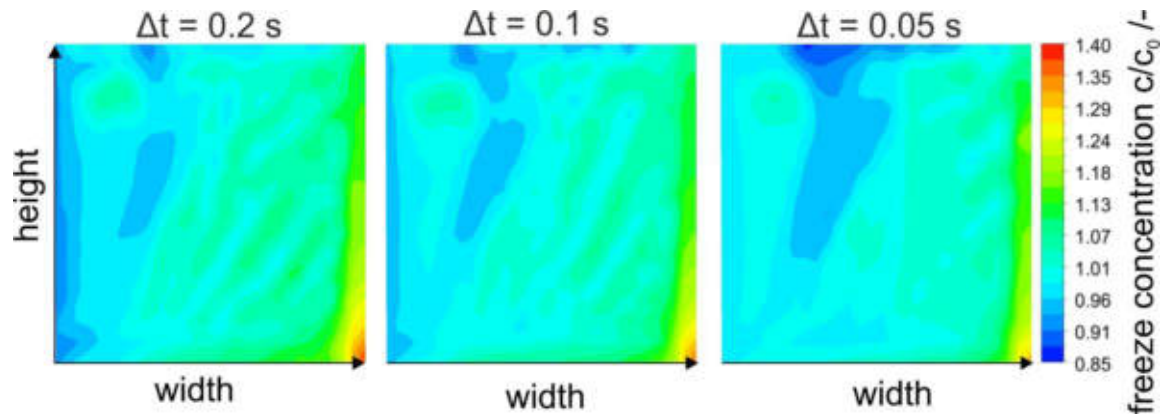
Figure 5.7: Freeze concentration in frozen bulk after freezing at different time steps. Half of a cross-section is depicted due to symmetry. The freezing temperature was set to -20 °C, the mesh resolution was 1 mm and the viscosity was fixed to 5 mPas for comparability with previous results.

Furthermore, at small time steps, changing the partition coefficient did not impact the freeze concentration significantly. Thus, the implemented solver did not reflect the physical properties. Different pressure-velocity coupling schemes, spatial discretization and adaptation of the under-relaxation factors were tested, but did not improve the results. As the model did not satisfy the need for stability, the simulations were not validated by transient concentration data.

The applied models for simulation freeze concentration are highly affected by numerical instabilities and most likely lead to unphysical results when not properly evaluated. The freeze concentration simulated by the implemented models were dependent on discretization and decoupled from physical properties. Unfortunately, very little information on numerical stability is given in recent work on the simulation of biopharmaceutical freezing processes. Geraldes et al. [119] have shown a description of a freezing process using the enthalpy-porosity method, where a sucrose solution was frozen at -10 °C. While concern with regards to numerical stability were raised and small under-relaxation factors were used, a mesh-study was not shown and a cell size of 1 mm was suggested. Furthermore, the time-step size was not mentioned. Validation of the simulation was performed with concentrations measured in the frozen bulk. In the authors' opinion, the endpoint validation gives little information on the transient process of freeze concentration. While a large screening of time steps,

partition coefficients and mushy zone parameters might lead to an appropriate description of one specific freeze concentration process, the predictability for new products or process conditions remains questionable.

5.4. Conclusion and outlook

In the presented work, simulation of the two critical process parameters freezing time and freeze concentration was conducted. The simulation of freezing time was successfully approximated by modelling freezing water. After a mesh study, the reliability of the predicted freezing times was validated by freezing time experiments. In addition, the freezing times of a narrow freezing container were predicted at temperatures from -60 to -20 °C, where the freezing times did not change considerably. Thus, the relevance of the ratio of cooldown time to freezing time was shown as suggested in Chapter 3. The model for freezing time prediction facilitates the optimization of freezing processes with regards to freezing time and freezing container design. Investigations of the water density anomaly revealed the presence effect of hot and cold vortices due to thermal convection, which potentially impacts the freeze concentrations in slow freezing processes.

Modelling the freeze concentration was challenging, as the implemented model showed a high dependency on discretization parameters. A reduction in both time step size and cell size is necessary to improve the robustness, but is not feasible due to hardware limitations. However, the qualitative process description and the analysis of the results was used to improve the process understanding as shown in Figure 4.8 and later in Figure 6.7. For quantitative freeze concentration predictions, improvements in the spatial discretization might be necessary. Furthermore, phase-field modelling has shown promising results on the simulation of freeze concentration on a microscopic [108] and macroscopic scale [122], but are not yet widely available.

5.5. Supplementary material

Table 5.2: Physical properties of water for the prediction of freezing times

Property	Value at a given temperature
Density ρ /kg m^{-3}	$\rho(0\ °C) = 999.87$; $\rho(4\ °C) = 1000.0$; $\rho(10\ °C) = 999.75$
Dynamic viscosity μ /kg m^{-1} s^{-1}	$\mu(0\ °C) = 0.001787$; $\mu(5\ °C) = 0.001519$
Heat capacity c_p /J kg^{-1} K^{-1}	$c_p(-0.15\ °C) = 2108$; $c_p(0.05\ °C) = 4181$
Thermal Conductivity λ /W m^{-1} K^{-1}	$\lambda(-0.15\ °C) = 2.22$; $\lambda(0.05\ °C) = 0.6$
Latent Heat /J kg^{-1}	334000

Table 5.3: Used properties of sucrose and water components of the mixture. Sucrose density and liquidus slope were determined iteratively

Property	Sucrose	Water
Density ρ /kg m^{-3}	1600	See Table 5.2
Molecular weight /kg mol^{-1}	342	18
Slope of liquidus line /K	-4	0
Eutectic mass fraction	0.63	1

Table 5.4: Spatial discretization schemes used in ANSYS Fluent

Variable	Scheme
Gradient	Least Squares Cell Based
Pressure	PRESTO!
Momentum	Second Order Upwind
Solute	First Order Upwind
Energy	Second Order Upwind

6

Impact of freeze-thaw processes on monoclonal antibody platform process development

Dennis Weber[1], Christian Sittig[1], Jürgen Hubbuch[1]*

[1] Institute of Engineering in Life Sciences, Section IV: Biomolecular Separation Engineering, Karlsruhe Institute of Technology (KIT), Fritz-Haber-Weg 2, 76131 Karlsruhe, Germany

* Corresponding author.

Abstract

Freezing of cell culture supernatant (CCS) is a standard procedure in process development of monoclonal antibody (mAb) platform processes as up- and downstream development are usually separated. In the manufacturing process of mAb, however, freezing is avoided, which poses the question of comparability and transferability from process development to manufacturing. In this case study, mAb CCS from Chinese hamster ovary (CHO) cells is frozen and thawed in a novel active freezing device and subsequently captured by protein A chromatography. Critical quality attributes such as host cell protein (HCP) concentration and soluble mAb dimer shares have been monitored throughout the case study. Furthermore, cryo-concentration of individual proteins was investigated. The main factors that drive cryo-concentration are diffusion and natural convection. Natural convection in freezing processes was found to increase at warmer freezing temperatures and thus slower freezing, leading to higher concentration gradients from top to bottom of a freezing chamber. The freeze concentration was dependent on protein size and correlated to diffusivity, where smaller proteins are exposed to higher cryo-concentration. Our results suggest that as a result of freezing processes, large particles based on mAb and specific HCPs expressing a certain affinity to mAbs are formed that have to be removed prior to

purification. This leads to a significant improvement in HCP reduction by the protein A step, when compared to reference samples, where twice as much HCP remained in the eluate. Furthermore, HCP and mAb dimer concentrations in protein A eluate were dependent on the freezing temperature. As a conclusion, CCS should be frozen as rapidly as possible during process development to minimize issues of transferability from process development to manufacturing.

6.1. Introduction

In the biopharmaceutical market, monoclonal antibodies (mAb) are the most important class of proteins to date. Hence, many studies with industrial interest in the improvement of the manufacturing process have been published leading to the establishment of a platform process for mAb purification [146]. A typical manufacturing process involves three major steps: cell culture, purification and formulation. During large-scale manufacturing, each of these steps is performed subsequently, whereas all steps are evaluated individually during process development. Additionally, the up- and downstream manufacturing parts are usually located on one manufacturing site, while filling of the drug product is often done at different locations. Therefore, the product is often frozen to reduce the risk of product loss by microbial growth, foam prevention, and mechanical stress during transportation and hold times in process development [15], [49]. However, freeze-thaw process steps come with disadvantages that might lead to protein activity loss [28] such as cryo-concentration, protein-ice surface interaction [35], and cold denaturation [27]. These freeze-thaw stresses might lead to protein aggregation [147] and even native aggregate particle formation, which was previously reported for mAb [148]. Because of the high importance to the drug industry, several studies on freeze-thaw processes of mAb formulations have been performed [13], [14], [71]. Such freezing processes are often categorized by scale and mode of cooling. Actively cooled freezing processes involve a cooling fluid, which is in contact with the container wall, whereas containers frozen in larger freezers are referred to as passive freezing processes. Across all freezing processes, cryo- or freeze concentration occurs due to exclusion of the solutes from ice crystals. This phenomenon is also well described for different solidification processes in various areas such as alloys [100]. From a macroscopic view, the area of solidification at the freezing front, where crystals grow into solution, is described as a 'mushy zone'. As a result of freeze concentration, buoyancy driven flows also known as 'natural convection' occur in the mushy zone and the remaining liquid in large scale-processes, due to density gradients. In addition to natural convection, diffusion of solutes also leads to cryo-concentration [64], which can be described by Fick's law.

As pointed out initially, up- and downstream process development is often done with hold times in between and process intermediates have to be frozen to increase their shelf life. This step is avoided during the manufacturing process to minimize the risk of product degradation. Despite this major difference in process development and manufacturing, no studies have been presented yet on the transferability of data characterizing unit operations across scales, where different sample preparations (frozen vs. reference) were applied. Therefore, this work investigates the impact of an additional freeze-thaw cycle prior to a typical protein A step using cell culture supernatant (CCS) from Chinese hamster ovary (CHO) cells with mAb. Furthermore, characterization of complex freezing processes with multiple proteins is performed to provide a better understanding of freezing processes.

6.2. Materials and Methods

6.2.1. Buffer preparation

All buffers have been prepared from sodium chloride (NaCl), sodium acetate (NaAc), potassium chloride (KCl), potassium hydrogen phosphate ($KHPO_4$), sodium dihydrogen phosphate-monohydrate (NaH_2PO_4 H_2O), sodium hydroxide (NaOH), and acetic acid (CH_3COOH) from Merck (Darmstadt, Germany), di-sodium hydrogen phosphate dihydrate (Na_2HPO_4 $2H_2O$) from Sigma Aldrich (Steinbach, Germany), and 20X phosphate-buffered saline (PBS) Tween™-20 from Thermo Fisher Scientific (Massachusetts, USA). The buffer salts were dissolved in ultrapure water (PURELAB Ultra, ELGA LabWater, Veolia Water Technologies, Saint-Maurice, France). After adjusting the pH of all buffers to the desired pH $\pm$ 0.1 using concentrated hydrochloric acid, acetic acid, or NaOH, all buffers have been filtered using 0.2 µm filter membranes and degassed in an ultra-sonic water bath.

6.2.2. Monoclonal antibody preparation

Cell culture supernatant (CCS) of a mAb harvest with a titer of 2 g/L from Chinese hamster ovary (CHO) cells was kindly provided by Byondis (Nijmegen, The Netherlands). Due to the lack of stability of CCS, handling and storage of CCS is not possible without freezing. Thus, the product was frozen at -80 °C post cell removal at the production site, and stored in 1 L bottles until further use. In order to adjust the sample volume, CCS from 1 L bottles has been thawed in a water bath at 25 °C for 2 to 3 h, aliquoted into 50 mL centrifugation tubes by Corning Life Sciences, USA, at 45 mL and frozen at -80 °C until further use. Prior to an experiment, the required number of aliquots have been thawed in a water bath at 25 °C, pooled, and filtered with 0.2 µm filters. In total, the harvest was freeze-thawed twice and filtered once before conducting the case study. This may influence the outcome of the study, but

mirrors typical handling of process development samples in industry. This said, the significant results obtained in this study highlight the mechanisms occurring in any freeze-thaw process during sample handling. The twice freeze-thawed harvest prior to our study will be referred to as the 'reference sample'.

6.2.3. Freeze-thaw process

Controlled freezing and thawing was done in a small-scale freezing device designed and manufactured in cooperation with Industrietechnik Salzburg Bilfinger (Salzburg, Wien). The freezing container is designed as a hollow tube cooled from the in- and outside. The used scale-down model is designed as a thin slice of a larger scale, that is separated into six wedges by an insulating inlay of polytetrafluoroethylene (PTFE). A schematic drawing of the freezing device and a sample chamber are displayed in Figure 6.1.
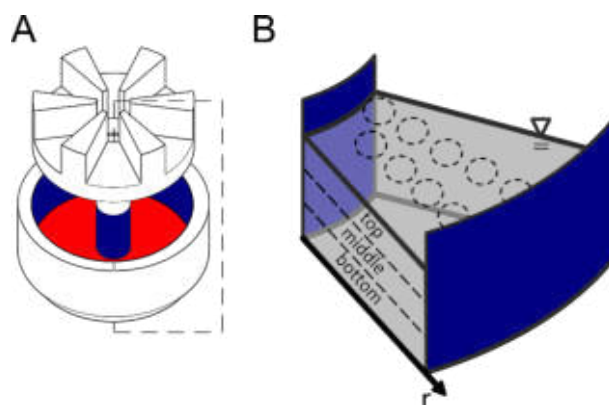
Figure 6.1: Freeze-thaw scale down model. **A:** an exploded view of the device with two cooling walls in blue. The inlay is used to reduce boundary freezing from the bottom and for volume reduction. The bottom of the device is heated to further minimize freezing from the bottom. **B**: a single chamber with sample layers and drill holes in the bulk volume as indicated by the dashed cross-section in A. Images were adapted from Weber et al. [120].

To reduce boundary conditions, an additional cooling circuit heats the wedge from the bottom at a constant temperature of 0 °C. The detailed process and thermal process behavior are described thoroughly in a previous study on the characterization of freezing processes [120].

All freezing experiments were performed in triplicates using three separated freezing chambers to account for process variation and assure reproducibility. 75 mL CCS prepared as described above was pipetted into each chamber. Then, the device was tempered at 5 °C for at least 1 h for temperature equilibration throughout the system and the sample bulk. After temperature equilibration, freezing was initiated by

lowering the cooling fluid temperature at maximum cooling rate to -60 to -20 °C. The final temperature was held for at least 5 h or overnight.

A core drill with 8 mm inner diameter from Buerkle (Bad Bellingen, Germany) was used for sampling from the frozen bulk. A 3D-printed lid was put on top of a chamber to assure reproducible sampling at three levels of 8 mm at nine locations with equal radial distances from each other as shown in Figure 6.1B. In preliminary experiments, radial freeze concentration was found negligible. Thus, samples were taken from two neighboring rows providing an increased number of overlapping samples volumes for improved data resolution. Afterwards, the frozen bulk was thawed by increasing the cooling fluid temperature to 25 °C for 1.5 h before homogenization and final liquid sampling using a 5 mL pipette.

If a subsequent protein A capture step was performed, no frozen samples were taken. In this case, the device temperature was lowered to 5 °C after thawing to reduce protein degradation while each replicate from a separate chamber was processed resulting in three separate protein A runs per freezing temperature. Therefore, samples were kept inside the cooled freezing device for up to 7 h at 5 °C.

6.2.4. mAb capturing

The mAb was captured from CCS using protein A affinity chromatography. MabSelect Sure was packed and operated with an ÄKTApurifier system (Cytiva, Illinois, Chicago, USA). UV extinction at 280 nm, pH, and conductivity were measured throughout the purification. An Omnifit column with 10 mm inner diameter from Omnifit Ltd. (Cambridge, UK) was used as column housing. The column was repacked throughout the experiments with column heights ranging from 188 to 203 mm resulting in a column volume (CV) of 14.7 to 15.9 mL. 65 mL samples with a titer of approximately 2-3 g/L mAb were loaded onto the column. As the manufacturer states a dynamic binding capacity of 35 g/mL resin, the column was operated well below its maximum capacity. The chromatography was conducted at a constant flow rate of 300 cm/h with PBS, pH 7.4 as equilibration and post-loading wash buffer. 25 mM NaAc, pH 5 has been applied as a second wash followed by an elution with 25 mM acetic acid, pH 3 until 2 CV after the end of fraction collection. Product was collected in 15 mL fractions starting from an extinction of 0.2 AU until stopped below 0.1 AU. Fraction collection criteria were chosen based in recommendations by the harvest supplier. Detailed chromatography conditions are listed in the supplementary material Table 6.2.

6.2.5. Filtration analysis

In general, as some systems showed a high turbidity, 0.2 µm filtration was performed in between every freeze-thaw and chromatography step to avoid clogging of the protein

A capturing columns. A filtration cascade using syringe filters with 1.2, 0.45, and 0.2 µm cut-off from Sartorius (Göttingen, Germany) was performed to investigate the size range of the particles present. The flow-through was analyzed for particles as described below.

Furthermore, the filter cake retained after a filtration step was investigated to measure the loss of mAb and HCP through filtration post freezing and thawing. Therefore, Vivaspin 2 filters with a 0.2 µm cut-off PES membrane from Sartorius (Göttingen, Germany) were loaded with a sample volume V_{load} of 2 to 4 mL and centrifuged at 1200 G. In preliminary experiments, 20 mL could be loaded onto the filter until filter clogging occurred. To reduce the influence of membrane fouling with increasing load volume, maximum load volumes of 4 mL were applied. After filtration, the filter membrane was detached from the housing, transferred into 500 µL centrifugation tubes and incubated with 500 µL $V_{dissolve}$ SEC-HPLC running buffer at 700 rpm and 5 °C in a thermomixer comfort from Eppendorf (Hamburg, Germany) overnight to dissolve any retained aggregates. As the filter membrane contained solution in the membrane pores after centrifugation, the measured protein concentration $c_{dissolve}$ in the dissolution buffer was composed of the dissolved filtered particles and the protein concentration from the filtered solution remaining in the filter. Thus, a mass balance over different load volumes V_{load} was used to calculate the aggregate concentration $c_{aggregate}$ in the analyzed sample. The subtraction of mass balances with different load volumes eradicates the influence of the remaining solution in the pores and leads to equation 6-I,

$$c_{aggregate} = V_{dissolve}\frac{\Delta c_{dissolve}}{\Delta V_{load}} = V_{dissolve}\,m \qquad\qquad \text{6-I}$$

where m is the slope of a linear regression of $c_{dissolved}$ over V_{load}. Protein concentrations were determined by capillary electrophoresis, HPLC, and SEC as described below. As proteins tend to adsorb to the filter membrane, the flow-through was re-filtered in a separate experiment for comparison.

6.2.6. Analytics

As this study aims to mimic typical process development conditions, analytics have been carefully chosen with respect to their application in industry. The most commonly used analytics involve enzyme-linked immunosorbent assay (ELISA) to quantify host-cell proteins (HCP) [149], size-exclusion high-performance liquid chromatography (SEC) for quantification of mAb monomers and aggregates and SDS-PAGE for protein size detection and quantification for low concentrated HCPs. While the analytics partially provide redundant data, comparability of redundant results is not always given due to lower limits of detection of the used methods. Additionally,

the optical density of solutions can be correlated with the particle number of non-filtered samples. Statistical significance was analyzed using a paired-sample t-test.

HCP quantification

The automated CHO HCP ELISA Gyrolab Bioaffy 1000HC with Gyrolab CHO HCP Kit 1 by Gyros Protein Technologies AB (Uppsala, Sweden) has been used for HCP analysis. The assays have been performed according to the supplied manual with reagents and buffers from Gyros Protein Technologies AB (Uppsala, Sweden). CCS and post-capture samples have been diluted 1:1000 and 1:10, respectively.

Protein size analysis

Proteins have been classified and quantified using an automated denaturing capillary electrophoresis. The Protein Express Assay LabChip together with the Caliper LabChip GX II by PerkinElmer (Massachusetts, USA) were operated according to the manual. All samples have been diluted 1:2 with ultrapure water (PURELAB Ultra, ELGA LabWater, Veolia Water Technologies, Saint-Maurice, France) before denaturing conditions were induced by adding 24.5 µL of 1 M dithiothreitol (DTT) at 100 °C for 5 min. For the analysis, proteins measured with approximately 30 and 60 kDa were regarded as light and heavy chains of the mAb, and the mAb concentration was calculated from the sum of the mentioned concentrations. It was further assumed that the detected HCPs did not possess a quaternary structure.

Large particles analysis

The optical density was used as an indicator for large aggregates in non-filtered samples. Therefore, 400 µL sample were pipetted into a cuvette with 1 cm path length, and the extinction at 600 nm wavelength was measured in a photometer infinite 200 by Tecan (Männedorf, Switzerland).

mAb monomer and aggregate analysis

SEC-HPLC was performed using a mAb specific TSKgel SuperSW mAb htp column by Tosoh Bioscience (Griesheim, Germany) with a 0.45 µm pre-column filter. The chromatography was performed on the HPLC UltiMate 3000 by Thermo Fisher Scientific (Massachusetts, USA) equipped with a diode-array detector and a cooled auto-sampler. Each analysis was operated at 0.35 mL/min for 9.5 min with a running buffer consisting of 100 mM sodium phosphate, 250 mM NaCl at pH 7. 200 µL samples were pipetted into a 0.45 µm filter plate, centrifuged into a micro-plate before covering with aluminum foil and placement into the cooled auto-sampler compartment, where 20 µL sample were injected onto the column for analysis. A baseline shift was observed when analyzing CCS. Therefore, CCS was spiked with concentrated post-capture material at different concentrations to evaluate accuracy of the assay. Furthermore,

mAb aggregates have only been calculated, if SEC-HPLC led to a baseline separation of the peaks of interest. Beside the protein main absorption peak at 280 nm wavelength, the absorption ratio A260/A280 was used to evaluated the presence of DNA, which has an absorption peak at 260 nm.

Protein concentration

The mAb concentration in post-capture samples was measured with Nanodrop 2000c by Thermo Fisher Scientific (Massachusetts, USA). Assuming a negligible HCP content, UV absorption was measured at 280 nm and protein concentration was calculated with an extinction coefficient of 1.5 g L^{-1} cm^{-1}.

6.3. Results

6.3.1. mAb concentration from CCS using SEC-HPLC

The quantification of mAb monomer and dimer was done using SEC-HPLC similarly to Paul et al. [150]. Spiking of the CCS with concentrated mAb was performed to validate the determination of mAb concentrations from absorption areas of SEC-HPLC chromatograms.
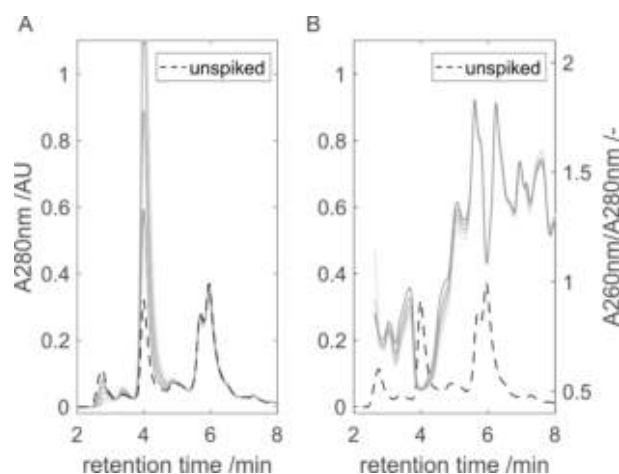
Figure 6.2: Size exclusion chromatogram of CCS spiked with concentrated mAb. **A:** Absorption at 280 nm (A280nm) of spiked samples over retention time. The absorption is capped at 1.1 AU for visualization although monomer absorption exceeds the limit. **B:** Absorption ratio calculated from absorption at 260 nm (A260nm) divided by absorption at 280 nm. Data prior to 2.5 min retention time is not shown due to low signal-to-noise ratios. In both figures, the dashed line shows the absorption at 280 nm of the unspiked sample on the left y-axis. Spike concentrations increase from dark to light from 1.8 to 10.0 g/L, respectively.

As shown in Figure 6.2A, the reference un-spiked sample showed a monomer peak after 4.0 min and a dimer peak after 3.4 min retention time. Numerous individual HCPs eluted after the monomer peak which could not be detected by SEC-HPLC in

the Protein A eluate (data not shown). The monomer and dimer absorption area at 280 nm increased with spike concentrations from 1.8 to 10.0 g/L. In contrast, the peak area after 2.7 min decreased with increasing spike concentration. Despite the fact that SEC-HPLC analysis did not lead to a baseline separation at the proteins of interest, a linear correlation between the monomer area and concentration was found with a coefficient of determination (R^2) of 0.9929 at a constant baseline at the global minimum. However, this correlation was only used for similar samples due to variances in the baseline shift that is expected to occur for varying contaminant concentrations. Figure 6.2B shows the absorption ratio A260/A280 of the samples. Data prior to 2.5 min retention time is not shown due to low signal-to- noise ratios. From 2.8 to 5.3 min retention time, the A260/A280 ratio decreases with increasing mAb concentration. For samples taken during elution of the mAb monomer from protein A, all ratios approach a minimum of 0.51. In comparison, a purified mAb sample approached a lower minimum A260/A280 ratio of 0.50.

6.3.2. Freeze concentration profiles

The macroscopic freeze concentration in frozen bulks was investigated at freezing temperatures from -20 to -60 °C. The mAb monomer concentrations c_{mab} relative to their initial concentration $c_{mab,0}$ are shown in Figure 6.3A over the cross-section of a freezing chamber at three individual layers. In Figure 6.3B, interpolated absolute concentrations are shown after freezing at -20 °C.
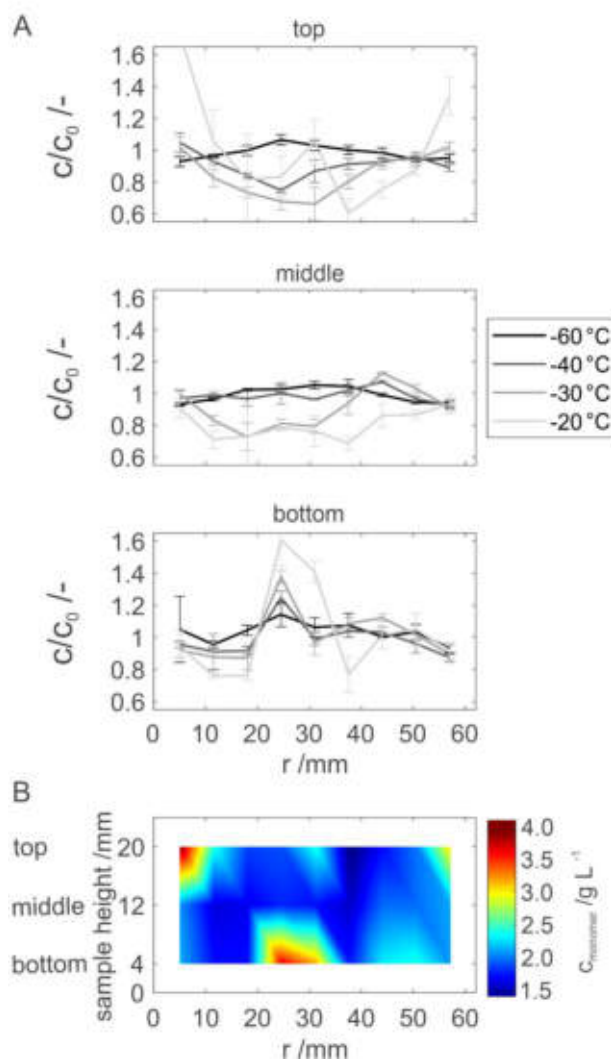
Figure 6.3: Concentration (c) profiles of mAb at different temperatures over the distance from the inner cooling wall (r). **A:** measured concentrations normalized by initial concentrations at the bottom, center, and top layers at 4, 12, and 20 mm above the bottom. The freezing temperatures rise with the gradient from dark to light from -60 to -20 °C. **B:** mAb concentration of a cross-section as a contour map after freezing at   -20 °C. Data is interpolated in between measured samples and the whole bulk volume is displayed. Data extrapolation to the boundaries has been avoided.

In general, the bulk was more homogeneous with lower freezing temperatures and resulting freezing times. While relative concentrations (c/c_0) varied from 0.61 to 1.60-fold at a freezing temperature of -20 °C, the concentrations after freezing at -60 °C varied only from 0.91 to 1.06-fold. The highest concentration was found just left of the bottom center at all freezing temperatures, whereas the lowest concentration was found in the top layer for all experiments except when freezing at -60 °C. The point of highest concentration matched the expected 'last point to freeze' determined in a previous study [120]. The concentration differences from the bottom

to top layer at $r = 25$ mm ($\Delta c = c_{b,25mm} - c_{t,25mm}$) from the inner cooling wall are 0.2, 1.1, 1.6, and 1.8 g/L at -60, -40, -30, and -20 °C. When freezing at -60 °C, the concentration increased towards the last point to freeze at $r = 25$ mm across all layers. At elevated freezing temperatures, however, the bulk concentration decreased towards the center in the top and middle layers. Higher freezing temperatures led to lower concentrations in the middle layer. In the top layer, a similar trend was found, except at the highest temperature of -20 °C. Furthermore, with higher freezing temperatures, a local maximum in the bottom layer was found between the outer larger cooling wall and the global maximum. Finally, the average standard deviations from triplicates increase with freezing temperatures resulting in $\sigma_{-60°C} = 3.5$ %, $\sigma_{-40°C} = 3.5$ %, $\sigma_{-30°C} = 4.9$ %, and $\sigma_{-20°C} = 9.1$ %. The mean relative freeze concentration over all samples was calculated for each freezing temperature to show the accuracy of the method by a volume averaged mass balance. A closed mass balance would result in an average freeze concentration of 100 %. Average freeze concentration decreased from 100 ± 5.5 % to 96 ± 9.0 % to 92 ± 15.6 % to 94 ± 27.7 % for freezing temperatures of -60 °C, -40 °C, -30 °C and -20 °C, respectively.

6.3.3. Protein size-dependent freeze concentration

In Figure 6.4A, freeze-concentrated proteins in the bottom layer after freezing at -30 °C are depicted. A freezing temperature of -30 °C was selected exemplarily as it led to a medium freeze concentration. The freeze concentration (c/c_0) of individual proteins has been measured by capillary electrophoresis. Freeze concentrations of up to 1.46 ± 0.08-fold for mAb were measured, which agrees with the measurements by SEC-HPLC reporting 1.38 ± 0.04-fold. For smaller HCP proteins, much higher freeze concentrations were detected such as 1.74 and 4.04-fold on average for proteins between 20 and 40 kDa and proteins smaller than 20 kDa, respectively. In the areas close to the cooling walls and at the local center minimum, the differences between the freeze concentration of small and large proteins were smaller. In the top layer right above the maximum freeze concentration, a relative mAb concentration of 35 % was found in contrast to 52 % for proteins between 20 and 40 kDa. When comparing the freeze concentration of small proteins to mAb as shown in Figure 6.4B, it was observed that small proteins show a high freeze concentration at the bottom and lower freeze concentration in the top layer. Thus, a separation of proteins as a function of size occurred. As shown in Figure 6.4C, the protein size correlates with the freeze concentration of the individual protein at bottom center with the highest concentration. Protein diffusivity increases with decreasing size and is thus suggested as a reason for the correlation. Under the assumption of spherical protein folding, the Einstein-Stokes equation can be used to calculate the diffusion coefficient D of

spherical particles with radius R and volume V by $D = \frac{k_B T}{6 \pi \eta R}$, where k_b is the Boltzmann constant, T the absolute temperature, and η is the viscosity. As the protein radius is proportional to the protein mass with $r \sim m^{1/3}$ [134], a data fit to $\frac{C}{C_0} = \frac{a}{m^{\frac{1}{3}}} + b$ resulted in an RMSE of 24.2 % and R^2 of 0.634, where a and b are fitted parameters. The parameter a accounts for the constant parameters in the Einstein-Stokes equation and b is necessary because of the minimal freeze concentration of all solutes.
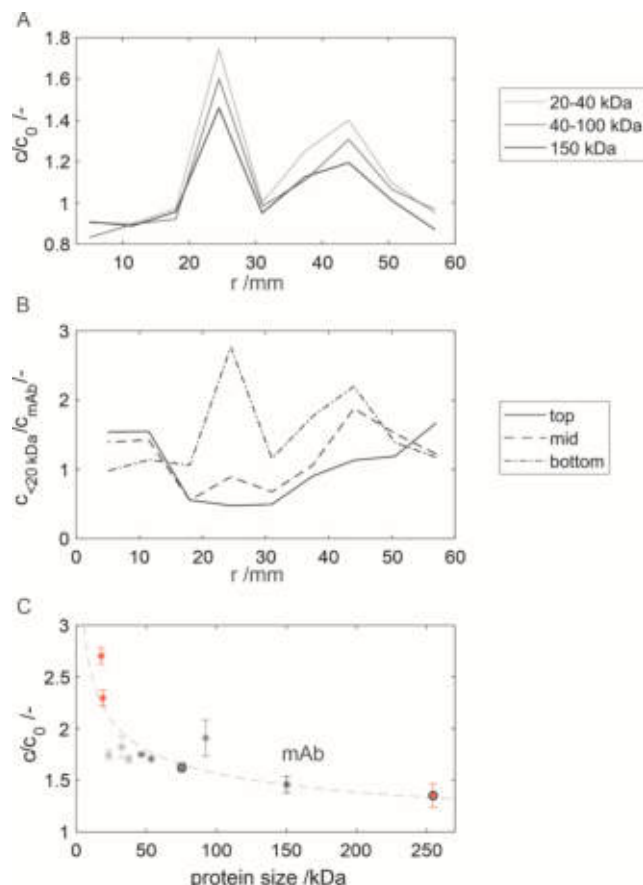
Figure 6.4: Protein size dependent freeze concentration measured by capillary electrophoresis. **A:** Mean protein concentrations (c) normalized by initial concentrations over the distance from the inner cooling wall (r) in the bottom layer. The harvest was frozen at -30 °C in triplicates and proteins are grouped by size in kDa. **B:** Freeze concentration of proteins smaller than 20 kDa normalized by the mAb concentration in the three sample layers. **C:** Freeze concentration at the point of highest concentration is plotted for all proteins over their respective sizes. If data points are circled, one outlier has been removed. Data was fitted to y=a/x$^{1/3}$+b. The color scheme in A and C is the same, and red data points in C are not shown in A.

6.3.4. Filtration analysis of thawed mAb CCS

After freezing and thawing of CCS, sometimes high turbidities can usually be observed visually. When thawed CCS was filtered using a filter cascade of decreasing pore size, the turbidity gradually decreased as shown in Table 6.1.

Table 6.1: Turbidity reduction with filtration cascade

Filter pore size /µm	Turbidity /mAu	Turbidity reduction /mAu (% of total)
Non-filtered	72.7 ± 0.75	n.a.
1.2	62.9 ± 0.25	9.8 (65.8 %)
0.45	61.5	1.4 (9.4 %)
0.2	57.8 ± 0.33	3.7 (24.8 %)

The majority of the filtered particles (66 %) was bigger in size than 1.2 µm, whereas 24.8 % had a size between 0.2 and 0.45 µm. Hence, 0.2 µm filtration prior to chromatography steps is necessary to avoid clogging of the columns. It has to be noted that several pre-syringe filters had to be used after freezing due to the large number of particles blocking the filter pores. This poses the question as to whether product is lost during filtration and critical quality attributes are changed. In order to analyze the particles filtered from a solution, a redissolution step of the retentate was performed. After a centrifugal filtration step, the membrane remains wet with soluble proteins in the retained solution. This leads to incorrect concentration measurements when incubating the filter membranes in redissolution buffer. Therefore, it is necessary to filter different filtration volumes, which is shown in Figure 6.5A, with exemplary raw data of replicates from individual freezing experiments.
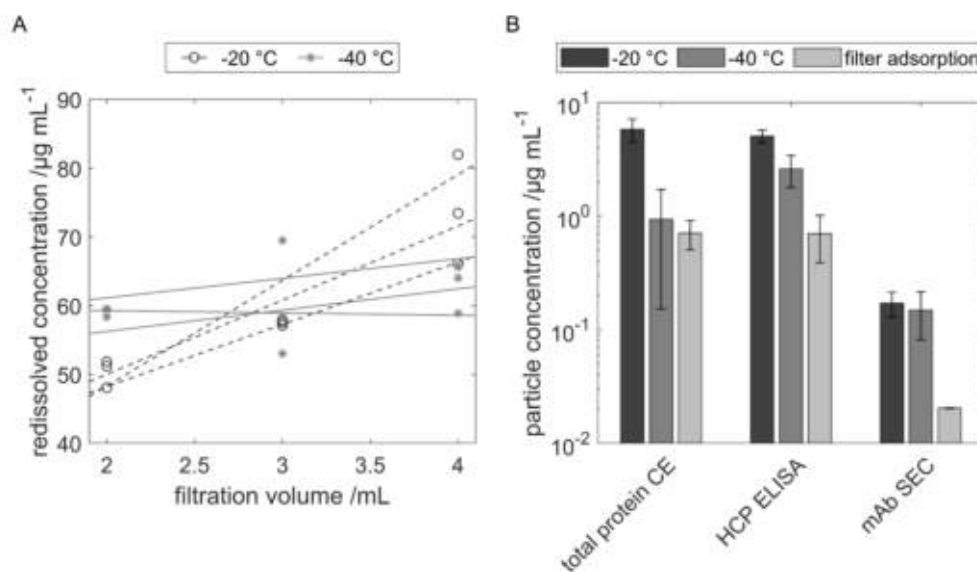
Figure 6.5: Retained proteins on a 0.2 μm filter. **A:** Exemplary raw data from triplicates with their respective linear regressions. The total, redissolved protein concentration measured by capillary electrophoresis (CE) at -20 and -40 °C is shown. Regression slopes from -40 and -20 °C in solid and dashed lines, respectively, are significantly different (p=0.04) and used to calculate the initial particle concentration. **B:** Particle concentrations of the total protein amount, host cell proteins (HCP) and mAb. A log-scale y-axis is shown. Protein adsorption to the filter is displayed for comparison.

Under the assumption of negligible membrane fouling, the redissolved protein concentration c_{dissolve} should be proportional to the volume filtered V_{load}. Thus, a linear regression was performed for each experiment. This regression reduces measurement errors occurring due to standard deviations and membrane variation. Additionally, the concentration contribution of the solution retained in the membrane pores can be calculated from the y-axis intercept. When comparing the re-dissolved protein concentrations from CCS frozen at -40 °C and -20 °C, the regression slopes decrease from 11.7 to 1.9 µg mL^{-1} mL^{-1} (µg Protein per mL V_{dissolve} and mL V_{load}) with statistical significance (p = 0.04). The particle concentrations calculated from the slopes are displayed in Figure 6.5B. More particles containing mAb and HCP are filtered on average when the solution is frozen at -20 °C. While the concentration of the total protein content and the HCP in the particles could be reduced when lowering the freezing temperature to -40 °C, the measured mAb concentration did not change significantly. Only a minor reduction in dimer shares when decreasing the freezing temperature was found on average. Adsorption of the proteins to the filter membrane did occur, but on average, it was always below the smallest concentration measured.

The measured mAb concentration was approximately one order of magnitude lower than the concentration of HCP and total protein.

6.3.5. Capturing of freeze-thawed mAb CCS

CCS from CHO was frozen at -40 °C, -30 °C, and -20 °C to investigate the influence of freezing and thawing on critical quality attributes. As particles are formed post freeze-thaw steps, filtration is necessary to avoid column clogging. When measuring the mAb aggregate and HCP content post freeze-thaw and filtration, no significant changes were observed. HCP concentrations varied within $101 \pm 6\,\%$ and $117 \pm 6\,\%$ of the initial concentration without a trend regarding freezing temperature. The average initial HCP concentration was 1.45 g/L. The average mAb aggregate content post freeze-thaw varied from $105 \pm 2\,\%$ to $97 \pm 5\,\%$ of the initial value. Although no significant difference was found, mAb aggregate shares post freeze-thaw increased on average with lower temperatures. However, the freeze-thaw step and the applied freezing temperature affected the HCP and aggregate concentration in the protein A eluate as shown in Figure 6.6.
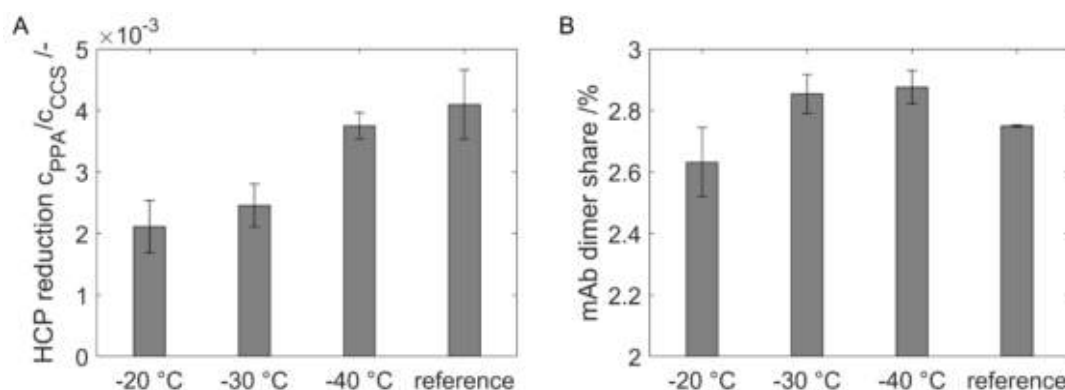
Figure 6.6: Analysis of post protein A (PPA) eluate. **A:** HCP reduction after protein A. Concentrations (c) measured by ELISA were normalized by the concentration in the cell culture supernatant (CCS). **B:** the dimer share PPA measured by SE-HPLC A280 area. Differences from -20 to -40 °C were significant in A for HCP recovery (p = 0.04) and in B for dimer shares (p = 0.03).

At lower freezing temperatures, the remaining HCP concentration was higher compared to the initial concentration. The remaining HCP concentration increased from $0.21 \pm 0.04\,\%$ to $0.37 \pm 0.02\,\%$ of the initial HCP concentration when lowering the temperature from -20 to -40 °C with significant difference (p = 0.04). In comparison, after capturing of mAb from the reference sample, almost twice as many HCPs $(0.41 \pm 0.06\,\%)$ were found in the eluate. Likewise, the mAb aggregate content after freezing at -20 °C and capturing was 2.63 % and increased to 2.87 % on average after freezing at -40 °C with significant difference (p = 0.03). When compared to a reference

mAb sample with aggregate shares of 2.75 %, elevated freezing temperatures reduced the aggregate shares, whereas colder freezing temperatures lead to increased aggregate shares.

6.4. Discussion

6.4.1. Correlation of mAb concentration to peak area

As shown in Figure 6.2, SEC-HPLC does not lead to baseline separation of the monomer and dimer peaks at 3.4 and 4.0 min, respectively. Analysis of a flow-through sample from a protein A load step with the majority of mAb removed revealed that a valley-to-valley baseline correction approaches the background noise of a CCS sample. Therefore, sample preparation prior to SEC-HPLC is often suggested [151] to avoid co-elution of CCS contaminants. Alternatively, precise monomer and dimer quantification from crude CCS samples requires intense background correction of the spectra. In our case, a valley-to-valley baseline correction marginally improved our concentration prediction model from $R^2 = 0.9929$ to 0.9934, which is in the range of the analysis by Dunn et al. [151] who reported R^2 of 0.9961. However, this model can only be applied under similar background conditions and is expected to perform worse at low concentrations. Additionally, the absorption ratio A260/A280 reveals further model restrictions. As DNA has its absorption maximum at 260 nm, a decrease of the signal indicates either less DNA or a higher protein concentration. Generally, the A260/A280 ratio decreased with increasing spike concentrations except at the elution of the monomer. Therefore, we conclude that DNA in the CCS tends to stick to mAb monomers, which in turn may increase the apparent absorption at 280 nm with increasing mAb concentration. Due to the discussed model uncertainties, a baseline fixed to the global minimum to quantify monomer concentrations from CCS was found sufficient for the scope of this work. The analyzed samples share the same origin, and the background is expected to be similar. Unlike Paul et al. [150], our spiking experiments suggest that the peak area at 2.7 min is not entirely mAb aggregates, as the area decreased with increasing spike concentrations. Additionally, the columns' void volume is expected to be around 1 mL, where the first peak elutes. Therefore, aggregate shares should not be as high as 75 % in CCS as reported by Paul et al. [150].

6.4.2. Freeze concentration profile

Our finding of macroscopic freeze concentration for elevated freezing temperatures is a well- described phenomenon in slow freezing processes due to elevated temperatures or passive cooling [14], [15], [104]. Freeze concentration of up to 160 % agrees with findings by Webb et al. [19], who reported a relative BSA concentration of 130 % in a similar actively cooled setup. The concentration profile differences at low and high

freezing temperatures can be explained by natural convection. As freezing temperatures are lowered, freeze front velocities increase resulting in faster freezing processes. Higher partition coefficients, that describe the entrapment of solute in the frozen matrix at the freezing front, have been reported at faster freezing processes [16] leading to reduced freeze concentration. Due to density gradients at the ice front, natural convection occurs causing high concentrations in the bottom layer [18]. Recent simulations by Geraldes et al. [119] report velocities in the area of up to 1 mm/s when freezing at -10°C. Higher density gradients and slower freezing processes therefore promote an increased natural convection at high freezing temperatures. The CCS in this study contained different contaminants besides the mAb at 2 g/L such as media components and HCPs. These contaminants are also freeze-concentrated leading to a higher density gradient compared to a mAb solution at a similar concentration, such as final fill formulations. Under the assumption of comparable partition coefficients, natural convection will be more pronounced for denser bulk solutions. The increasing concentration towards the center across all layers at -60 °C indicates a possible reduction of natural convection at such low freezing temperatures. However, with the occurrence of natural convection, effects such as second local concentration maximum and increased overall standard deviations appear. Fluctuation might occur with convection, which in turn leads to higher standard deviations. Furthermore, the convection is not only dependent on the physical properties of the solution, but also on the crystal morphology at the ice front, as the crystal structure is a stochastic effect. The observed top layer outlier close to the cooling walls at -20 °C might be due to freeze concentrate pushed out of the center at the last point to freeze. After freezing was completed, the bulk surface showed a mountain-like shape. Therefore, samples above 22 mm height were discarded, except for the samples close to the cooling walls, where the bulk volume height did not exceed 22 mm. This was also described by Hauptmann et al. [14]. Increasing convection also led to larger inaccuracies of the sampling method. The mass balance did not close for the observed concentrations at elevated freezing temperatures.

6.4.3. Natural convection amplifies solute separation by diffusion

Looking at the freeze concentration of differently sized proteins shown in Figure 6.4C, a correlation between freeze concentration and protein size can be found, where smaller proteins tend to freeze and concentrate more at the center bottom of a container. However, the relation between protein size and freeze concentration was only found when freeze concentration effects were high at the bottom of the freezing container. At points of lower freeze concentration at the bottom, the freeze concentration of different proteins was less significant. Fitting of the freeze

concentration data at the point of highest concentration according to the correlation of diffusion to protein size, as shown in Figure 6.4C, revealed that protein diffusion might be an explanation. Besides diffusion, natural convection leads to an additional mass flux from the freeze concentrated areas at the freezing front towards the center bottom, where size dependent freeze concentration was most prominent. Natural convection is caused by density gradients due to freeze concentration and temperature differences leading to a convective layer in the gravitational direction at the freezing front [16], [68]. The convection induces a circular motion, dragging down the solutes to the bottom and along the bottom of the freezing container in front of the freezing boundary, where it settles due to the higher density. Meanwhile, non-concentrated liquid from the center is transported to the freezing boundary, reducing the entrapped solute concentration and thus increasing inhomogeneity in the frozen bulk. On the one hand, natural convection is promoted by high concentration gradients leading to faster velocities at the freezing boundary. On the other hand, the convection at the freezing front is inhibited by crystallization such as dendritic ice formation [71]. The density anomaly of water adds additional complexity to the mechanism. This complex behavior has been modeled [98], [119] using the enthalpy-porosity method and the Carman-Kozeny equation to describe velocity through porous media [152]. Figure 6.7 schematically depicts liquid fraction, temperature, velocity in gravitational direction and concentration at the freezing front. Data are derived from numeric fluid simulation using velocity dumping method at the mushy zone according to a flow through porous media.

The convection velocity increases with solute concentration and liquid fraction, with the maximum velocity at the edge of the mushy zone. The solute concentration maximum is within the mushy zone, as the increasing velocity drags down the freeze concentrated liquid and bring less concentrated liquid from the top and center. For detailed description of the mechanistic processes involved, the Grashof number and Prandtl number could be analyzed in further studies. Simulations show flow profiles thick as several mm at the beginning, which become thinner and slower over time [119]. Smaller molecules with higher diffusivity might be able to diffuse further into the convective layer. Diffusive mass transport might be too slow for molecules to diffuse beyond the boundary layer. Hence, small proteins are exposed to faster drag velocities leading to a higher bottom freeze concentration. Experimental studies of flow profiles during solidification processes show the importance of such flow profiles [100], which was also investigated by Geraldes et al. [119], who simulated the effect of varying mushy zone porosities.
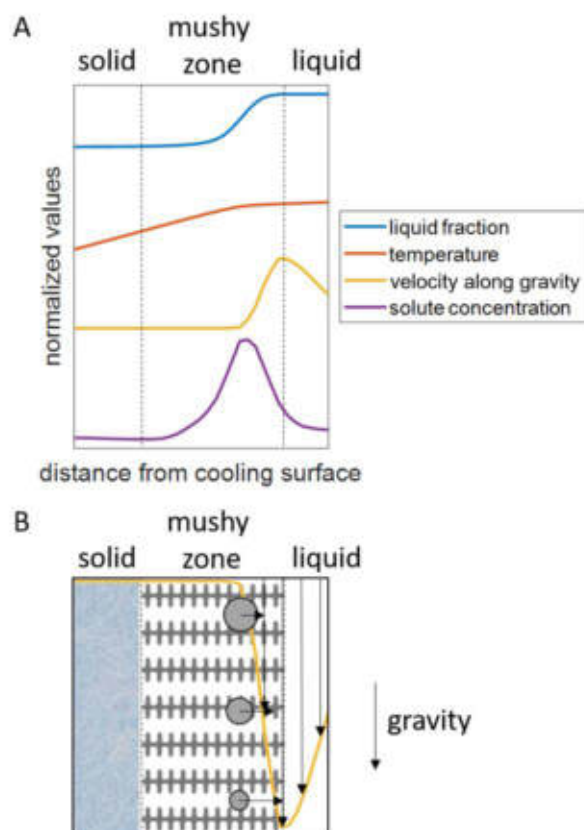
Figure 6.7: Schematic representation of mass transport at the freezing front. **A:** normalized values for liquid fraction, temperature, gravitational velocity and solute concentration. Values originate from CFD simulation with enthalpy porosity method. **B:** schematic representation of the diffusion of three differently sized proteins shown as circles. The velocity profile of A in direction of gravity is shown and arrow length indicates the driving force.

Furthermore, the hypothesis is supported by an early study on freeze concentration, where buffer components were freeze-concentrated whereas the lactose dehydrogenase concentration was equal across the frozen bulk [153]. Other studies have not found significant differences when comparing stabilizing formulation agents such as small buffer molecules and proteins like Roessl et al. [106], who evaluated freeze concentration in an actively cooled small-scale model. The presumably low height of the container might have reduced natural convection and therefore minimized diffusion-based freeze concentration. The results by Kohle et al. [15] show the mAb aggregate freeze concentration to be similar to that of the monomer, which can be explained by the minor variation in the diffusion coefficient, because of the relative large size of the proteins, which is above 150 kDa.

6.4.4. Freeze-thaw of CCS leads to temperature-dependent formation of particles containing mAb and HCP

If the CCS was frozen, particles were formed during the freeze-thaw step, that consist of both mAb and HCP as shown in Figure 6.5B. On average, all analytics show a reduction in particle formation with decreasing freezing temperature. As lower freezing temperatures lead to faster freezing processes, they induce less freeze stress and therefore reduce the rate of aggregation [37]. Furthermore, lower freezing temperatures lead to reduced freeze concentration as discussed before. Such particle formation might be induced by CHO HCPs such as protease cathepsin D [154] and thus, should be separated from the product as soon as possible. Furthermore, mAbs also form native aggregates under freeze-thaw stress [148].

The relatively low mAb concentration in the dissolution buffer can be explained by the presence of particles in the dissolution buffer. While ELISA and capillary electrophoresis are able to handle non-soluble particles by dilution, wash steps or denaturation, HPLC methods require sample filtration and the use of a pre-column filter. Furthermore, ELISA and capillary electrophoresis are sensitive methods whereas the HPLC operates at the lower limit of the detection and is affected by model limitations as discussed earlier leading to relatively high standard deviations. Finally, capillary electrophoresis indicated a lower total protein concentration after -40 °C freeze-thaw than the measured HCP concentration.

Protein adsorption to filtration membranes is a common issue [155] and therefore has to be accounted for at such low concentration levels. The occurring membrane adsorption was lower than the measured particle concentration and thus can be interpreted as the background noise.

6.4.5. Freezing influences critical quality attributes of mAb capturing

If CCS from CHO cells is frozen prior to capturing, significant changes in HCP and aggregate shares can be expected in the protein A eluate as depicted in Figure 6.6. HCP levels in the eluate are generally lower after a freeze-thaw step followed by a necessary filtration compared to a reference sample. At first glance, the HCP concentration might be generally decreased by the particle removal, leading to an overall reduction of HCP in the protein A load and subsequently the eluate. However, the HCP content from an aliquot, after the freeze-thaw step and after filtration did not change significantly. Thus, a hypothesis is suggested, where the changes in the protein A eluate may arise from specific HCPs with high mAb affinity due to protein interactions. Looking at mAb capturing processes, HCP co-elution with mAb from protein A occurs due to protein interactions between HCPs and the mAb-protein A

complex [154], [156], [157]. Hence, co-eluting HCPs show increased affinity towards mAbs. If freeze-thaw stress is exerted on the CCS, the stress favors particle formation of these particular high-affinity HCPs and the mAb because of their affinity. As discussed earlier, warmer freezing temperatures exert stronger freeze stress causing increased particle formation. These particles contain small amounts of mAb and high-affinity HCPs that are removed before the protein A capturing. As a result, freezing and subsequent filtration of CCS decrease the HCP concentration in protein A eluate. Furthermore, the freeze-thaw step induces mAb aggregation leading to higher aggregate shares [148]. As a result, slightly stressed and fast-frozen samples at -40 °C show higher dimer shares compared to reference protein A eluate. However, the soluble dimer aggregates might form insoluble oligomers that are removed by a filtration step. As higher freeze-thaw stress is applied at warmer freezing temperatures, larger particles are formed [158], which might be caused by higher concentrations [159]. Hence, the protein A eluate from freezing steps with warmer freezing temperatures show reduced aggregate shares compared to faster frozen samples. Unfortunately, soluble dimer shares are determined by HPLC and thus, mAb aggregate shares directly after freeze-thaw steps cannot be determined without prior filtration.

6.5. Conclusion

This study highlights the effect of freezing temperature with regards to particle formation of mAb CCS. Freezing reduced the number of HCPs present in the protein A eluate, which demonstrates the importance of the careful characterization of freezing processes in current platform process development. Furthermore, increased levels of mAb dimers with slower freezing processes were shown. Our results suggest particle formation of mAb and co-eluting HCPs with mAb affinity. In subsequent studies, the hypothesis of the co-eluting HCPs could further be examined by proteomics.

Furthermore, the study provides in-depth process understanding of freezing mechanisms involving complex multicomponent media. Solute diffusion in the mushy zone is suggested as an explanation of freeze concentration dependency on protein size. The complex interplay of diffusion and convection should be further evaluated in mechanistic studies, such as computational fluid dynamics, to improve the process understanding.

6.6. Acknowledgments

6.7. Supplementary material

Table 6.2 Protein A purification conditions

Phase	Buffer	Duration
Equilibration	PBS, pH 7.4	3 CV
Load	CCS	65 mL
Wash 1	PBS, pH 7.4	3 CV
Wash 2	25 mM Sodium Acetate, pH 5	3 CV
Elution	25 mM Acetic Acid, pH 3	2 CV post UV < 100 mA
Strip	500 mM Acetic Acid	2 CV
Neutralization	ddH$_2$O	2 CV
Sterilization	100 mM NaOH	15 min
Re-equilibration	PBS, pH 7.4	10 CV

7

Conclusion and outlook

In the presented work, insights into biopharmaceutical freezing processes were given by investigation of freeze concentration. The importance of mass transport phenomena in freezing processes was investigated by novel process analytical technology (PAT), in-silico models and case-studies in a small-scale model. The improved process understanding enables freezing process optimization during development and thus contributes to the Quality-by-Design (QbD) approach. Furthermore, the potentials of a small-scale freezing model and in-silico descriptions were investigated using the proposed PAT.

In the first part of this thesis (Chapter 3), a small-scale model for freeze-thaw experiments was established and investigated. The freezing time was identified as a critical process parameter, which allows for comparison of different freezing processes. With increasing freezing time, the freeze concentration was found to increase. A temperature probe array was used as a novel PAT for freeze progression monitoring. The setup overcame common challenges such as freezing point detection and improved the accuracy of freezing time determination. Freeze progression monitoring enabled the detection of the position the last point to freeze (LPTF), which shifted depending on the applied freezing temperature. In addition, the applicability of the Plank equation for freezing time prediction was investigated in actively cooled freezing processes. Limitations of freezing time reduction by the cooling equipment were shown, which may have a major impact on fast freezing processes.

The CPP freezing time affects the critical quality attribute (CQA) freeze concentration in the frozen bulk. In addition to measuring the CPP, a PAT for real-time monitoring of the CQA freeze concentration is presented in Chapter 4. Therefore, Raman spectroscopy in conjunction with partial least squares (PLS) regression was used to quantify up to three solutes simultaneously in the freezing container. Upon validation of the method, the impact of freezing time on freeze concentration was confirmed.

Furthermore, the additive concentration had a major impact on the freeze concentration. The separation of solutes was shown during the freeze concentration process indicating potential protein destabilization mechanisms in freezing process. Real-time monitoring in combination with flexibility of positioning of the probe reveals small convection currents at the bottom of the freezing container.

Using the generated transient data about freezing processes, a computational fluid dynamic (CFD) model was evaluated to predict freezing time and freeze concentration in Chapter 5. The freezing time was predicted successfully and the findings from Chapter 3 could be confirmed. The water density anomaly led to thermal convection referred to as hot and cold vertices, that might impact freeze concentration in slow freezing processes, especially when the fluid is directly frozen from room temperature. With the extension of the water simulation by a solute model, the freeze concentration was described qualitatively. The results were used to qualitatively improve the process understanding and substantiated the discussions in the other studies. However, due to discretization issues and numerical instability, the prediction of freeze concentration was dependent on physical and numerical parameters. A quantitative prediction of freeze concentration using the implemented enthalpy-porosity method was not successful, which questions the reliability of process prediction by models suggested in recent literature.

The impact of freezing time on mAb CQAs in frequently used platform processes was investigated by a case study presented in Chapter 6. While freezing is performed regularly during process development to overcome the short shelf life of process intermediates, the study highlights the importance of freezing evaluation. Long freezing times led to an increased reduction of contaminants in the protein A eluate after freezing. The contaminant removal was attributed to particle formation as a result of freeze concentration and subsequent filtration. Thus, processes that include an additional freeze-thaw cycle might not be comparable to non-frozen processing. Furthermore, the degree of freeze concentration of host cell proteins (HCP) was correlated with their size. Diffusion was suggested as a driver for freeze concentration, which confirms the previous findings.

Looking in to the future, the findings suggest, that freezing processes are an overlooked process in the biopharmaceutical industry. While a variety of options and scale down models are available, PAT should be implemented more often to further increase the process understanding of freezing phenomena, especially in complex multicomponent solutions and protein mixtures. Less expensive alternatives to Raman spectroscopy, such as conductivity measurements, could be investigated for large-scale manufacturing quality assurance. While this widely available method

could be used as a monitoring approach during production, it has drawbacks in selectivity when compared to Raman spectroscopy. Available in-silico CFD models for freezing processes provide qualitative process descriptions, but currently lack of the numerical stability to predict freeze concentration, yet. Improvements in discretization and the description of the liquid-solid transition are necessary to for further investigations. In future case studies, the influence of thawing should be investigated, as the gradients present in frozen bulks might lead to variable drug concentration after filling.

Bibliography

[1]   W. Cullen, "Of the Cold produced by evaporating fluids, and of some other Means of producing Cold," *Essays Obs. Phys. Lit. Read before a Soc. Edinburgh, Publ. by them*, vol. II, 1756.

[2]   G. Walsh, "Biopharmaceutical benchmarks 2018," *Nat. Biotechnol.*, vol. 36, no. 12, pp. 1136–1145, 2018.

[3]   L. Milane and M. Amiji, "Clinical approval of nanotechnology-based SARS-CoV-2 mRNA vaccines: impact on translational nanomedicine," *Drug Deliv. Transl. Res.*, 2021.

[4]   D. C. Malone *et al.*, "Cost-effectiveness analysis of using onasemnogene abeparvocec (AVXS-101) in spinal muscular atrophy type 1 patients," *J. Mark. Access Heal. Policy*, vol. 7, no. 1, p. 1601484, Jan. 2019.

[5]   N. Rathore and R. S. Rajan, "Current Perspectives on Stability of Protein Drug Products during Formulation, Fill and Finish Operations," *Biotechnol. Prog.*, vol. 24, no. 3, pp. 504–514, May 2008.

[6]   W. Wang, *Instability, stabilization, and formulation of liquid protein pharmaceuticals*, vol. 185, no. 2. 1999.

[7]   S. K. Singh and S. Nema, "Freezing and Thawing of Protein Solutions," *Formul. Process Dev. Strateg. Manuf. Biopharm.*, pp. 625–675, 2010.

[8]   D. J. A. Crommelin, T. J. Anchordoquy, D. B. Volkin, W. Jiskoot, and E. Mastrobattista, "Addressing the Cold Reality of mRNA Vaccine Stability," *J. Pharm. Sci.*, vol. 110, no. 3, pp. 997–1001, 2021.

[9]   P. Marks, "FDA In Brief: FDA Authorizes Longer Time for Refrigerator Storage of Thawed Pfizer-BioNTech COVID-19 Vaccine Prior to Dilution, Making Vaccine More Widely Available." [Online]. Available: https://www.fda.gov/news-events/press-announcements/fda-brief-fda-authorizes-longer-time-refrigerator-storage-thawed-pfizer-biontech-covid-19-vaccine. [Accessed: 27-May-2021].

[10]   K. G. Desai, W. Pruett, P. J. Martin, J. D. Colandene, and D. Nesta, "Impact of manufacturing-scale freeze-thaw conditions on a mAb solution," vol. 30, pp. 30–36, Jan. 2017.

[11]   U. Roessl, S. Humi, S. Leitgeb, and B. Nidetzky, "Design of experiments reveals critical parameters for pilot-scale freeze-and-thaw processing of L-lactic dehydrogenase," *Biotechnol. J.*, vol. 10, no. 9, pp. 1390–1399, 2015.

[12]   M. Puri, S. Morar-Mitrica, G. Crotts, and D. Nesta, "Evaluating freeze-thaw processes in biopharmaceutical development - Small-scale study designs," *Bioprocess Int.*, vol. 13, Jan. 2015.

[13]   W. J. Rayfield, S. Kandula, H. Khan, and N. Tugcu, "Impact of Freeze/Thaw Process on Drug Substance Storage of Therapeutics," *J. Pharm. Sci.*, vol. 106, no. 8, pp. 1944–1951, 2017.

[14]   A. Hauptmann, G. Hoelzl, and T. Loerting, "Distribution of Protein Content and Number of Aggregates in Monoclonal Antibody Formulation After Large-Scale Freezing," *AAPS PharmSciTech*, vol. 20, no. 2, pp. 1–11, 2019.

[15]   P. Kolhe and A. Badkar, "Protein and solute distribution in drug substance containers during frozen storage and post-thawing: A tool to understand and define freezing-thawing parameters in biotechnology process development," *Biotechnol. Prog.*, vol. 27, no. 2, pp. 494–504, 2011.

[16]   M. A. Rodrigues, M. A. Miller, M. A. Glass, S. K. Singh, and K. P. Johnston, "Effect of Freezing Rate and Dendritic Ice Formation on Concentration Profiles of Proteins Frozen in Cylindrical Vessels," *J. Pharm. Sci.*, vol. 100, no. 4, pp. 1316–1329, 2011.

[17]   U. T. Lashmar, M. Vanderburgh, and S. J. Little, "Bulk Freeze–Thawing of Macromolecules."

[18]   M. A. Rodrigues *et al.*, "The importance of heat flow direction for reproducible and homogeneous freezing of bulk protein solutions," *Biotechnol. Prog.*, vol. 29, no. 5, pp. 1212–1221, 2013.

[19]   S. D. Webb, J. N. Webb, T. G. Hughes, D. F. Sesin, and A. C. Kincaid, "Freezing bulk-scale biopharmaceuticals using common techniques - And the magnitude of freeze-concentration," *BioPharm*, vol. 15, no. 5, pp. 22–34, 2002.

[20]   R. Peraman, K. Bhadraya, and Y. Padmanabha Reddy, "Analytical Quality by Design: A Tool for Regulatory Flexibility and Robust Analytics," *Int. J. Anal. Chem.*, vol. 2015, p. 868727, 2015.

[21]   D. Roush *et al.*, "Toward in silico CMC: An industrial collaborative approach to model-based process development," *Biotechnol. Bioeng.*, vol. 117, no. 12, pp. 3986–4000, 2020.

[22]   M. E. Krause and E. Sahin, "Chemical and physical instabilities in manufacturing and storage of therapeutic proteins," *Curr. Opin. Biotechnol.*, vol. 60, pp. 159–167, 2019.

[23]   M. Vázquez-Rey and D. A. Lang, "Aggregates in monoclonal antibody manufacturing processes," *Biotechnol. Bioeng.*, vol. 108, no. 7, pp. 1494–1508, Jul. 2011.

[24]   D. A. Parkins and U. T. Lashmar, "The formulation of biopharmaceutical products," *Pharm. Sci. Technolo. Today*, vol. 3, no. 4, pp. 129–137, 2000.

[25]   K. Baumgartner *et al.*, "Determination of protein phase diagrams by microbatch experiments: Exploring the influence of precipitants and pH," *Int. J. Pharm.*, vol. 479, no. 1, pp. 28–40, Feb. 2015.

[26]   N. Rakel, K. C. Bauer, L. Galm, and J. Hubbuch, "From osmotic second virial coefficient (B22) to phase behavior of a monoclonal antibody," *Biotechnol. Prog.*, vol. 31, no. 2, pp. 438–451, 2015.

[27]   P. L. Privalov, "Cold denaturation of protein," *Crit. Rev. Biochem. Mol. Biol.*, vol. 25, no. 4, pp. 281–306, 1990.

[28]   B. S. Bhatnagar, R. H. Bogner, and M. J. Pikal, "Protein stability during freezing: Separation of stresses and mechanisms of protein stabilization," *Pharm. Dev. Technol.*, vol. 12, no. 5, pp. 505–523, 2007.

[29]   A. Twomey, K. Kurata, Y. Nagare, H. Takamatsu, and A. Aksan, "Microheterogeneity in frozen protein solutions," *Int. J. Pharm.*, vol. 487, no. 1–2, pp. 91–100, 2015.

[30]   G. Gómez, M. J. Pikal, and N. Rodríguez-Hornedo, "Effect of initial buffer composition on pH changes during far-from-equilibrium freezing of sodium phosphate buffer solutions.," *Pharm. Res.*, vol. 18, no. 1, pp. 90–97, Jan. 2001.

[31]   K. A. Pikal-Cleland, J. L. Cleland, T. J. Anchordoquy, and J. F. Carpenter, "Effect of Glycine on pH Changes and Protein Stability During Freeze–Thawing in Phosphate Buffer Systems," *J. Pharm. Sci.*, vol. 91, no. 9, pp. 1969–1979, 2002.

[32] K. Izutsu, S. Yoshioka, and T. Terao, "Effect of mannitol crystallinity on the stabilization of enzymes during freeze-drying.," *Chem. Pharm. Bull. (Tokyo).*, vol. 42, no. 1, pp. 5–8, Jan. 1994.

[33] M. E. Klijn, A. K. Wöll, and J. Hubbuch, "Apparent protein cloud point temperature determination using a low volume high - throughput cryogenic device in combination with automated imaging," *Bioprocess Biosyst. Eng.*, no. 0123456789, pp. 1–45, 2019.

[34] B. D. Mason, L. Zhang, R. L. Remmele, and J. Zhang, "Opalescence of an IgG2 monoclonal antibody solution as it relates to liquid–liquid phase separation," *J. Pharm. Sci.*, vol. 100, no. 11, pp. 4587–4596, 2011.

[35] B. S. Chang, B. S. Kendrick, and J. F. Carpenter, "Surface-Induced Denaturation of Proteins during Freezing and its Inhibition by Surfactants," *J. Pharm. Sci.*, vol. 85, no. 12, pp. 1325–1330, 1996.

[36] G. Assegehegn, E. Brito-de la Fuente, J. M. Franco, and C. Gallegos, "The Importance of Understanding the Freezing Step and Its Impact on Freeze-Drying Process Performance," *J. Pharm. Sci.*, vol. 108, no. 4, pp. 1378–1395, 2019.

[37] A. K. Wöll, M. Desombre, L. Enghauser, and J. Hubbuch, "A phase diagram-based toolbox to assess the impact of freeze/thaw ramps on the phase behavior of proteins," *Bioprocess Biosyst. Eng.*, no. 0123456789, 2019.

[38] A. A. Shukla, L. S. Wolfe, S. S. Mostafa, and C. Norman, "Evolving trends in mAb production processes," *Bioeng. Transl. Med.*, vol. 2, no. 1, pp. 58–69, 2017.

[39] A. Bezawada, M. Thompson, and W. Cui, "Use of blast freezers in vaccine manufacture," *Bioprocess Int.*, vol. 9, no. 9, pp. 42–51, 2011.

[40] E. S. Langer and R. A. Rader, "Single-use technologies in biopharmaceutical manufacturing: A 10-year review of trends and the future," *Eng. Life Sci.*, vol. 14, no. 3, pp. 238–243, 2014.

[41] R. W. Potter, M. A. Clynne, and D. L. Brown, "Freezing point depression of aqueous sodium chloride solutions," *Econ. Geol.*, vol. 73, no. 2, pp. 284–285, Apr. 1978.

[42] J. J. Schwegman, L. M. Hardwick, and M. J. Akers, "Practical Formulation and Process Development of Freeze-Dried Products," *Pharm. Dev. Technol.*, vol. 10, no. 2, pp. 151–173, Jan. 2005.

[43] Y. ROOS and M. KAREL, "Amorphous state and delayed ice formation in sucrose solutions," *Int. J. Food Sci. Technol.*, vol. 26, no. 6, pp. 553–566, Dec. 1991.

[44] F. E. Young and F. T. Jones, "Sucrose Hydrates. The Sucrose–Water Phase Diagram.," *J. Phys. Chem.*, vol. 53, no. 9, pp. 1334–1350, 1949.

[45] S. K. Pansare and S. M. Patel, "Practical Considerations for Determination of Glass Transition Temperature of a Maximally Freeze Concentrated Solution," *AAPS PharmSciTech*, vol. 17, no. 4, pp. 805–819, 2016.

[46] L. Chang *et al.*, "Mechanism of protein stabilization by sugars during freeze-drying and storage: Native structure preservation, specific interaction, and/or immobilization in a glassy matrix?," *J. Pharm. Sci.*, vol. 94, no. 7, pp. 1427–1444, 2005.

[47] D. Vitkup, D. Ringe, G. A. Petsko, and M. Karplus, "Solvent mobility and the protein 'glass' transition," *Nat. Struct. Biol.*, vol. 7, no. 1, pp. 34–38, 2000.

[48] G. A. Sacha and S. L. Nail, "Thermal analysis of frozen solutions: Multiple glass transitions in amorphous systems," *J. Pharm. Sci.*, vol. 98, no. 9, pp. 3397–3405, Sep. 2009.

[49] J. R. Authelin *et al.*, "Freezing of Biologicals Revisited: Scale, Stability, Excipients, and Degradation Stresses," *J. Pharm. Sci.*, vol. 109, no. 1, pp. 44–61, 2020.

[50] J. GENOTELLE, "EXPRESSION DE LA VISCOSITE DES SOLUTIONS SUCREES," 1978.

[51] M. Rampp, C. Buttersack, and H.-D. Lüdemann, "Self-Diffusion of Sucrose in Molasses," *Ind. Eng. Chem. Res.*, vol. 39, no. 11, pp. 4400–4407, Nov. 2000.

[52] M. Rampp, C. Buttersack, and H. D. Lüdemann, "c,T-dependence of the viscosity and the self-diffusion coefficients in some aqueous carbohydrate solutions," *Carbohydr. Res.*, vol. 328, no. 4, pp. 561–572, 2000.

[53] F. Schneider, A. Emmerich, D. Finke, and N. Panitz, "Untersuchungen uber die Diffusion in reinen und technischenSaccharoselosungen. I. Die Diffusion der Saccharose in reinen wassrigen Losungen." pp. 222–229, 1976.

[54] D. Girlich, H.-D. Lüdemann, C. Buttersack, and K. Buchholz, "c , T-Dependence of the Self Diffusion in Concentrated Aqueous Sucrose Solutions," *Zeitschrift für Naturforsch. C*, vol. 49, no. 3–4, pp. 258–264, 1994.

[55] R. Schiller, "The Stokes-Einstein law by macroscopic arguments," *Int. J. Radiat. Appl. Instrumentation. Part C. Radiat. Phys. Chem.*, vol. 37, no. 3, pp. 549–550, 1991.

[56] *Development and manufacture of drug substances (chemical entities and biotechnological/biological entities) Q11.* International conference on harmonisation of technical requirements for registration of pharmaceuticals for human use, 2012.

[57] S. Rambhatla, R. Ramot, C. Bhugra, and M. J. Pikal, "Heat and mass transfer scale-up issues during freeze drying: II. Control and characterization of the degree of supercooling," *AAPS PharmSciTech*, vol. 5, no. 4, pp. 54–62, 2004.

[58] G. John Morris and E. Acton, "Controlled ice nucleation in cryopreservation - A review," *Cryobiology*, vol. 66, no. 2, pp. 85–92, 2013.

[59] Q. T. Pham, "Extension to Planck's equation for predicting freezing times of foodstuffs of simple shapes," *Int. J. Refrig.*, vol. 7, no. 6, pp. 377–383, 1984.

[60] V. Alexiades and A. D. Solomon, *Mathematical Modeling Of Melting And Freezing Processes.* Washington: Taylor & Francis, 1993.

[61] O. Miyawaki, L. Liu, and K. Nakamura, "Effective partition constant of solute between ice and liquid phases in progressive freeze-concentration," *J. Food Sci.*, vol. 63, no. 5, pp. 756–758, 1998.

[62] M. D. Dupouy, D. Camel, and J. J. Favier, "Natural convection in directional dendritic solidification of metallic alloys-I. Macroscopic effects," *Acta Metall.*, vol. 37, no. 4, pp. 1143–1157, 1989.

[63] S. Ganesan and D. R. Poirier, "Solute redistribution in dendritic solidification with diffusion in the solid," *J. Cryst. Growth*, vol. 97, no. 3–4, pp. 851–859, 1989.

[64] M. F. Butler, "Freeze Concentration of Solutes at the Ice/Solution Interface Studied by Optical Interferometry," *Cryst. Growth Des.*, vol. 2, no. 6, pp. 541–548, 2002.

[65]   M. C. Schneider and C. Beckermann, "A numerical study of the combined effects of microsegregation, mushy zone permeability and flow, caused by volume contraction and thermosolutal convection, on macrosegregation and eutectic formation in binary alloy solidification," *Int. J. Heat Mass Transf.*, vol. 38, no. 18, pp. 3455–3473, 1995.

[66]   A. Fick, "Über Diffusion [Translated: (1995) 'On liquid diffusion'. Journal of Membrane Science]," *Poggendorff's Ann. der Phys. und Chemie*, vol. 94, no. 1, pp. 59–86, 1855.

[67]   K. P. Young and D. H. Kerkwood, "The dendrite arm spacings of aluminum-copper alloys solidified under steady-state conditions," *Metall. Trans. A*, vol. 6, no. 1, pp. 197–205, 1975.

[68]   M. Vynnycky and S. Kimura, "An analytical and numerical study of coupled transient natural convection and solidification in a rectangular enclosure," *Int. J. Heat Mass Transf.*, vol. 50, no. 25–26, pp. 5204–5214, 2007.

[69]   X. Wang and Y. Fautrelle, "An investigation of the influence of natural convection on tin solidification using a quasi two-dimensional experimental benchmark," *Int. J. Heat Mass Transf.*, vol. 52, no. 23–24, pp. 5624–5633, 2009.

[70]   K. G. Schmidt, *VDI Heat Atlas*. 2010.

[71]   M. A. Miller, M. A. Rodrigues, M. A. Glass, S. K. Singh, K. P. Johnston, and K. P. mayna. Johnston, "Frozen-State Storage Stability of a Monoclonal Antibody: Aggregation is Impacted by Freezing Rate and Solute Distribution," *Int. J. Pharm. Sci.*, vol. 102, no. 4, pp. 1194–1208, 2013.

[72]   FDA, "PAT — A Framework for Innovative Pharmaceutical Development, Manufacturing, and Quality Assurance," 2004.

[73]   J. N. Sangshetti, M. Deshpande, Z. Zaheer, D. B. Shinde, and R. Arote, "Quality by design approach: Regulatory need," *Arab. J. Chem.*, vol. 10, pp. S3412–S3425, 2017.

[74]   R. S. Uberoi, E. Swati, U. Gupta, and A. Sibal, "Root Cause Analysis in Healthcare," *Apollo Med.*, vol. 4, no. 1, pp. 72–75, 2007.

[75]   H. Bhatia, E. Read, C. Agarabi, K. Brorson, S. Lute, and S. Yoon, "A design space exploration for control of Critical Quality Attributes of mAb," *Int. J. Pharm.*, vol. 512, no. 1, pp. 242–252, 2016.

[76]   X. Le Saout, E. Youssef, H. Broly, and M. D. Costioli, "Safe Freeze – Thaw of Protein Drug Products : A QbD Approach," *BioPharm Int.*, no. December, pp. 28–43, 2012.

[77]   K. A. Pikal-Cleland and J. F. Carpenter, "Protein Denaturation during Freezing and Thawing in Phosphate Buffer Systems: Monomeric and Tetrameric ☒-Galactosidase," *J. Pharm. Sci.*, vol. 90, no. 9, pp. 1255–1268, 2001.

[78]   G. Larsson, M. Törnkvist, E. S. Wernersson, C. Trägårdh, H. Noorman, and S.-O. Enfors, "Substrate gradients in bioreactors: origin and consequences," *Bioprocess Eng.*, vol. 14, no. 6, pp. 281–289, 1996.

[79]   A. S. Rathore, M. Yu, S. Yeboah, and A. Sharma, "Case study and application of process analytical technology (PAT) towards bioprocessing: Use of on-line high-performance liquid chromatography (HPLC) for making real-time pooling decisions for process chromatography," *Biotechnol. Bioeng.*, vol. 100, no. 2, pp. 306–316, Jun. 2008.

[80]   R. L. Fahrner, P. M. Lester, G. S. Blank, and D. H. Reifsnyder, "Real-time control of purified product collection during chromatography of recombinant

human insulin-like growth factor-I using an on-line assay," *J. Chromatogr. A*, vol. 827, no. 1, pp. 37–43, 1998.

[81] E. K. Read, J. T. Park, R. B. Shah, B. S. Riley, K. A. Brorson, and A. S. Rathore, "Process analytical technology (PAT) for biopharmaceutical products: Part I. concepts and applications," *Biotechnol. Bioeng.*, vol. 105, no. 2, pp. 276–284, Feb. 2010.

[82] L. Rolinger, M. Rüdt, and J. Hubbuch, "A critical review of recent trends, and a future perspective of optical spectroscopy as PAT in biopharmaceutical downstream processing," *Anal. Bioanal. Chem.*, Mar. 2020.

[83] K. Buckley and A. G. Ryder, "Applications of Raman Spectroscopy in Biopharmaceutical Manufacturing: A Short Review," *Appl. Spectrosc.*, vol. 71, no. 6, pp. 1085–1116, 2017.

[84] R. l. McCreery, *Raman Spectroscopy for Chemical Analysis*. John Wiley & Sons, Ltd, 2005.

[85] C. V. Raman and K. S. Krishnan, "The production of new radiations by light scattering. —Part I," *Proc. R. Soc. London. Ser. A, Contain. Pap. a Math. Phys. Character*, vol. 122, no. 789, pp. 23–35, Jan. 1929.

[86] A. Rygula, K. Majzner, K. M. Marzec, A. Kaczor, M. Pilarczyk, and M. Baranska, "Raman spectroscopy of proteins: a review," *J. Raman Spectrosc.*, vol. 44, no. 8, pp. 1061–1076, Aug. 2013.

[87] Y.-C. Kao *et al.*, "Multiplex Surface-Enhanced Raman Scattering Identification and Quantification of Urine Metabolites in Patient Samples within 30 min," *ACS Nano*, vol. 14, no. 2, pp. 2542–2552, Feb. 2020.

[88] T. Vankeirsbilck *et al.*, "Applications of Raman spectroscopy in pharmaceutical analysis," *TrAC - Trends Anal. Chem.*, vol. 21, no. 12, pp. 869–877, 2002.

[89] R. M. Santos, J.-M. Kessler, P. Salou, J. C. Menezes, and A. Peinado, "Monitoring mAb cultivations with in-situ raman spectroscopy: The influence of spectral selectivity on calibration models and industrial use as reliable PAT tool," *Biotechnol. Prog.*, vol. 34, no. 3, pp. 659–670, May 2018.

[90] D. Yilmaz, H. Mehdizadeh, D. Navarro, A. Shehzad, M. O'Connor, and P. McCormick, "Application of Raman spectroscopy in monoclonal antibody producing continuous systems for downstream process intensification," *Biotechnol. Prog.*, vol. 36, no. 3, p. e2947, May 2020.

[91] L. Rolinger, M. Rüdt, and J. Hubbuch, "Comparison of UV- and Raman-based monitoring of the Protein A load phase and evaluation of data fusion by PLS models and CNNs," *Biotechnol. Bioeng.*, vol. n/a, no. n/a, pp. 1– 14, 2021.

[92] U. Roessl, S. Leitgeb, S. Pieters, T. De Beer, and B. Nidetzky, "In situ protein secondary structure determination in ice: Raman spectroscopy-based process analytical tool for frozen storage of biopharmaceuticals," *J. Pharm. Sci.*, vol. 103, no. 8, pp. 2287–2295, 2014.

[93] F. Marini, R. Bucci, A. L. Magrì, and A. D. Magrì, "Artificial neural networks in chemometrics: History, examples and perspectives," *Microchem. J.*, vol. 88, no. 2, pp. 178–185, 2008.

[94] W. Kessler, *Multivariate Datenanalyse: für die Pharma-, Bio- und Prozessanalytik*. Wiley-VCH Verlag GmbH & Co. KGaA, 2006.

[95] FDA, "Reporting of Computational Modeling Studies in Medical Device Submissions," 2016.

[96] Y. Toparlar, B. Blocken, B. Maiheu, and G. J. F. van Heijst, "A review on the CFD analysis of urban microclimate," *Renew. Sustain. Energy Rev.*, vol. 80, pp. 1613–1640, 2017.

[97] M. M. Aslam Bhutta, N. Hayat, M. H. Bashir, A. R. Khan, K. N. Ahmad, and S. Khan, "CFD applications in various heat exchangers design: A review," *Appl. Therm. Eng.*, vol. 32, pp. 1–12, 2012.

[98] V. Ramesh, S. Terala, S. Mazumder, G. Matharu, D. Vaishnav, and S. Ali, "Development and Validation of a Model for Efficient Simulation of Freezing of Water in Large Tanks," *J. Therm. Sci. Eng. Appl.*, vol. 13, no. 1, 2021.

[99] H. Jayakody, R. Al-Dadah, and S. Mahmoud, "Computational fluid dynamics investigation on indirect contact freeze desalination," *Desalination*, vol. 420, no. May, pp. 21–33, 2017.

[100] N. Shevchenko, O. Roshchupkina, O. Sokolova, and S. Eckert, "The effect of natural and forced melt convection on dendritic solidification in Ga-In alloys," *J. Cryst. Growth*, vol. 417, pp. 1–8, 2015.

[101] K. C. Bauer, S. Suhm, A. K. Wöll, and J. Hubbuch, "Impact of additives on the formation of protein aggregates and viscosity in concentrated protein solutions," *Int. J. Pharm.*, vol. 516, no. 1–2, pp. 82–90, Jan. 2017.

[102] J. R. Authelin *et al.*, "Freezing of Biologicals Revisited: Scale, Stability, Excipients, and Degradation Stresses," *Journal of Pharmaceutical Sciences.* 2020.

[103] S. K. Singh, P. Kolhe, W. Wang, and S. Nema, "Large-scale freezing of biologics," *BioProcess International*, vol. 7, no. 9, pp. 32–44, 2009.

[104] H. Reinsch, O. Spadiut, J. Heidingsfelder, and C. Herwig, "Examining the freezing process of an intermediate bulk containing an industrially relevant protein," *Enzyme Microb. Technol.*, vol. 71, pp. 13–19, 2015.

[105] A. K. Wöll, J. Schütz, J. Zabel, and J. Hubbuch, "Analysis of phase behavior and morphology during freeze-thaw applications of lysozyme," *Int. J. Pharm.*, vol. 555, no. September 2018, pp. 153–164, 2019.

[106] U. Roessl, D. Jajcevic, S. Leitgeb, J. G. Khinast, and B. Nidetzky, "Characterization of a laboratory-scale container for freezing protein solutions with detailed evaluation of a freezing process simulation," *J. Pharm. Sci.*, vol. 103, no. 2, pp. 417–426, 2014.

[107] H. Maity, C. Karkaria, and J. Davagnino, "Mapping of solution components, pH changes, protein stability and the elimination of protein precipitation during freeze-thawing of fibroblast growth factor 20," *Int. J. Pharm.*, vol. 378, no. 1–2, pp. 122–135, 2009.

[108] T. H. Fan *et al.*, "Phase-field modeling of freeze concentration of protein solutions," *Polymers (Basel).*, vol. 11, no. 1, pp. 1–20, 2018.

[109] T. J. Zbacnik *et al.*, "Role of Buffers in Protein Formulations," *J. Pharm. Sci.*, vol. 106, no. 3, pp. 713–733, 2017.

[110] R. Plank, "Die Gefrierdauer von Eisblocken," *Zeitschrift für die gesamte Kälteindustrie*, vol. 20, no. 6, pp. 109–114, 1913.

[111] Q. T. Pham, "Mathematical modeling of freezing processes," *Handb. Frozen Food Process. Packag.*, pp. 141–174, 2005.

[112] H. Martin, *Transient Conduction in Stagnant Media*, 2nd intern. Springer, Berlin, Heidelberg, 2010.

[113] M. Randall and F. D. Rossini, "Heat capacities in aqueous salt solutions," *J. Am. Chem. Soc.*, vol. 51, no. 2, pp. 323–345, 1929.

[114] H. Kumano, T. Asaoka, A. Saito, and S. Okawa, "Study on latent heat of fusion of ice in aqueous solutions," *Int. J. Refrig.*, vol. 30, no. 2, pp. 267–273, 2007.

[115] P. Kolhe, A. Mehta, A. Lary, S. Chico, and S. K. Singh, "Large-Scale Freezing of Biologics (Part III) Understanding Frozen-State Protein and Solute Concentration Changes in Celsius Bags," *BioPharm Int.*, vol. 25, no. October, pp. 40–48, 2012.

[116] J. F. Buyel, R. M. Twyman, and R. Fischer, "Very-large-scale production of antibodies in plants: The biologization of manufacturing," *Biotechnol. Adv.*, vol. 35, no. 4, pp. 458–465, 2017.

[117] B. D. Connolly, L. Le, T. W. Patapoff, M. E. M. Cromwell, J. M. R. Moore, and P. Lam, "Protein Aggregation in Frozen Trehalose Formulations: Effects of Composition, Cooling Rate, and Storage Temperature," *J. Pharm. Sci.*, vol. 104, no. 12, pp. 4170–4184, 2015.

[118] P. A. Shamlou, L. H. Breen, W. V. Bell, M. Pollo, and B. A. Thomas, "A new scaleable freeze–thaw technology for bulk protein solutions," *Biotechnol. Appl. Biochem.*, vol. 46, no. 1, p. 13, 2007.

[119] V. Geraldes, D. C. Gomes, P. Rego, D. Fegley, and M. A. Rodrigues, "A New Perspective on Scale-Down Strategies for Freezing of Biopharmaceutics by Means of Computational Fluid Dynamics," *J. Pharm. Sci.*, vol. 109, no. 6, pp. 1978–1989, 2020.

[120] D. Weber and J. Hubbuch, "Temperature Based Process Characterization of Pharmaceutical Freeze-Thaw Operations," vol. 9, no. April, pp. 1–9, 2021.

[121] M. A. Rodrigues, M. A. Miller, M. A. Glass, S. K. Singh, and K. P. Johnston, "Comparison of freezing rate and dendritic ice formation on concentration profiles of proteins frozen in cylindrical vessels," *J. Pharm. Sci.*, vol. 101, no. 1, pp. 322–332, 2012.

[122] J. Q. Li and T. H. Fan, "Phase-field modeling of macroscopic freezing dynamics in a cylindrical vessel," *Int. J. Heat Mass Transf.*, vol. 156, p. 119915, 2020.

[123] J. Dong, A. Hubel, J. C. Bischof, and A. Aksan, "Freezing-induced phase separation and spatial microheterogeneity in protein solutions," *J. Phys. Chem. B*, vol. 113, no. 30, pp. 10081–10087, 2009.

[124] A. Savitzky and M. J. E. Golay, "Smoothing and Differentiation of Data by Simplified Least Squares Procedures.," *Anal. Chem.*, vol. 36, no. 8, pp. 1627–1639, Jul. 1964.

[125] S. Großhans *et al.*, "In-line Fourier-transform infrared spectroscopy as a versatile process analytical technology for preparative protein chromatography," *J. Chromatogr. A*, vol. 1547, pp. 37–44, 2018.

[126] S. Wold, M. Sjöström, and L. Eriksson, "PLS-regression: A basic tool of chemometrics," *Chemom. Intell. Lab. Syst.*, vol. 58, no. 2, pp. 109–130, 2001.

[127] E. Schmälzlin *et al.*, "Raman Imaging with a Fiber-Coupled Multichannel Spectrograph," *Sensors*, vol. 14, no. 11. 2014.

[128] N. Ockman, "The infra-red and Raman spectra of ice," *Adv. Phys.*, vol. 7, no. 26, pp. 199–220, 1958.

[129] I. Đuričković, R. Claverie, P. Bourson, M. Marchetti, J. M. Chassot, and M. D. Fontana, "Water-ice phase transition probed by Raman spectroscopy," *J.*

Raman Spectrosc., vol. 42, no. 6, pp. 1408–1412, 2011.

[130] S. Guo, T. Bocklitz, and J. Popp, "Optimization of Raman-spectrum baseline correction in biological application," *Analyst*, vol. 141, no. 8, pp. 2396–2404, 2016.

[131] D. R. Parachalil, B. Brankin, J. McIntyre, and H. J. Byrne, "Raman spectroscopic analysis of high molecular weight proteins in solution-considerations for sample analysis and data pre-processing," *Analyst*, vol. 143, no. 24, pp. 5987–5998, 2018.

[132] J. Filik and N. Stone, "Drop coating deposition Raman spectroscopy of protein mixtures," *Analyst*, vol. 132, no. 6, pp. 544–550, 2007.

[133] D. R. Rohleder *et al.*, "Comparison of mid-infrared and Raman spectroscopy in the quantitative analysis of serum," *J. Biomed. Opt.*, vol. 10, no. 3, pp. 1–10, May 2005.

[134] J. F. Torres, A. Komiya, J. Okajima, and M. Shigenao, "Measurement of the molecular mass dependence of the mass diffusion coefficient in protein aqueous solutions," *Defect Diffus. Forum*, vol. 326–328, pp. 452–458, 2012.

[135] D. Weber, C. Sittig, and J. Hubbuch, "Impact of Freeze-Thaw Processes on Monoclonal Antibody Platform Process Development," *Biotechnol. Bioeng.*, vol. 118, no. 10, 2021.

[136] P. H. Oosthuizen and J. T. Paul, "A numerical study of the steady state freezing of water in an open rectangular cavity," *Int. J. Numer. Methods Heat Fluid Flow*, vol. 6, no. 5, pp. 3–16, Jan. 1996.

[137] W. F. Giauque and J. W. Stout, "The Entropy of Water and the Third Law of Thermodynamics. The Heat Capacity of Ice from 15 to 273°K.," *J. Am. Chem. Soc.*, vol. 58, no. 7, pp. 1144–1150, Jul. 1936.

[138] R. Darros-Barbosa, "High pressure and temperature dependence of thermodynamic properties of model food solutions obtained from in situ ultrasonic measurements," University of Florida, 2003.

[139] Z. Bubnik, P. Kadlec, D. Urban, and M. Bruhns, *Sugar Technologists Manual*, 8th editio. Berlin: Bartens, 1996.

[140] V. V. R. & P. C., "A Fixed grid numerical modelling methodology for convection diffusion mushy region phase change problems," *Int. Jounal Heat Mass Transf.*, vol. 30, no. 8, pp. 1709–1719, 1978.

[141] S. L. Braga and R. Viskanta, "Effect of density extremum on the solidification of water on a vertical wall of a rectangular cavity," *Exp. Therm. Fluid Sci.*, vol. 5, no. 6, pp. 703–713, 1992.

[142] G. Wada and S. Umeda, "Effects of nonelectrolytes on the temperature of the maximum density of water. I. Alcohols," *Bull. Chem. Soc. Jpn.*, vol. 35, no. 4, pp. 646–652, 1962.

[143] F. E. Young and F. T. Jones, "Sucrose HYDRATES The Sucrose-Water," pp. 1334–1350, 1949.

[144] H. C. Price, J. Mattsson, and B. J. Murray, "Sucrose diffusion in aqueous solution," *Phys. Chem. Chem. Phys.*, vol. 18, no. 28, pp. 19207–19216, 2016.

[145] R. Courant, K. Friedrichs, and H. Lewy, "Über die partiellen Differenzengleichungen der mathematischen Physik," *Math. Ann.*, vol. 100, no. 1, pp. 32–74, 1928.

[146] P. Baumann and J. Hubbuch, "Downstream process development strategies for effective bioprocesses: Trends, progress, and combinatorial approaches," *Eng. Life Sci.*, vol. 17, no. 11, pp. 1142–1158, Nov. 2017.

[147] H.-C. Mahler, W. Friess, U. Grauschopf, and S. Kiese, "Protein aggregation: Pathways, induction factors and analysis," *J. Pharm. Sci.*, vol. 98, no. 9, pp. 2909–2934, 2009.

[148] S. N. Telikepalli *et al.*, "Structural Characterization of IgG1 mAb Aggregates and Particles Generated Under Various Stress Conditions," *J. Pharm. Sci.*, vol. 103, no. 3, pp. 796–809, 2014.

[149] X. Wang, A. K. Hunter, and N. M. Mozier, "Host cell proteins in biologics development: Identification, quantitation and risk assessment," *Biotechnol. Bioeng.*, vol. 103(3), pp. 446–58, 2009.

[150] A. J. Paul, K. Schwab, and F. Hesse, "Direct analysis of mAb aggregates in mammalian cell culture supernatant," *BMC Biotechnol.*, vol. 14, no. 1, pp. 1–11, 2014.

[151] Z. D. Dunn, J. Desai, G. M. Leme, D. R. Stoll, and D. D. Richardson, "Rapid two-dimensional Protein-A size exclusion chromatography of monoclonal antibodies for titer and aggregation measurements from harvested cell culture fluid samples," *MAbs*, vol. 12, no. 1, 2020.

[152] W. Kast, (Revised by Hermann Nirschl), E. S. Gaddis, K.-E. Wirth, and J. Stichlmair, "L1 Pressure Drop in Single Phase Flow," in *VDI Heat Atlas*, 2nd ed., VDI, Ed. Springer-Verlag Berlin Heidelberg, 2010, pp. 1053–1116.

[153] Y. H. Chen, E. Cao, and Z. F. Cui, "An experimental study of freeze concentration in biological media," *Food Bioprod. Process.*, vol. 79, no. March, pp. 35–40, 2001.

[154] J. S. Bee, L. Tie, D. Johnson, M. N. Dimitrova, K. C. Jusino, and C. D. Afdahl, "Trace levels of the CHO host cell protease cathepsin D caused particle formation in a monoclonal antibody product," *Biotechnol. Prog.*, vol. 31, no. 5, pp. 1360–1369, Sep. 2015.

[155] H.-W. Birk, A. Kistner, V. Wizemann, and G. Schütterle, "Protein Adsorption by Artificial Membrane Materials Under Filtration Conditions," *Artif. Organs*, vol. 19, no. 5, pp. 411–415, 1995.

[156] B. Nogal, K. Chhiba, and J. C. Emery, "Select host cell proteins coelute with monoclonal antibodies in protein a chromatography," *Biotechnol. Prog.*, vol. 28, no. 2, pp. 454–458, 2012.

[157] Q. Zhang *et al.*, "Characterization of the co-elution of host cell proteins with monoclonal antibodies during protein A purification," *Biotechnol. Prog.*, vol. 32, no. 3, pp. 708–717, 2016.

[158] A. Hauptmann, K. Podgoršek, D. Kuzman, S. Srčič, G. Hoelzl, and T. Loerting, "Impact of Buffer, Protein Concentration and Sucrose Addition on the Aggregation and Particle Formation during Freezing and Thawing," *Pharm. Res.*, vol. 35, no. 5, 2018.

[159] S. P. F. M. Roefs and K. G. De Kruif, "A Model for the Denaturation and Aggregation of ß-Lactoglobulin," *Eur. J. Biochem.*, vol. 226, no. 3, pp. 883–889, Dec. 1994.

Abbreviations and Symbols

Abbreviations

API	Active pharmaceutical ingredient
BSA	Bovine serum albumin
CAD	computer aided design
CCD	charge-coupled device
CCS	Cell culture supernatant
CE	Capillary electrophoresis
CFD	Computational fluid dynamics
CPP	Critical process parameter
CQA	Critical quality attribute
CV	Column volume
ELISA	Enzyme-linked immunosorbent assay
emsc	extended multiplicative signal correction
FDA	Food and Drug Administration
HCP	Host cell proteins
HPLC	High performance liquid chromatography
ICH	International Council for Harmonisation of Technical Requirements for Pharmaceuticals for Human Use
LPTF	Last point to freeze
mAb	Monoclonal antibody
mRNA	Messenger ribonucleic acid
r	Radius
RMSECV	Root mean square error of cross validation
PAT	Process analytical technology
PLS	Partial least squares
PPA	Post Protein A

PRESS   Predictive residual sum of squares

PTFE   Polytetrafluoroethylene

SIMPLE   the semi-implicit method for pressure linked equations

UV-Vis   visible and ultra-violet

Latin Symbols

A	Surface area
A260	Absorption at 260 nm wavelength
A280	Absorption at 280 nm wavelength
Bi	Biot number
c	concentration
c_p	Heat capacity
D	diffusivity
E	Geometric factor in the Plank equation
H	Enthalpy
k	Partition coefficient
k_a	Heat transfer resistance of the shell in the Plank equation
n	Number of observations for calculation of residuals
p	p-Value returned by t-test
$\dot{q}$	Heat flux
$\dot{Q}$	Heat flow
r	Distance from inner cooling wall
R^2	Coefficient of determination
T	Temperature
t	Time
w	Mass fraction
y	variable
X	Characteristic distance in the Plank Equation
x	Heat conducting distance

Greek Symbols

ß	Solid fraction in enthalpy-porosity description

λ	Heat conductivity
ρ	density
μ	Dynamic viscosity
Δv	Raman shift